



**HAL**  
open science

# Analyse et validation expérimentale de la plus basse fréquence utilisable dans une chambre réverbérante à parois métamatériaux pour des tests de Compatibilité ElectroMagnétique (CEM)

Jeudy Kean

► **To cite this version:**

Jeudy Kean. Analyse et validation expérimentale de la plus basse fréquence utilisable dans une chambre réverbérante à parois métamatériaux pour des tests de Compatibilité ElectroMagnétique (CEM). Autre. Institut National Polytechnique de Toulouse - INPT; Institut de technologie du Cambodge (Phnom Penh ; 1964-..), 2023. Français. NNT : 2023INPT0057 . tel-04219721

**HAL Id: tel-04219721**

**<https://theses.hal.science/tel-04219721v1>**

Submitted on 27 Sep 2023

**HAL** is a multi-disciplinary open access archive for the deposit and dissemination of scientific research documents, whether they are published or not. The documents may come from teaching and research institutions in France or abroad, or from public or private research centers.

L'archive ouverte pluridisciplinaire **HAL**, est destinée au dépôt et à la diffusion de documents scientifiques de niveau recherche, publiés ou non, émanant des établissements d'enseignement et de recherche français ou étrangers, des laboratoires publics ou privés.



Université  
de Toulouse

# THÈSE

En vue de l'obtention du

## DOCTORAT DE L'UNIVERSITÉ DE TOULOUSE

**Délivré par :**

Institut National Polytechnique de Toulouse (Toulouse INP)

**Discipline ou spécialité :**

Electromagnétisme et Systèmes Haute Fréquence

---

**Présentée et soutenue par :**

M. JEUDY KEAN

le lundi 26 juin 2023

**Titre :**

Analyse et validation expérimentale de la plus basse fréquence utilisable dans une chambre réverbérante à parois métamatériaux pour des tests de Compatibilité ElectroMagnétique (CEM)

---

**École doctorale :**

Génie Electrique, Electronique, Télécommunications (GEETS)

**Unité de recherche :**

Laboratoire Plasma et Conversion d'Énergie ( LAPLACE)

**Directeurs de Thèse :**

MME NATHALIE RAVEU

M. SOKCHENDA SRENG

**Rapporteurs :**

M. ANTHONY GHIOTTO, UNIVERSITE DE BORDEAUX

MME ELODIE RICHALOT, UNIVERSITE GUSTAVE EIFFEL

**Membres du jury :**

M. RAPHAËL GILLARD, INSA DE RENNES, Président

M. HAMZA KAOUACH, TOULOUSE INP, Membre

MME NATHALIE RAVEU, TOULOUSE INP, Membre

M. SOKCHENDA SRENG, INSTITUT DE TECHNOLOGIE DU CAMBODGE, Membre



# Résumé

La chambre réverbérante est l'un des environnements d'essai dans le domaine des Interférences ElectroMagnétiques et de la Compatibilité ElectroMagnétique (IEM/CEM). Les chambres réverbérantes ont été couramment utilisées pour plusieurs essais CEM tels que les essais d'immunité rayonnée, les essais d'émission rayonnée, les mesures d'efficacité de blindage. Dans le cadre du développement des systèmes de communication mobile 4G/5G, cette chambre peut être utilisée comme émulateur de canal pour les liaisons sans fil.

Pour tester un appareil électronique de petite taille fonctionnant à basse fréquence, il ne devrait pas être nécessaire d'utiliser une chambre de grande taille. Réduire la taille de la chambre a plusieurs avantages : sa fabrication utilise moins de matériaux de construction, ce qui permet de réduire le coût de fabrication par rapport à une chambre plus grande ; elle pourrait également être déplacée. Pour une chambre conventionnelle, donc complètement métallisée, la fréquence de fonctionnement est déterminée par ses dimensions puisque la fréquence la plus basse utilisable (LUF) peut être estimée à partir de 60<sup>ème</sup> mode. Cette LUF correspond à la fréquence à partir de laquelle les champs peuvent être considérés comme homogènes et isotropes dans le volume où le dispositif sous test peut être positionné. Cette LUF est donc nécessairement élevée pour les chambres réverbérantes métalliques de petite taille. L'utilisation de métamatériaux comme parois de la chambre réverbérante peut permettre de réduire cette LUF. De plus, le choix du meilleur métamatériau est difficile à prévoir car ces matériaux artificiels sont nombreux. En outre, l'optimisation des parois métamatériaux de la chambre nécessite un temps de calcul important sans aucune garantie qu'un optimum puisse être atteint. L'objectif principal de cette thèse est d'étudier cette nouvelle topologie de chambre réverbérante utilisant des parois métamatériaux pour concevoir une chambre de taille réduite mais fonctionnant aux fréquences basses.

Dans ce travail, la Théorie Modale Elargie (TME) est proposée pour définir les parois métamatériaux à insérer, elles sont qualifiées comme des parois homogénéisées anisotropes appelées impédances de surface. Diverses impédances de surface sont testées pour connaître la gamme la plus favorable à réduire la LUF. Puis, une cellule élémentaire correspondant à ces impédances de surface est déterminée et insérée sur les parois de la chambre réverbérante. Les modes sont calculés grâce à une simulation de modes propres d'une cavité rectangulaire avec des parois en métamatériaux afin d'observer l'efficacité de la cellule unitaire proposée. Dans un second temps, l'ensemble de la structure de la chambre réverbérante, qui comprend la cage de Faraday, le brasseur, l'antenne d'excitation et les parois métamatériaux, est construit pour validation par des mesures. Les données relatives à l'amplitude du champ électrique pour 9 positions de la sonde dans le volume dédié aux mesures du dispositif sous test, suivant les 3 polarisations orthogonales, pour 36 angles de rotation du brasseur sont extraites pour évaluer la LUF. Les valeurs des LUF de deux cas, avec et sans les parois métamatériaux, sont comparées pour prouver l'avantage de la nouvelle topologie de la chambre avec les parois métamatériaux et son usage à des fréquences plus basses que la chambre réverbérante conventionnelle.

# Abstract

Reverberation chamber is one of testing environments in Electromagnetic Interference/Electromagnetic Compatibility (EMI/EMC) domain. The reverberation chambers have been commonly used for several EMC tests such as the radiated immunity test, the radiated emission test, the measurement of the material shielding effectiveness, the evaluation of the permittivity of material and the antenna characterization. In the development of 4G/5G mobile communication system, the chamber can be used as the wireless channel emulator.

To test a small-size electronic device operating at low frequency, small-size reverberation chamber is preferred. Despite its size and perhaps ability to be moved, its fabrication uses less construction material resulting in reduction of the fabrication cost compared to a larger chamber. For the conventional chamber, the operation frequency is ruled by its dimensions since the Lowest Usable Frequency (LUF) may be estimated from the frequency of the 60<sup>th</sup> resonant mode. This LUF is high for small reverberation chamber. Using metamaterials as walls of the reverberation chamber can lead to the chamber's LUF reduction. However, the best choice of metamaterial is difficult to predict since these artificial materials are numerous. Furthermore, the optimization of the metamaterial walls in the chamber require large amount of times without any guarantee that an optimum can be reached. The main objective of this thesis is to study this new topology of reverberation chamber using metamaterial walls to conceive a small chamber operating at low frequency.

In this work, firstly, the Modal Expansion Theory (MET) is proposed to define which anisotropic walls should be inserted. Various metamaterial unit cells are tested to find the unit cell's impedance. Then, a unit cell structure is selected, modeled and inserted in an ideal reverberation chamber. Modes are computed thanks to an Eigen-mode simulation of rectangular cavity with metamaterial walls to observe the efficiency of the proposed unit cell. Secondly, the whole structure of the reverberation chamber which includes the stirrer, the excitation antenna and the two panels of metamaterial is constructed for the measurement validation. To achieve this purpose, the structure of the stirrer is selected, the excitation antenna and its position on the chamber wall are evaluated. The electric field strength data, from the 9 positions of the field probe in the working volume with the 36 step angles of stirrer rotation, are extracted to evaluate the LUF value. The LUF values, with and without the metamaterial walls, are compared to prove the advantage of the new topology of the chamber with metamaterial walls.

# Acknowledgement

First of all, I would like to take this opportunity to express my deepest gratitude and thank to my supervisor at Toulouse INP, Mrs. Nathalie RAVEU, professor and head of Département Électronique, Energie Électrique & Automatique (3EA) of the École nationale supérieure d'électrotechnique, d'électronique, d'informatique, d'hydraulique et des télécommunications (ENSEEIHT), for her advices and guidance in conducting this research. Mrs. RAVEU is a supportive supervisor. She always continuously provided encouragement and was always willing to assist me in any way she could throughout the research project. I am gratefully thanking to my co-supervisor at Toulouse INP, Mr. Hamza KAOUACH, associate professor at 3EA department of ENSEEIHT, for his supports, advices, facilitation and discussion during this research duration. I do not know where I would be without his supports.

I would like also to express my sincere gratitude and thank to my supervisor at Institute of Technology of Cambodia (ITC), Mr. Sokchenda SRENG, lecturer and head of Department of Telecommunication and Network (GTR), for his invaluable advice and continuously support. He entirely supports me from the very beginning until the completion of this work. I am particularly grateful for the advices given by my co-supervisor at ITC, Mr. Kosorl THOURN, lecturer and vice-head of GTR department, for his technical discussion and practical suggestion. I would like also to thank Mr. THOURN for his acceptance to be my thesis examiner.

I would like to extend my sincere thanks to Mr. Anthony GHIOTTO, associate professor with full professor habilitation, Laboratory of Integration from Materials to System (IMS Laboratory), University of Bordeaux and Mrs. Elodie RICHALOT, professor, Laboratoire Electronique, SYstemes de COMmunications et Microsystemes (ESYCOM Laboratory), Université Gustave Eiffel, for their acceptances to be the referees of my thesis. I would like also extend my gratitude to Mr. Raphaël GILLARD, professor, Institut d'Electronique et des Technologies du numéRique (IETR), INSA of Rennes, for his acceptance to be the examiner of my thesis.

I am also grateful to Mr. Olivier PIGAGLIO, research engineer, Laboratoire PLasma et Conversion d'Énergie (LAPLACE Laboratory), Toulouse INP, for his support in constructing and measuring the prototype of reverberation chamber and the metamaterials in this research.

I have great pleasure of working with people in the LAPLACE laboratory of Toulouse INP and GTR department of ITC. They provided me with encouragement and patience throughout the duration of this research.

I would like to thank the French Government Scholarship (BGF) co-funded by Ministry of Education, Youth and Sports (MoYES) of Cambodia for their main financially support of this doctoral studies. I would like also to thank the Higher Education Improvement Project (HEIP) SGA#03, Institute of Technology of Cambodia (ITC), Food-STEM Erasmus+ and Toulouse INP Erasmus+ program for addition financial support for my stay in France and in Cambodia during this research. I would like to thank to my home institution, ITC, for allowing me to grab this

opportunity to continue my study during being the staff there and thank to the LAPLACE laboratory of Toulouse INP for the warm welcome during this thesis duration.

Last but not least, I would like to thank to my family for their mental support during my stay in Cambodia and abroad. I can work calmly because of their patience and encouragement. I would like also thank to all friends that always keep in touch with me all the times. Many thanks to Menghorng, Thavath and Sothea for the help during the defense preparation as well as the relax time together after work.

This manuscript would not be completed without the technical, academic, financial and mental support from various organizations, institutions, laboratory and people that are mentioned above.

# Table of contents

Résumé .....	2
Abstract .....	3
Acknowledgement .....	4
Table of contents .....	6
Acronyms .....	9
List of figures .....	10
List of tables .....	13
1. Introduction .....	15
1.1. Electromagnetic interference and measurement environment .....	16
1.1.1. Open Area Test Site (OATS).....	16
1.1.2. Anechoic Chamber (AC) .....	17
1.1.3. Reverberation Chamber (RC) .....	18
1.2. Problem statement and research motivation .....	18
1.3. Research objective and methodology .....	19
1.4. Dissertation contribution and structure .....	19
2. Reverberation chamber characteristics and challenges .....	21
2.1. Structure and components of the reverberation chamber.....	22
2.2. Reverberation chamber properties .....	24
2.2.1. Working Volume .....	24
2.2.2. Lowest Usable Frequency .....	24
2.2.3. Quality Factor (Q-factor).....	25
2.3. Qualification method with standard IEC 61000-4-21 .....	26
2.3.1. Location of field probe .....	27



2.3.2.	Measurement procedure and stored data .....	27
2.3.3.	Standard deviation evaluation .....	28
2.3.4.	LUF assumption with tolerance requirement of the IEC 61000-4-21 .....	30
2.4.	Design challenges of RC with MTMs walls.....	30
3.	Design of the metamaterial unit cell.....	32
3.1.	MET for the analysis of anisotropic walls reverberation chamber .....	33
3.1.1.	Analysis of anisotropic walls reverberation chamber .....	33
3.1.2.	Validation of the MET method.....	38
3.1.3.	Sensitivity analysis to the surface impedance .....	41
3.2.	Design and characterization of the metamaterial unit cell .....	41
3.2.1.	Unit cell structures.....	42
3.2.2.	Metamaterial unit cell design .....	46
3.2.3.	Characterization of the metamaterial unit cell.....	50
3.3.	Conclusion .....	54
4.	Sensitivity analysis and characterization of reverberation chamber prototype .....	55
4.1.	Sensitivity analysis on the cavity .....	56
4.1.1.	Metallic walls selection.....	56
4.1.2.	Material and capacitor selection for the metamaterial walls .....	57
4.2.	Reverberation chamber prototype .....	61
4.2.1.	Stirrer design and position.....	62
4.2.2.	Working volume and field probe location in the reverberation chamber .....	65
4.2.3.	Antenna selection and position.....	67
4.2.4.	Configuration set up .....	72
4.3.	Measurement and qualification of the chamber .....	76

4.3.1.	Measurement configuration and data extraction .....	76
4.3.2.	Chamber prototype with metallic and with metamaterial walls .....	79
4.3.3.	LUF results, comparison and discussion .....	80
4.4.	Conclusion .....	82
5.	Conclusion and future perspective .....	83
6.	Annex .....	84
6.1.	Relation between the transverse and the longitudinal components of the electromagnetic field.....	84
6.1.1.	Propagating in the forward direction (formula with term $e^{-\gamma_z z}$ ) .....	84
6.1.2.	Propagating in the backward direction (formula with term $e^{+\gamma_z z}$ ) .....	86
6.2.	MET analysis for the rectangular cavity with two anisotropic walls.....	90
6.2.1.	Longitudinal components of electromagnetic field .....	90
6.2.2.	Expression of the transverse components of the EM field .....	94
6.2.3.	Surface impedance boundary conditions .....	103
6.2.4.	System of linear equation .....	103
6.2.5.	Special case with zero order modes.....	107
6.3.	The Z-fold stirrer design .....	111
6.3.1.	The condition to select the dimension of the mechanical stirrer .....	111
6.3.2.	Selection of stirrer structure and appropriate dimension.....	111
6.3.3.	The position of stirrer in the chamber .....	115
6.4.	The working volume and location of field probe.....	117
6.5.	Changing distance to anisotropic surface impedance walls.....	119
	Publications .....	122
	References .....	123

# Acronyms

<b>AC</b>	Anechoic Chamber
<b>AD-GoF</b>	Anderson-Darling Goodness-of-fit
<b>AF</b>	Antenna Factor
<b>DNG</b>	Double Negative metamaterial
<b>EM</b>	Electromagnetic
<b>EMC</b>	ElectroMagnetic Compatibility
<b>EMI</b>	ElectroMagnetic Interference
<b>EUT</b>	Equipment Under Test
<b>FAC</b>	Full Anechoic Chamber
<b>FEM</b>	Finite Element Method
<b>GTEM</b>	Gigahertz TEM Cell
<b>GUI</b>	Graphic User Interface
<b>HFSS</b>	High Frequency Structure Simulator
<b>IEC</b>	International Electro-technical Commission
<b>LPDA</b>	Log-Periodic Dipole Array antenna
<b>LUF</b>	Lowest Usable Frequency
<b>MET</b>	Modal Expansion Theory
<b>MTMs</b>	MetaMaTerials
<b>OATS</b>	Open Area Test Site
<b>PCB</b>	Printed Circuit Board
<b>PEC</b>	Perfect Electric Conductor
<b>Q-factor</b>	Quality Factor
<b>RAM</b>	Radiation Absorbers Materials
<b>RC</b>	Reverberation Chamber
<b>RTCA</b>	Radio Technical Commission for Aeronautics
<b>SAC</b>	Semi-Anechoic Chamber
<b>SNG</b>	Single Negative metamaterial
<b>TEM Cell</b>	Transverse ElectroMagnetic cell
<b>VIRC</b>	Vibrating Reverberation Chamber
<b>VNA</b>	Vector Network Analyzer
<b>WV</b>	Working Volume

# List of figures

Figure 2.1 : The typical components of the reverberation chamber [55].....	22
Figure 2.2 : Typical components of RC validated by AD GoF method [59].....	23
Figure 2.3 : Quality factor curves of RC with aluminum walls and with copper walls compared to threshold of Q-factor .....	25
Figure 2.4 : Configuration of RC for validation by IEC 61000-4-21 .....	26
Figure 2.5 : Field Probe locations in the RC .....	27
Figure 3.1 : Representation of the reverberation chamber with two anisotropic walls .....	33
Figure 3.2 : Tthe resonant frequencies of the PEC walls RC .....	39
Figure 3.3 : Resonant frequencies in the RC with two isotropic walls $Z_t = Z_z = -jZ_0$ .....	40
Figure 3.4 : One example of unit cell simulation using Floquet port and Master/Slave (Primary/Secondary) boundary conditions .....	42
Figure 3.5 : The modification of the unit-cell with lumped capacitor (a) Capacitor in the center (b) Haft capacitor on both sides (c) The orthogonal line and capacitor are added in both polarization. ....	45
Figure 3.6 : HFSS model of the selected metamaterial surface .....	46
Figure 3.7 : The unit cell surface impedance for 3 different capacitors. ....	47
Figure 3.8 : The surface impedance for different incident angle, capacitor value is <b>39 pF</b> . .....	48
Figure 3.9 : Rectangular metallic box with two metamaterial walls .....	49
Figure 3.10 : Resonant mode frequencies for the PEC cavity by theory Vs. Metamaterial cavity simulated with Eigen-mode solver in HFSS .....	49
Figure 3.11 : Choice of the new capacitor value by simulation with HFSS of the unit cell. ....	50
Figure 3.12 : Two unit cells test in waveguide (a) 3D views (b) 2D views.....	51
Figure 3.13 : The prototype of the two unit cells inserted in the WR229 waveguide: (a) Back view (b) Top view (c) Place to insert two unit cells (d) Two unit cells attached in the waveguide and locked with screws.....	52

Figure 4.1 : The simulation model of small cavity box .....	56
Figure 4.2 : HFSS model of the rectangular cavity with two metamaterial walls .....	58
Figure 4.3 : Z-folded stirrer design.....	64
Figure 4.4 : Stirrer location in the reverberation chamber .....	65
Figure 4.5 : The locations of field probe: (a) 3D view with the origin O set in red dot and the positions of field probe FP1 to FP9 are on black dot (b) Side view from the back of horn antenna (c) Top view .....	66
Figure 4.6 : The location of field probe in the working volume identified by red dot (a) Case 9 field probe locations (b) Case 15 field probe locations (c) Case 27 field probe locations.....	67
Figure 4.7 : DRH20E double ridged horn antenna (dimension in mm).....	69
Figure 4.8 : Reflection coefficient of the horn antenna model vs. the real horn antenna with and without covering side walls by metallic sheets. ....	70
Figure 4.9 : Position of case 1.....	71
Figure 4.10 : Position of case 2.....	71
Figure 4.11 : Position of case 3.....	71
Figure 4.12 : Measurement configuration for RC qualification.....	76
Figure 4.13 : Measurement procedure .....	77
Figure 4.14 : The equipment for chamber qualification (a) Antenna and field probe (b) Inside view of aluminium walls chamber including field probe head and stirrer (c) VNA (d) Whole chamber structure .....	79
Figure 6.1 : Representation model of reverberation chamber with two anisotropic walls .....	90
Figure 6.2 : Dimension of the 1 <sup>st</sup> stirrer (side view).....	112
Figure 6.3 : The structure of the stirrer for the 1 <sup>st</sup> design consideration. ....	113
Figure 6.4 : The modified structure of stirrer to ease the prototype fabrication .....	114
Figure 6.5 : RC box which contain one stirrer.....	115
Figure 6.6 : Location of stirrer in the RC.....	116

Figure 6.7 : The location of WV in RC: (a) 3D view (b) Top view (c) Side view ..... 117

Figure 6.8 : WV and the 9 locations of field probe for chamber validation (a) 3D view (b) Side view (c) Top view ..... 118

## List of tables

Table 2.1 : The required number of stirrer positions and the sample frequencies according to IEC 61000-4-21 .....	28
Table 2.2 : The tolerance requirement of the standard deviation according to IEC 61000-4-21 [55] .....	30
Table 3.1 : LUF table for first 60 resonant modes of the anisotropic walls reverberation chamber .....	41
Table 3.2 : Some structures of unit cell for observation of resonant frequency for specific parameters value .....	43
Table 3.3 : Unit cell dimensions .....	47
Table 4.1 : The first 10 resonant frequencies and Q-factor for chamber with aluminum versus copper walls .....	57
Table 4.2 : Comparison table for RO4232 and RO4003 substrates with relative permittivity 3.2 and 3.55, respectively.....	59
Table 4.3 : Comparison of resonant modes when changing thickness of dielectric material .....	59
Table 4.4 : Two cases with different dielectric loss tangent.....	60
Table 4.5 : The first 10 resonant frequencies for two capacitor values .....	61
Table 4.6 : Comparison of some stirrer shapes.....	62
Table 4.7 : Antennas specification and frequency band for some reverberation chamber calibration .....	67
Table 4.8 : Some available LPDA antennas with specification of frequency range and size.....	68
Table 4.9 : Frequency bands and sizes of horn antennas .....	68
Table 4.10 : Standard deviation (in dB) for antenna in position of case 1, metallic chamber, for 12, 18 and 36 stirrer angles, and for 27 locations of field probe .....	73
Table 4.11 : Standard deviation (in dB) for antenna in position of case 1, metallic chamber, for 36 stirrer angles, and for 9, 15 and 27 locations of field probe .....	74
Table 4.12 : Standard deviation (in dB) for antenna in position of case 1, case 2 and case 3, metallic chamber, for 36 stirrer angles and for 9 positions of field probe.....	75

Table 4.13 : Standard deviation (in dB) for antenna in position of case 1, metamaterial chamber, for 36 stirrer angles and for 9 positions of field probe.....	75
Table 6.1 : The first 20 resonant frequencies for isotropic walls distant from 1.90m .....	119
Table 6.2 : The first 20 resonant frequencies for isotropic walls distant from 2.58m .....	120
Table 6.3 : The first 20 resonant frequencies for isotropic walls distant from 2.91 m .....	121



# Chapter 1: Introduction

In this chapter, some electromagnetic compatibility testing environments are introduced. The application domain, the advantages and disadvantages of each chamber is discussed. Then, a focus is done on reverberation chamber with the presentation of the problem statements, the objective and the methodology of research. At the end of this chapter, the dissertation contribution and the thesis structure are presented.

## Content

---

1.1.	Electromagnetic interference and measurement environment .....	16
1.1.1.	Open Area Test Site (OATS).....	16
1.1.2.	Anechoic Chamber (AC) .....	17
1.1.3.	Reverberation Chamber (RC) .....	18
1.2.	Problem statement and research motivation .....	18
1.3.	Research objective and methodology .....	19
1.4.	Dissertation contribution and structure .....	19

## **1.1. Electromagnetic interference and measurement environment**

The electromagnetic interference [1] is one of the complex problem in modern technology. The source of the ElectroMagnetic Interference (EMI) could be a man-made source that interferes on the devices/systems through various parts (conducting coupling, inductive coupling, capacitive coupling and the radiated coupling) or a natural source (solar radiation and lightning strike). The natural EMI sources are generally not significant since many solutions have been already developed to solve those problems. The EMI effects can cause either small variation of the operation of nearby device or serious failure of the device or the system no more working properly. Some examples of the EMI effect are the error of the radio/television's reception signal, the error of the transmitted data in digital transmission system, the delay/fault/failure of the production line due to error in the control system, malfunction of the medical electronic equipment, failure operation of the automotive electronic control board, the inaccuracy of navigation equipment, the malfunction of the explosive system, etc.

From the beginning of the third industrial revolution known as the digital revolution, the electrical and electronic device usage in industry as well as in daily life has grown exponentially. In addition, more frequency bands and/or high operation frequencies are occupied by several electronic devices. The digital devices operating with high frequency clock and switch have rapidly increased. Hence, problems with the electromagnetic interference also became significant issues. As a result, electromagnetic interferences are more complex.

Many problems with the electromagnetic interference are observed and included in methods and tools to solve them [2]. Even if it is included in design, to avoid EMI/EMC problem, measurement methods [3, 4] are also proposed to evaluate the field emission to strengthen the immunity of the device. These methods are done by using some testing environment for the EMI/EMC applications. The test objective is to guarantee the normal operation of the device with other nearby devices or systems. The test is used to confirm that the devices are designed or installed correctly following the specific standard requirements. For these EMC tests, several kind of chambers are created and standard rules are defined for each chamber validation and test operation. Some testing environments/chambers are presented in the following part.

### **1.1.1. Open Area Test Site (OATS)**

The Open Area Test Site [5] is a large open space with almost perfect reflective floor (the shape and size of this reflective floor is not infinite and can be defined against the measurement conditions [6]), usually located far away from any surrounding structure, which can cause reflection, as well as from any man-made interference source. The OATS can be used for the immunity test [7] and the emission test [8] of the electronic devices and the measurement of the antenna [9].

The advantage of the OATS is its low cost, since it needs few equipment (transmitter/receiver antenna, a signal generator, a spectrum analyzer/a network analyzer, a turntable and a metallic

ground plane). No specific walls are necessary [10]. The available large space [5] for the Equipment Under Test (EUT) is also a main advantage.

However, some disadvantages of the OATS are also to be mentioned. With the requirement of the large free space area, transportation time and cost need to be added for the test operation if the company location is far away from the OATS site (considering the office normally in the city and the test site need to be constructed in rural area where less electromagnetic interference signal exists from the nearby structure and man-made electromagnetic interference source). The tester must also be an expert to distinguish the interference signal from the test signal on the EUT. Additional electromagnetic wave from the sources due to surrounding environment can penetrate into the EUT. This phenomenon leads to measurement errors. These interference waves come from some source such as the radio transmitter, TV, mobile phone tower, etc. Moreover, difficulties exist to find the suitable site that must be far away without ambient radio signals. The site is also sensitive to the effect from the natural sources like wind and rain. There are still unwanted signals from the ground or from any structure close to the OATS since there is no 100% clearance space. Finally, the strong radiated electric field for immunity test may get out from the site and interfere with things nearby since the site has no wall (This condition is not recommended by the regulation of the radio communication body).

### **1.1.2. Anechoic Chamber (AC)**

The Anechoic Chamber [11] is a chamber acting as free space environment to perform EMC tests of the electronic components, devices or systems. The chamber is constructed by using Radiation Absorbers Materials (RAM) [12, 13] inside a Faraday cage to absorb the incident wave into the chamber walls, so that there is no reflection from the walls to the Equipment Under Test. Generally, there are two types of anechoic chamber: the Full Anechoic Chamber (FAC) [14] where all walls are covered by absorbers materials and the Semi-Anechoic Chamber (SAC) [15] where the floor is not covered by the electromagnetic absorbers. Normally, the performance of the anechoic chamber is related to the reflection properties and the arrangement of the RAM [16]. The applications of the AC are the electromagnetic compatibility tests which refer to the radiated emission [17] and radiated immunity measurement [18], the antenna radiation pattern measurement [19] and the radar cross-section measurement [20, 21].

The advantage of the anechoic chamber is the isolation from the intrusive electromagnetic wave from the surrounding environment thanks to the metallic room. The results are repeatable since the chamber structure is fixed compared to the OATS. Moreover, since the radiated electric field from the excitation antenna cannot get out from the metallic room, there is no problem with the radio communication regulation when strong electric fields are needed for the immunity test. The maintenance cost is also low compared to the OATS. The chamber is not affected by weather conditions compared to the OATS. The disadvantage of the AC is its price since the RAM are expensive.

### **1.1.3. Reverberation Chamber (RC)**

The reverberation chamber [11] is another kind of testing environment composed only of metallic walls and stirrer to mix the electromagnetic field in the chamber. The chamber is used for EMC tests while the over-mode condition in the working volume is reached. The reverberation chambers have been commonly used for several applications [22]. Those applications include the radiated immunity test [18, 23], the radiated emission test [24], the measurement of the material shielding effectiveness [25], the antenna radiation pattern measurement [26]. In the design of 4G/5G applications, the chamber can also be used as the wireless channel emulator [27].

According to the structure of the reverberation chamber, it is more convenient for construction compared to the anechoic chamber. The construction cost is also lower since there are no radiation absorbers materials inside.

The disadvantage of the reverberation chamber is that its lowest usable frequency is still high even with large size chamber because many modes must resonate in the same frequency range to get fields homogeneity and so to use the chamber to test devices. Since the number of resonant modes is increasing with frequency, the 60th resonant mode frequency is first considered as criteria. Moreover, the measurement results need complex method for the extraction of the EUT sensitivity to electromagnetic interferences as presented in [26, 28].

Beside the three testing environments described above, there are testing environments such as the TEM cell [29, 30], the GTEM cell [30-32], etc.

After this short introduction of the electromagnetic measurement environments, the reverberation chamber is interesting because it can emulate different environments. Currently, this chamber is used in many EMC tests more than other chamber tests and will be used for more applications in the future. Therefore, this thesis is focused on this chamber improvement.

## **1.2. Problem statement and research motivation**

According to the principle of the reverberation chamber, the operation at low frequency implies large chamber size [33]. With large chamber size, to get suitable field strength, high gain power amplifier is required. For small size device test, small reverberation chamber can be preferred, where lower power can also be injected. Under this condition, the space for chamber and the material used for chamber construction are reduced which significantly affects the construction cost, the mobility of the chamber and the power amplifier. In contrary, the disadvantage of the small chamber is the measurement frequency band which is moved to high frequencies.

To extend the RC band to lower frequencies, metamaterials [34] are of interest. Metamaterials are artificial materials fabricated by using a periodic structure. They can present properties such as the Single Negative (SNG) metamaterial [35, 36] or the Double Negative (DNG) metamaterial [37], depending on the negative sign of the effective permittivity and/or permeability. Such

properties do not exist in nature. The properties of the metamaterial depend on the shape and/or size of the elementary cell that is periodically repeated, and acts on the transmission and reflection properties of the incident electromagnetic field [38]. Metamaterial are used in antenna reflector [38], metamaterial cloaking [39] or the metamaterial super-lens [40], the metamaterial waveguide [41, 42] and many other applications. Metamaterial can be used as reverberation chamber walls, according to the investigation and the experiment in [43-46] to lower the LUF, it is adjusted from 288 MHz to 165 MHz. This study provides the important guideline to further investigate the application of metamaterial for reverberation chamber walls. Normally, the properties of metamaterial are difficult to predict. Additionally, the analysis and optimization of the metamaterial walls on the chamber require large amount of times and computational resources. So, it is interesting to use an efficient method for the analysis of the reverberation chamber with metamaterial walls. The Modal Expansion Theory (MET) method [47] has been used for the analysis of waveguide with metamaterial walls [41, 42] efficiently. This method will be modified for the analysis of the reverberation chamber with metamaterial walls in this thesis.

### **1.3. Research objective and methodology**

The objective of this thesis is to construct a small reverberation chamber by using the metamaterial as walls to operate at lower frequencies than with metallic RC. To accomplish this objective, the modal expansion theory will be used to analyze reverberation chamber with metamaterial walls. In this method, metamaterials are represented by anisotropic surface walls. So, several values of surface impedance will be tested in the RC to find the proper walls to adjust the operating band of the RC.

In order to reduce the complexity, the scope is limited to two parallel metamaterial walls while other parts of chamber are kept metallic. To finalize the prototype of the reverberation chamber with this topology of the metamaterial walls, the chamber components such as the stirrer, the excitation antenna and location of field probe, will be reviewed, analyzed and designed. The prototype of the small reverberation chamber with and without the metamaterial walls will be constructed for the measurement validation.

### **1.4. Dissertation contribution and structure**

The originality of this work is related to the MET as analysis tool to find the type of metamaterial to be inserted as walls on the reverberation chamber. This work will contribute to the development in the research field of the electromagnetic compatibility as well as the telecommunication since the reverberation chamber can be used for several applications in both field. The advantage for the EMC is that more electronic devices are produced in small size so that there is no need to construct large testing chamber, it will therefore save resources and money. For the telecommunication sector, the small chamber can be used to test small antenna that are used for the 4G and 5G applications since this chamber emulates real world urban environment better than other testing chamber. Additionally, the MET method for analysis of the reverberation chamber with metamaterial walls is proposed for the first time in this condition. By using this MET

method, the type and location of the metamaterial walls are selected. This method can be improved for optimization of the metamaterial RC by hybridization with FEM simulation of the unit cell to take into account the frequency-dependency of surface impedances.

In this research work, the small reverberation chamber with and without the metamaterial walls is designed, analyzed and experimentally characterized. The validation method by using VNA and electric field probe is also operated. This small chamber is expected to operate from low frequency, so that the small device can be tested on a wide range.

This manuscript is divided into five chapters. In chapter 2, the reverberation chamber characteristics and challenges are discussed. This chapter defines the structure and components in the chamber, the chamber's properties, the standardized qualification of the reverberation chamber and the designed challenges of the reverberation chamber with metamaterial walls. Chapter 3 focuses on the design of the metamaterial unit cell for use as reverberation chamber's walls. In this chapter, the MET is applied to select the metamaterial's type through a sensitivity analysis on the unit cell's surface impedances. Then several structures of the unit cell are simulated to reach the required impedances. Finally, a unit cell is selected for the analysis, simulation and measurement validation. Chapter 4 is related to the sensitivity analysis and characterization of the reverberation chamber prototype. In this part, the chamber materials are selected through sensitivity analysis. Moreover, the stirrer structure, the excitation antenna and the field probe's position are also reviewed, selected and designed. Finally, the prototype of the reverberation chamber with and without the metamaterial walls are tested and compared with the expected results from the simulation. Chapter 5 will conclude on all the results and define the perspectives for the related future work.

# Chapter 2: Reverberation chamber characteristics and challenges

In this chapter, the basic properties of the reverberation chamber will be reviewed. Then the qualification method of the chamber according to the commercial standard IEC 61000-4-21 will be described. Additionally, the reverberation chamber with metamaterial walls will be discussed in the last section of this chapter.

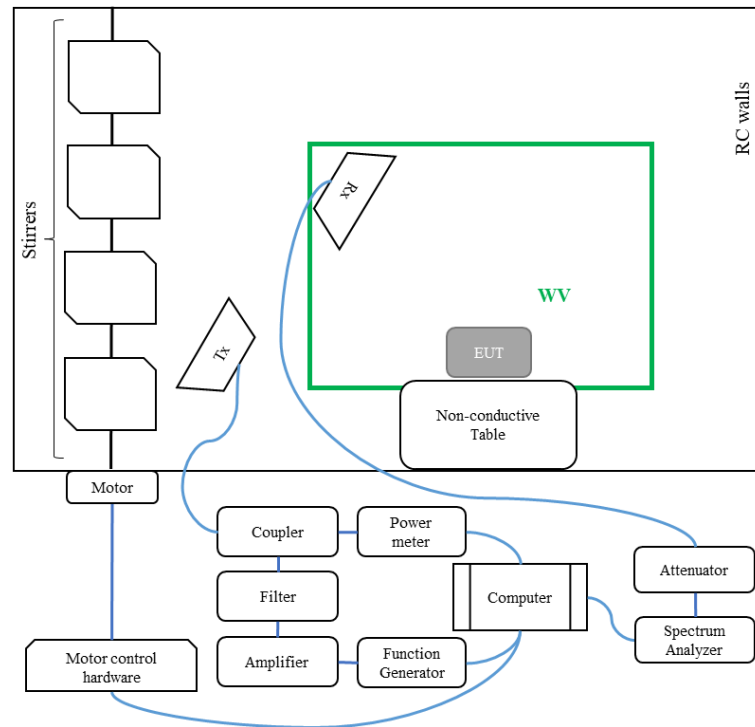
## Content

---

2.1.	Structure and components of the reverberation chamber.....	22
2.2.	Reverberation chamber properties .....	24
2.2.1.	Working Volume .....	24
2.2.2.	Lowest Usable Frequency .....	24
2.2.3.	Quality Factor (Q-factor).....	25
2.3.	Qualification method with standard IEC 61000-4-21.....	26
2.3.1.	Location of field probe .....	27
2.3.2.	Measurement procedure and stored data .....	27
2.3.3.	Standard deviation evaluation .....	28
2.3.4.	LUF assumption with tolerance requirement of the IEC 61000-4-21 .....	30
2.4.	Design challenges of RC with MTMs walls.....	30

## 2.1. Structure and components of the reverberation chamber

The Reverberation Chambers (RC) are constructed in a variety of shapes and sizes. Some are in arbitrary shape, for example, as in [48], the aeronautical metallic hall which has gable roof is converted to be used as the mode-stirred reverberation chamber by adding the rotating metallic paddle inside. Another example is the RC constructed from the thermal vacuum chamber in [49] to give the advantage of EMC test and thermal test simultaneously. So, the shape of these RCs depend on the remaining chamber. Mostly, the reverberation chamber are constructed in rectangular shape [50-53] because this shape is simple for construction and the resonant modes can be known analytically as in [54].



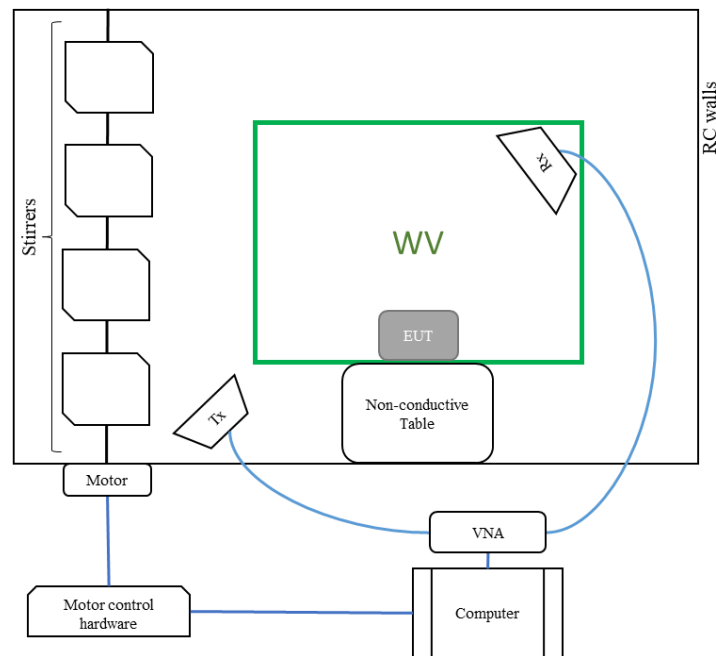
*Figure 2.1 : The typical components of the reverberation chamber [55]*

The minimum frequency from which the RC can operate correctly is named the LUF. Since the reverberation chamber is a resonant cavity, the resonant modes occur at specific frequencies. Figure 2.1 shows the schematic of the reverberation chamber. In the figure, the Equipment Under Test (EUT) is placed in the Working Volume (WV) for measurement. The WV is the region where the electromagnetic field is uniform and isotropic. Inside the chamber, there are one or two stirrers [56], a transmitter antenna, a receiver antenna, some field probes, a non-conductive stand to support the EUT and some power and signal cables to feed the EUT and transfer signals. Outside the chamber, the equipments for generating, monitoring and recording the data are placed so that they are not perturbed by EM radiation. Amongst these equipments, computer is used to control the stirrer position through a board connected to motors for stirrer rotation and also to perform the



field monitoring with connections to the spectrum analyzer at receiver part and through the power meter and function generator at transmitter part. In addition, the attenuators, couplers, filters and amplifiers may be used to control the EM field properties.

There is also alternative combination of components in the reverberation chamber such as in [57, 58], for the validation of the reverberation following the Anderson-Darling Goodness-of-Fit (AD-GoF) method which is different from the IEC 61000-4-21 standard, the required equipments are only the antenna and the Vector Network Analyzer (VNA) [59]. Within this method, the field uniformity evaluation is extracted from the  $S_{11}$  data [57, 58] and/or  $S_{21}$  [60, 61] by the calculated rejection rate and autocorrelation function. Figure 2.2 shows the typical components for validation of reverberation chamber by AD-GoF method.



**Figure 2.2 : Typical components of RC validated by AD GoF method [59]**

The material used as the chamber's walls could be the galvanized steel or the aluminum [62, 63]. For example, the galvanized steel is mostly used for construction of big commercial RC while in small RC, the aluminum is preferred since it is less expensive than copper but has comparable mechanical strength.

The stirrer function is to create various boundary conditions in the chamber so that each stirring state gives different electromagnetic field distributions. The field uniformity condition is created in a dedicated area called the working volume for one stirring cycle. There are many stirring methods that can be categorized into two groups: the mechanical or the electronic mode stirring [64, 65]. The mechanical mode stirring technique refers to the physical movement of components such as paddles or walls [66] of chamber. For example, rotating paddle (the Z-fold [67], the irregular reconfigurable stirrer in [68] and the carousel stirrer shape [69, 70]) and the walls stirring

RC (the VIRC [71], the oscillating quasi-wall stirrer [72, 73]) are in this group. The electronic mode stirring technique refers to a change in the boundary condition of the chamber by using electronic methods. For example, the frequency stirring [74], and source stirring (the random excitation of several antennas stirring [75], the reactively-loaded antennas stirring [76] and the source position stirring [77]).

## **2.2. Reverberation chamber properties**

Three important parameters are considered to design and characterize a reverberation chamber: the Working Volume, the Lowest Usable Frequency (LUF) and the Quality Factor (Q-factor).

### **2.2.1. Working Volume**

The Working Volume is also known as the testing volume. In the WV region [70], the electric field is uniform for one complete rotation of stirrer. Therefore, the Equipment Under Test is placed in WV region during the measurements. Classically, the WV is located inside the RC with a distance of a quarter wavelength at LUF from each chamber wall and metallic parts such as the mechanical stirrer [78].

### **2.2.2. Lowest Usable Frequency**

The lowest frequency of the frequency band used for measurement is defined as the Lowest Usable Frequency. Above this frequency, the electric field in the chamber is supposed homogenous and isotropic in the working volume. The LUF depends on the chamber size. According to the IEC standard for commercial product known as IEC 61000-4-21 [55], the value of the LUF is generally between 3 to 6 times of the cavity first resonant frequency or the LUF can be defined as the resonant frequency of the 60<sup>th</sup> modes. However, some researches select the LUF from the resonant frequency of the 100<sup>th</sup> resonant mode [43, 46] to be confident on the field uniformity. The exact number of resonant modes in the cavity can be numerically calculated in the rectangular case. However, for simple hand calculation, the smooth approximation formula (or the extension of Weyl's formula for the rectangular cavity) of  $N$  resonant mode number in the rectangular cavity is often used to estimate this number in a metallic walls rectangular cavity of size  $(a \times b \times d)$  at specific frequency. From [54], the formula is re-written as:

$$N = \frac{8\pi}{3}(a \times b \times d) \frac{f^3}{c^3} - (a + b + d) \frac{f}{V} + \frac{1}{2} \quad (2.1)$$

where  $N$  is the number of modes having a resonant frequency below  $f$ , with  $f$  the frequency in (Hz),  $c$  the speed of light in vacuum,  $a, b, d$  the dimensions of the chamber and  $V$  the volume of the chamber.

The formula (2.1) gives results similar to the rectangular cavity resonant mode calculation in [54]. For example, the cavity box of size  $30 \text{ cm} \times 40 \text{ cm} \times 50 \text{ cm}$  presents 60 resonant modes up to  $1.5337 \text{ GHz}$  according to analytical calculation and  $1.5223 \text{ GHz}$  with (2.1) formula. Similarly,

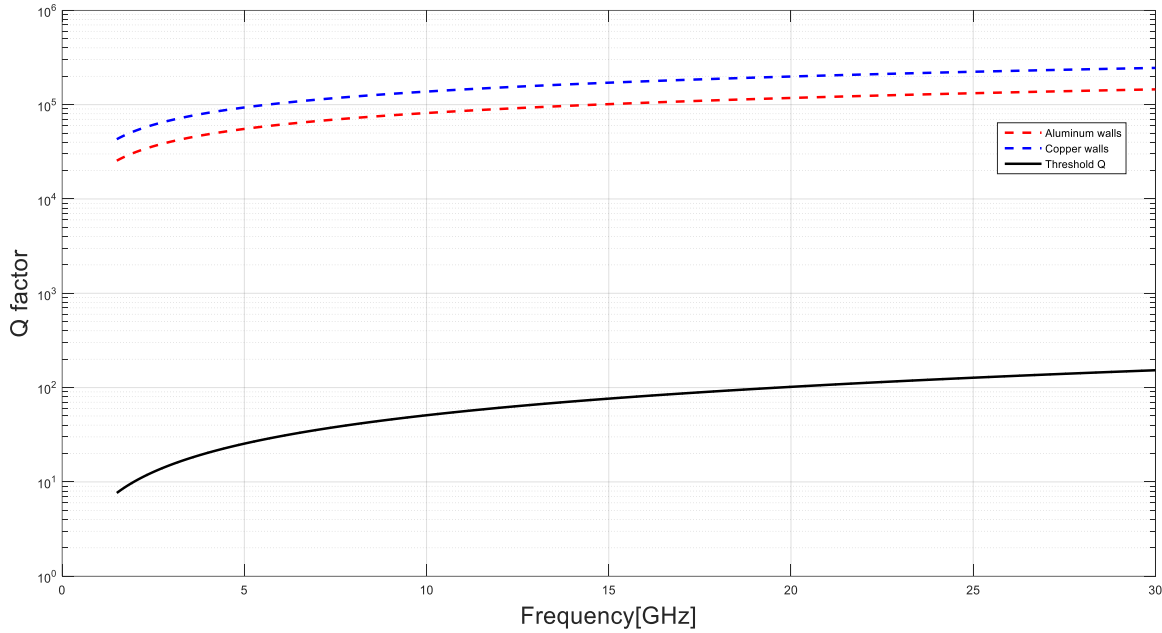
it presents 100 resonant modes up to  $1.7799GHz$  according to analytical calculation and  $1.7887GHz$  with (2.1) formula. In this thesis, the frequency of the 60<sup>th</sup> resonant mode is considered as the LUF definition.

### 2.2.3. Quality Factor (Q-factor)

The Quality Factor (Q-factor) represents the ability of the chamber to store energy during a time period. The value of the chamber Q-factor provides the information for setting the input power to get the required electric field strength for testing operation in the chamber. By definition, the Q-factor of the perfect metallic walls RC is determined by the formula as in [79]:

$$Q(f) = \frac{3}{2} \frac{V}{\mu_r S \delta_s} \frac{1}{1 + \frac{3\pi}{8k} \left( \frac{1}{a} + \frac{1}{b} + \frac{1}{d} \right)} \quad (2.2)$$

where  $S$  is the total inner surface of the chamber,  $\delta_s$  is the skin depth of the material used as chamber walls,  $k$  is the wavenumber where  $k = 2\pi f/c$  and  $\mu_r$  is the relative permeability.



**Figure 2.3 : Quality factor curves of RC with aluminum walls and with copper walls compared to threshold of Q-factor**

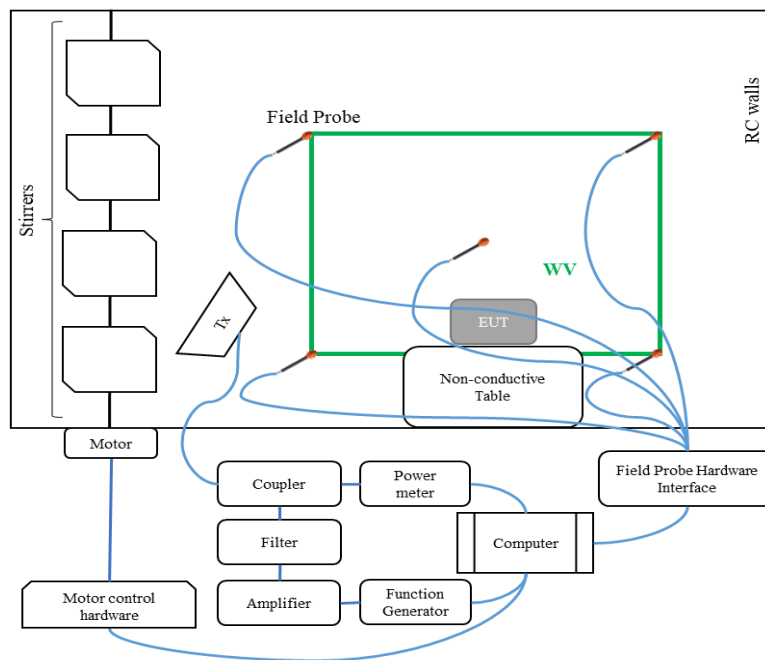
For the cavity box of size  $30\text{ cm} \times 40\text{ cm} \times 50\text{ cm}$ , the Q-factor curves are plotted on Figure 2.3 for aluminum and copper walls. The 60<sup>th</sup> resonant mode of this chamber appears at  $1533.7\text{ MHz}$ . In [80], they show that Q-factor needs to be higher than the threshold value  $Q_{thr}$  to have an effective reverberation chamber that the stirred energy exceeds the unstirred energy throughout most of the chamber volume. This quality factor threshold value is related to the wavelength  $\lambda$  and the chamber volume  $V$  as:

$$Q_{thr} = \left(\frac{4\pi}{3}\right)^{2/3} \frac{V^{1/3}}{2\lambda} \quad (2.3)$$

In Figure 2.3 plot, the Q factor for aluminum and for copper walls RC are compared to this threshold value. It shows that the Q-factor of the aluminum walls RC is comparable with the copper walls RC. Both curves are much higher than the threshold level whatever the frequency. Hence, using aluminum for chamber walls is acceptable and economic compared to copper chamber.

### 2.3. Qualification method with standard IEC 61000-4-21

There are many methods and standards for reverberation chamber calibration [81]. The choice of the validation standard depends on application domains of device that will be tested in the chamber. For example, for space and civil aviation equipment, the RC is validated by the standard RTCA/DO-160G [82]. Generally, the standard IEC 61000-4-21 [55] is used to qualify the chamber for commercial electronic product. In this thesis, the RC is qualified according to the IEC standard. This standard is reminded in this part.



*Figure 2.4 : Configuration of RC for validation by IEC 61000-4-21*

To validate the value of the RC's LUF by IEC standard, one needs to statistically evaluate the electromagnetic field uniformity properties in the defined working volume. For the metallic walls RC, the region of the working volume is at least at a quarter wavelength (at the LUF frequency) from the metallic walls. The procedure is therefore to extract the LUF from the electric field homogeneity data. With the reference standard IEC 61000-4-21 for reverberation chamber validation, the procedure to get the measurement data and to calculate the standard deviation

parameters in order to evaluate the field uniformity is described in next sub-sections. Figure 2.4 shows the configuration of reverberation chamber validation according to the IEC standard.

### 2.3.1. Location of field probe

As the LUF is the minimum frequency for which the electric field is isotropic and uniformly distributed in the WV, the location of WV needs to be defined. Data are collected with a field probe located at the 8 corners and in the center of the WV. Therefore, 9 positions of E-field probe are normally necessary. Ideally, large number of data points in WV give more accurate estimation of the field uniformity. The field should be measured in all the WV points but it is not reasonably practical because a lot of field probe positions would be required. So, only 9 probe locations will be considered. Figure 2.5 shows the WV and the 9 locations of the field probe represented as FP1 to FP9. Measurements must be done for each FPi and each polarization successively since only one probe is available.

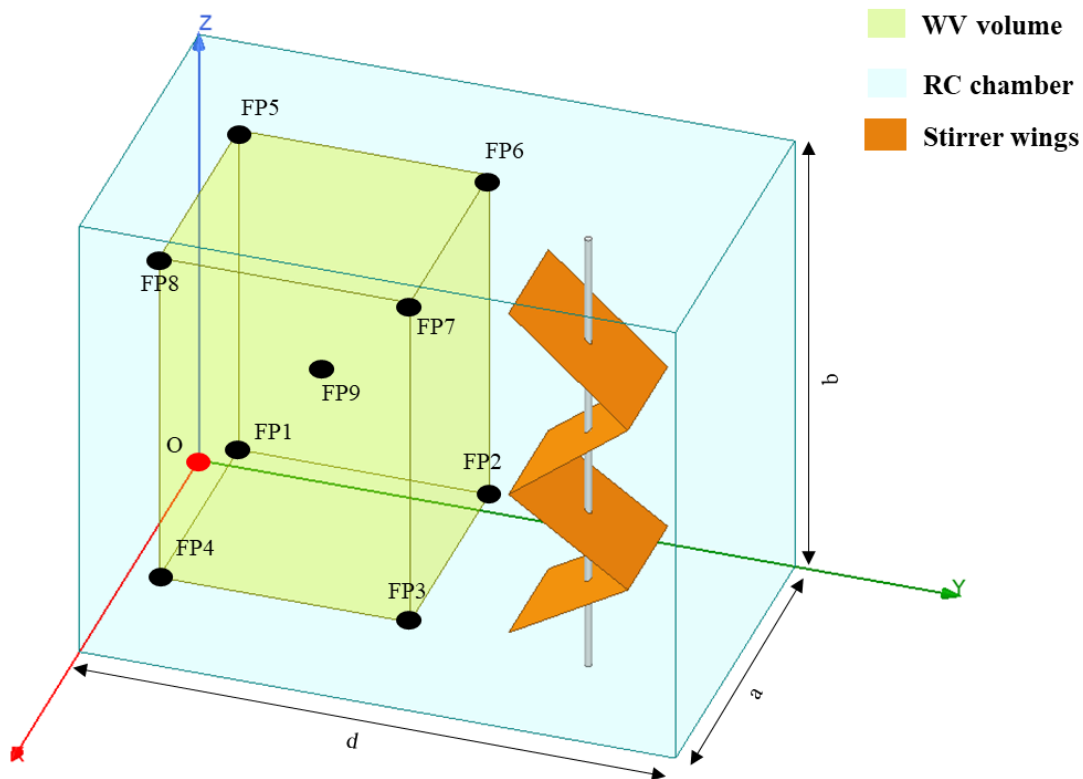


Figure 2.5 : Field Probe locations in the RC

### 2.3.2. Measurement procedure and stored data

In order to get significant measurement data, stirrer positions and frequency points in the band must be set according to IEC 61000-4-21. They are reported in Table 2.1. The  $f_s$  is the starting frequency with value around 3 times of the first resonant mode. The table shows that from

frequency  $f_s$  to  $3f_s$ , a measurement must be stored for at least stirrer positions separated by 30 degrees. In the band ( $f_s \rightarrow 3f_s$ ), the recommended frequency samples are 20 log spaced. This standard gives the rule for stirrer positions and sample frequencies up to more than  $10f_s$ .

**Table 2.1 : The required number of stirrer positions and the sample frequencies according to IEC 61000-4-21**

Frequency band	Minimum number of stirrer step angle	Number of log spaced frequency for each band
$f_s \rightarrow 3f_s$	12	20
$3f_s \rightarrow 6f_s$	12	15
$6f_s \rightarrow 10f_s$	12	10
$> 10f_s$	12	20/decade

During the RC qualification, the collected data are:

- The excitation frequencies
- The angular position of the stirrer
- The magnitude of E-field in the three axis ( $E_x, E_y, E_z$ ) by using polarized field probe
- The input and reflected powers

The reflected power needs to be considered when it is significant. Otherwise, only the input power is required in the normalization of the electric field as in the formula (2.4) to (2.6).

### **2.3.3. Standard deviation evaluation**

To evaluate the E-field uniformity property in the WV, one needs to calculate the standard deviation from the measurement data stored for a cycle of the stirrer at each excitation frequency.

Considering that the stirrer has  $N + 1$  positions corresponding to  $0, \varphi_1, \dots, \varphi_N$  angles. The maximum of E-field's magnitude amongst all the stirrer positions for each  $p$  position of the field probe is written [83]:

$$\hat{E}_{x,p} = \frac{\max_{0 \leq \varphi \leq \varphi_N} \|\vec{E}_{x,p}\|}{\sqrt{P_{input}}} \quad (2.4)$$

$$\hat{E}_{y,p} = \frac{\max_{0 \leq \varphi \leq \varphi_N} \|\vec{E}_{y,p}\|}{\sqrt{P_{input}}} \quad (2.5)$$

$$\hat{E}_{z,p} = \frac{\max_{0 \leq \varphi \leq \varphi_N} \|\vec{E}_{z,p}\|}{\sqrt{P_{input}}} \quad (2.6)$$

where  $\varphi$  is the stirrer angle position,  $p$  is the location of field probe,  $P_{input}$  is the input power.

The average value of the E-field magnitude from M positions  $p_1, p_2, \dots, p_9, \dots, p_M$  of the field probe is calculated as:

$$\langle \hat{E}_x \rangle_M = \frac{\sum_{p=p_1, \dots, p_M} \hat{E}_{x,p}}{M} \quad (2.7)$$

$$\langle \hat{E}_y \rangle_M = \frac{\sum_{p=p_1, \dots, p_M} \hat{E}_{y,p}}{M} \quad (2.8)$$

$$\langle \hat{E}_z \rangle_M = \frac{\sum_{p=p_1, \dots, p_M} \hat{E}_{z,p}}{M} \quad (2.9)$$

Supposed  $\langle \hat{E} \rangle_{3M}$  represents the average value of all E-field for M positions of field probe and for the 3 components of electric field. It is calculated as:

$$\langle \hat{E} \rangle_{3M} = \frac{\sum_{p=p_1, \dots, p_M} \sum_{i=x,y,z} \hat{E}_{i,p}}{3M} \quad (2.10)$$

Then the standard deviations are calculated for the different polarizations and the mean value of E-field by the formula:

$$\sigma_x = \sqrt{\frac{\sum_{p=p_1, \dots, p_M} (\hat{E}_{x,p} - \langle \hat{E}_x \rangle_M)^2}{M-1}} \quad (2.11)$$

$$\sigma_y = \sqrt{\frac{\sum_{p=p_1, \dots, p_M} (\hat{E}_{y,p} - \langle \hat{E}_y \rangle_M)^2}{M-1}} \quad (2.12)$$

$$\sigma_z = \sqrt{\frac{\sum_{p=p_1, \dots, p_M} (\hat{E}_{z,p} - \langle \hat{E}_z \rangle_M)^2}{M-1}} \quad (2.13)$$

$$\sigma_{3M} = \sqrt{\frac{\sum_{p=p_1, \dots, p_M} \sum_{i=x,y,z} (\hat{E}_{i,p} - \langle \hat{E} \rangle_{3M})^2}{3M-1}} \quad (2.14)$$

Finally, the standard deviation relative to the mean value in *dB* form is calculated as:

$$\sigma_{x,dB} = 20 \log_{10} \left[ \frac{\sigma_x + \langle \hat{E}_x \rangle_M}{\langle \hat{E}_x \rangle_M} \right] \quad (2.15)$$

$$\sigma_{y,dB} = 20 \log_{10} \left[ \frac{\sigma_y + \langle \hat{E}_y \rangle_M}{\langle \hat{E}_y \rangle_M} \right] \quad (2.16)$$

$$\sigma_{z,dB} = 20 \log_{10} \left[ \frac{\sigma_z + \langle \hat{E}_z \rangle_M}{\langle \hat{E}_z \rangle_M} \right] \quad (2.17)$$

$$\sigma_{3M,dB} = 20 \log_{10} \left[ \frac{\sigma_{3M} + \langle \hat{E} \rangle_{3M}}{\langle \hat{E} \rangle_{3M}} \right] \quad (2.18)$$

### **2.3.4. LUF assumption with tolerance requirement of the IEC 61000-4-21**

The standard deviation value is then compared to the standard IEC 61000-4-21 requirement recalled in Table 2.2. From 80 MHz to 100 MHz, the standard deviation value must be lower than 4 dB. The requirement decreases linearly from 4 dB at 100 MHz to 3 dB at 400 MHz. From the frequency higher than 400 MHz, the requirement is set to 3 dB. The LUF is the frequency upon which the requirement is met.

*Table 2.2 : The tolerance requirement of the standard deviation according to IEC 61000-4-21 [55]*

Frequency	Tolerance requirement for standard deviation
80 MHz -100 MHz	4 dB
100 MHz – 400 MHz	4 dB at 100 MHz, decreasing linearly to 3 dB at 400 MHz
Higher than 400 MHz	3 dB

### **2.4. Design challenges of RC with MTMs walls**

When designing the conventional metallic walls reverberation chamber, one needs to consider some factors such as the material used for chamber walls, the stirring technique [64, 84], the type and the structure of the stirrer and also the source and receiver antenna choice [85].

For the material, the electrical and the mechanical properties need to be rightly selected. One important electrical property is the conductivity of the walls, since it is related to the RC quality factor. The Q-factor influences the field uniformity in the chamber [80]. One important mechanical property of the walls material is its hardness since it affects the RC strength.



The selection of the stirring technique must be suitable with chamber size and structure. One common stirring technique is the rotating paddle, the stirrer has also some effects on the field uniformity of the RC [86, 87]. In order to design the chamber with rotating paddle, one needs to consider the structure, size and the number of stirrer [56]. Some stirrers have been simulated or measured for performance comparison in [88-91]. The comparison shows that the z-fold stirrer is suitable for implementation in our project since it has simple structure and gives good field uniformity. For selection of the stirrer structure, some criteria have been proposed in [92]. Even though many other criteria exist, the [92] criteria are chosen in this thesis to design the stirrer. The location of the stirrer is also studied in [93]. The study shows that stirrer locations have less effect on the field uniformity but it is better to select their position so that the working volume is optimized.

Another factor to consider is the type of antenna for emission and reception. Some wideband antennas [94-96] or multiple antennas operating in various frequency bands [53] are used when one antenna cannot cover all the frequency band. Another parameter is the size of the antenna. The antenna is usually inserted in the chamber and must be considered to define the RC working volume for EUT. Small antennas are mandatory for small RC.

Additionally, the chamber peripherals such as the hardware and software control on stirrer movement also need to be included in the RC design. Moreover, the measurement equipment to connect to the transmitter part and the receiver part are also carefully selected for suitable operation frequency.

To design the reverberation chamber with metamaterial walls, the type and structure of the metamaterial are included in the RC design. Its design is one of the challenge since there are variety of metamaterials. So, before constructing the real prototype of the chamber, new RC must be analyzed with numerical and simulation models.

# Chapter 3: Design of the metamaterial unit cell

In the first part of this chapter, the modal expansion theory (MET) method has been modified to analyze the reverberation chamber with anisotropic walls. In this method, the 2D metamaterial can be represented by anisotropic surface impedances. The second part of the chapter will focus on the design and characterization of the metamaterial unit cell which will be used for the chamber walls.

## Content

---

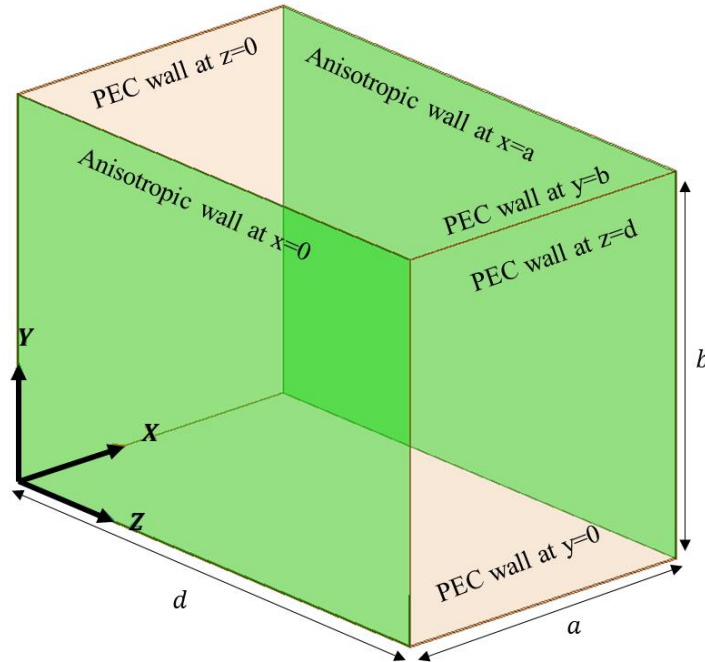
3.1.	MET for the analysis of anisotropic walls reverberation chamber .....	33
3.1.1.	Analysis of anisotropic walls reverberation chamber .....	33
3.1.2.	Validation of the MET method.....	38
3.1.3.	Sensitivity analysis to the surface impedance .....	41
3.2.	Design and characterization of the metamaterial unit cell.....	41
3.2.1.	Unit cell structures.....	42
3.2.2.	Metamaterial unit cell design .....	46
3.2.3.	Characterization of the metamaterial unit cell.....	50
3.3.	Conclusion .....	54

### 3.1. MET for the analysis of anisotropic walls reverberation chamber

The modal expansion theory method can be used to analyze the propagation model of the electromagnetic field in waveguides [42, 97] or resonant cavities. In this method, the impedance boundary condition is used to link the electromagnetic field components. The MET method for the analysis of the anisotropic walls waveguide is explained in [47]. It helps to study the properties of the propagation mode at frequency lower than the first resonant frequency of the conventional waveguide [97]. The MET for the analysis of the reverberation chamber with anisotropic walls is described in the following sub-sections.

#### 3.1.1. Analysis of anisotropic walls reverberation chamber

First, the RC representation is given in the Figure 3.1 below. The walls in the planes  $y = \{0, b\}$  and  $z = \{0, d\}$  are perfect electric conductor (PEC) walls. The anisotropic walls are placed in the planes  $x = \{0, a\}$ .



*Figure 3.1 : Representation of the reverberation chamber with two anisotropic walls*

According to PEC conditions,  $k_y = \frac{n\pi}{b}$  stands for the phase constant along y direction;  $k_z = \frac{p\pi}{d}$  stands for the phase constant along z direction. So,  $\gamma_z = jk_z = j\frac{p\pi}{d}$  is the propagation constant along z direction. The  $n$  and  $p$  parameters are integers. According to the anisotropic representation of the walls at  $x = 0$  and at  $x = a$ , the propagation constant along x direction is represented by the variable  $\gamma_x$  which is unknown and needs to be found to get the resonant modes in the cavity.

### 3.1.1.1. Surface impedance boundary conditions

As mentioned in [47], the anisotropic boundary condition is defined as:

$$\vec{E}_t = Z_s (\vec{H}_t \times \vec{n}) \quad (3.1)$$

where  $\vec{E}_t$  is the tangential electric field on the anisotropic wall,  $\vec{H}_t$  is the tangential magnetic field on the anisotropic wall,  $\vec{n}$  is the normal vector to this wall oriented outside the cavity.

This impedance  $Z_s$  is decomposed in tangential and a longitudinal components at  $x = 0$  and  $x = a$ . They are noted  $(Z_{t1}; Z_{z1})$  and  $(Z_{t2}; Z_{z2})$  respectively. So, the boundary conditions at the anisotropic walls of the chamber can be written as in (3.2) to (3.5)

$$\left. \frac{E_y}{H_z} \right|_{x=0} = -Z_{t1} \quad (3.2)$$

$$\left. \frac{E_y}{H_z} \right|_{x=a} = Z_{t2} \quad (3.3)$$

$$\left. \frac{E_z}{H_y} \right|_{x=0} = Z_{z1} \quad (3.4)$$

$$\left. \frac{E_z}{H_y} \right|_{x=a} = -Z_{z2} \quad (3.5)$$

Since all the boundary conditions are defined, the field components will be expressed in the next part to get the equations for the resonant frequencies of the reverberation chamber with metamaterial walls.

### 3.1.1.2. Analysis with the modal expansion theory

In this analysis,  $z$  axis is supposed to be the longitudinal direction of the electromagnetic field in the cavity. All the electromagnetic field components can be written as:

$$E_i = E_i^+ + E_i^- \quad (3.6)$$

$$H_i = H_i^+ + H_i^- \quad (3.7)$$

with  $i = x, y, z$

The first part of the expression corresponds to the propagation waves in +z direction and the second part in -z direction.

**The purpose in this part is to focus on the  $E_i^+, H_i^+$  terms.**

From Maxwell equation in **annex 6.1.1**, transverse components can be expressed as function of the longitudinal field by:

$$(\gamma_z^2 + k_0^2 \epsilon_r) \vec{E}_T^+ = -\gamma_z (\nabla_T E_z^+) - j\omega\mu_0 (\nabla_T H_z^+) \times \vec{z} \quad (3.8)$$

$$(\gamma_z^2 + k_0^2 \epsilon_r) \vec{H}_T^+ = j\omega\epsilon_0 \epsilon_r (\nabla_T E_z^+) \times \vec{z} - \gamma_z (\nabla_T H_z^+) \quad (3.9)$$

With  $\vec{E}_T^+, \vec{H}_T^+$  the transverse field components propagating in +z direction. And  $\gamma_z^2 + k_0^2 \epsilon_r = k_c^2$ . Considering the boundary conditions along y, the PEC conditions impose a  $\sin(k_y y)$  for  $E_z^+$  and a  $\cos(k_y y)$  for  $H_z^+$ . The variation in x condition is supposed to be the superposition of both components.

$$E_z^+ = [\alpha_1 \cosh(\gamma_x x) + \alpha_2 \sinh(\gamma_x x)] e^{-\gamma_z z} \sin(k_y y) \quad (3.10)$$

$$H_z^+ = [\beta_1 \cosh(\gamma_x x) + \beta_2 \sinh(\gamma_x x)] e^{-\gamma_z z} \cos(k_y y) \quad (3.11)$$

with  $\alpha_1, \alpha_2, \beta_1, \beta_2$  four unknown complex coefficients.

Introducing (3.10) and (3.11) in (3.8), it yields to:

$$E_y^+ = \frac{1}{k_c^2} \left[ -\gamma_z \frac{\partial E_z^+}{\partial y} + j\omega\mu_0 \frac{\partial H_z^+}{\partial x} \right] \quad (3.12)$$

$$E_y^+ = \frac{e^{-\gamma_z z} \cos(k_y y)}{k_c^2} [-\gamma_z k_y \cosh(\gamma_x x) \alpha_1 - \gamma_z k_y \sinh(\gamma_x x) \alpha_2 + j\omega\mu_0 \gamma_x \sinh(\gamma_x x) \beta_1 + j\omega\mu_0 \gamma_x \cosh(\gamma_x x) \beta_2] \quad (3.13)$$

Inserting (3.10) and (3.11) in (3.9), it yields to:

$$H_y^+ = \frac{1}{k_c^2} \left[ -j\omega\epsilon_0 \frac{\partial E_z^+}{\partial x} - \gamma_z \frac{\partial H_z^+}{\partial y} \right] \quad (3.14)$$

$$H_y^+ = \frac{e^{-\gamma_z z} \sin(k_y y)}{k_c^2} [-j\omega\epsilon_0\gamma_x \sinh(\gamma_x x)\alpha_1 - j\omega\epsilon_0\gamma_x \cosh(\gamma_x x)\alpha_2 + \gamma_z k_y \cosh(\gamma_x x)\beta_1 + \gamma_z k_y \sinh(\gamma_x x)\beta_2] \quad (3.15)$$

Up to this section, all the necessary components for the surface impedance conditions  $E_y^+, H_y^+, E_z^+$  and  $H_z^+$  are expressed.

**A similar work is done for the  $E_i^-, H_i^-$  terms**

Equation (3.8), (3.9) are similar in this case and recalled:

$$(\gamma_z^2 + k_0^2 \epsilon_r) \vec{E}_T^- = \gamma_z (\nabla_T E_z^-) - j\omega\mu_0 (\nabla_T H_z^-) \times \vec{z} \quad (3.16)$$

$$(\gamma_z^2 + k_0^2 \epsilon_r) \vec{H}_T^- = j\omega\epsilon_0 \epsilon_r (\nabla_T E_z^-) \times \vec{z} + \gamma_z (\nabla_T H_z^-) \quad (3.17)$$

With  $E_T^-, H_T^-$  the transverse field components propagating in  $-z$  direction.

$$E_z^- = [\alpha_1 \cosh(\gamma_x x) + \alpha_2 \sinh(\gamma_x x)] e^{+\gamma_z z} \sin(k_y y) \quad (3.18)$$

$$H_z^- = [-\beta_1 \cosh(\gamma_x x) - \beta_2 \sinh(\gamma_x x)] e^{+\gamma_z z} \cos(k_y y) \quad (3.19)$$

Introducing (3.18) and (3.19) in (3.16), it yields to:

$$E_y^- = \frac{1}{k_c^2} \left[ \gamma_z \frac{\partial E_z^-}{\partial y} + j\omega\mu_0 \frac{\partial H_z^-}{\partial x} \right] \quad (3.20)$$

$$E_y^- = \frac{e^{+\gamma_z z} \cos(k_y y)}{k_c^2} [\gamma_z k_y \cosh(\gamma_x x)\alpha_1 + \gamma_z k_y \sinh(\gamma_x x)\alpha_2 - j\omega\mu_0 \gamma_x \sinh(\gamma_x x)\beta_1 - j\omega\mu_0 \gamma_x \cosh(\gamma_x x)\beta_2] \quad (3.21)$$

Inserting (3.18) and (3.19) in (3.17), it yields to:

$$H_y^- = \frac{1}{k_c^2} \left[ -j\omega\epsilon_0 \frac{\partial E_z^-}{\partial x} + \gamma_z \frac{\partial H_z^-}{\partial y} \right] \quad (3.22)$$

$$H_y^- = \frac{e^{+\gamma_z z} \sin(k_y y)}{k_c^2} [-j\omega\varepsilon_0\gamma_x \sinh(\gamma_x x)\alpha_1 - j\omega\varepsilon_0\gamma_x \cosh(\gamma_x x)\alpha_2 + \gamma_z k_y \cosh(\gamma_x x)\beta_1 + \gamma_z k_y \sinh(\gamma_x x)\beta_2] \quad (3.23)$$

The complete expression is recombined thanks to (3.6) and (3.7)

$$E_y = \frac{\cos(k_y y) \sinh(\gamma_z z)}{k_c^2} [\gamma_z k_y \cosh(\gamma_x x) A_1 + \gamma_z k_y \sinh(\gamma_x x) A_2 - j\omega\mu_0\gamma_x \sinh(\gamma_x x) B_1 - j\omega\mu_0\gamma_x \cosh(\gamma_x x) B_2] \quad (3.24)$$

$$H_y = \frac{\sin(k_y y) \cosh(\gamma_z z)}{k_c^2} [-j\omega\varepsilon_0\gamma_x \sinh(\gamma_x x) A_1 - j\omega\varepsilon_0\gamma_x \cosh(\gamma_x x) A_2 + \gamma_z k_y \cosh(\gamma_x x) B_1 + \gamma_z k_y \sinh(\gamma_x x) B_2] \quad (3.25)$$

with  $A_1 = 2\alpha_1, A_2 = 2\alpha_2, B_1 = 2\beta_1, B_2 = 2\beta_2$ .

Also the recombination of the longitudinal components gives, thanks to (3.6) and (3.7):

$$E_z = \cosh(\gamma_z z) \sin(k_y y) [A_1 \cosh(\gamma_x x) + A_2 \sinh(\gamma_x x)] \quad (3.26)$$

$$H_z = -\sinh(\gamma_z z) \cos(k_y y) [B_1 \cosh(\gamma_x x) + B_2 \sinh(\gamma_x x)] \quad (3.27)$$

The boundary conditions (3.2) to (3.5) are applied on (3.24) to (3.27) fields expression to get the system (3.28) which can be written  $[M] \times [X] = [0]$ . For more details, see Annex 6.2.

$$\begin{bmatrix} M_{11} & M_{12} & M_{13} & M_{14} \\ M_{21} & M_{22} & M_{23} & M_{24} \\ M_{31} & M_{32} & M_{33} & M_{34} \\ M_{41} & M_{42} & M_{43} & M_{44} \end{bmatrix} \times \begin{bmatrix} A_1 \\ A_2 \\ B_1 \\ B_2 \end{bmatrix} = \begin{bmatrix} 0 \\ 0 \\ 0 \\ 0 \end{bmatrix} \quad (3.28)$$

where

$$\begin{aligned} M_{11} &= \gamma_z k_y; & M_{12} &= 0; & M_{13} &= -Z_{t1} k_c^2; & M_{14} &= -j\omega\mu_0\gamma_x; & M_{21} &= \gamma_z k_y \cosh(\gamma_x a); & M_{22} &= \gamma_z k_y \sinh(\gamma_x a); \\ M_{23} &= -j\omega\mu_0\gamma_x \sinh(\gamma_x a) + Z_{t2} k_c^2 \cosh(\gamma_x a); & M_{24} &= -j\omega\mu_0\gamma_x \cosh(\gamma_x a) + Z_{t2} k_c^2 \sinh(\gamma_x a); \\ M_{31} &= k_c^2; & M_{32} &= Z_{z1} j\omega\varepsilon_0\gamma_x; & M_{33} &= -Z_{z1} \gamma_z k_y; & M_{34} &= 0; \\ M_{41} &= k_c^2 \cosh(\gamma_x a) - Z_{z2} j\omega\varepsilon_0\gamma_x \sinh(\gamma_x a); & M_{42} &= k_c^2 \sinh(\gamma_x a) - Z_{z2} j\omega\varepsilon_0\gamma_x \cosh(\gamma_x a); \\ M_{43} &= Z_{z2} \gamma_z k_y \cosh(\gamma_x a); & M_{44} &= Z_{z2} \gamma_z k_y \sinh(\gamma_x a) \end{aligned}$$

In order to get  $\gamma_x$  value, and then the resonant frequencies and the resonant modes, the condition  $\det([M]) = 0$  is imposed. From this condition,  $\gamma_x$  is found. Then the resonant frequency of each resonant mode is computed thanks to  $k_0^2 = -\gamma_x^2 + \left(\frac{n\pi}{b}\right)^2 + \left(\frac{p\pi}{d}\right)^2$ .

### **Special case with zero order modes**

#### **Case ( $n = 0$ & $p \neq 0$ )**

If  $n = 0$ ,  $k_y = \frac{n\pi}{b} = 0$ . So,  $\sin(k_y y) = 0$  and  $\cos(k_y y) = 1$ .

From  $E_z$  expression in (3.26),  $E_z = [A_1 \cosh(\gamma_x x) + A_2 \sinh(\gamma_x x)] \sin(k_y y) \cosh(\gamma_z z) = 0$ , the resonant modes are ruled by  $H_z$ , they are called  $TE_{m0p}$ .

From **annex 6.2.5.1**, the linear system becomes in this case:

$$\begin{bmatrix} -k_c^2 Z_{t1} & -j\omega\mu_0\gamma_x \\ -j\omega\mu_0\gamma_x \sinh(\gamma_x a) + Z_{t2} k_c^2 \cosh(\gamma_x a) & -j\omega\mu_0\gamma_x \cosh(\gamma_x a) + Z_{t2} k_c^2 \sinh(\gamma_x a) \end{bmatrix} \times \begin{bmatrix} B_1 \\ B_2 \end{bmatrix} = \begin{bmatrix} 0 \\ 0 \end{bmatrix} \quad (3.29)$$

#### **Case ( $n \neq 0$ & $p = 0$ )**

If  $p = 0$ ,  $\gamma_z = jk_z = j\frac{p\pi}{d} = 0$ . So,  $\sinh(\gamma_z z) = 0$  and  $\cosh(\gamma_z z) = 1$  resulting in  $H_z = [-B_1 \cosh(\gamma_x x) - B_2 \sinh(\gamma_x x)] \cos(k_y y) \sinh(\gamma_z z) = 0$  from equation (3.27). The modes are ruled by  $E_z$  only. So, the resonant modes are  $TM_{m0}$  modes.

From the same procedure as in the previous section, the formula becomes:

$$\begin{bmatrix} k_c^2 & Z_{z1} j\omega\varepsilon_0\gamma_x \\ k_c^2 \cosh(\gamma_x a) - Z_{z2} j\omega\varepsilon_0\gamma_x \sinh(\gamma_x a) & k_c^2 \sinh(\gamma_x a) - Z_{z2} j\omega\varepsilon_0\gamma_x \cosh(\gamma_x a) \end{bmatrix} \times \begin{bmatrix} A_1 \\ A_2 \end{bmatrix} = \begin{bmatrix} 0 \\ 0 \end{bmatrix} \quad (3.30)$$

### **3.1.2. Validation of the MET method**

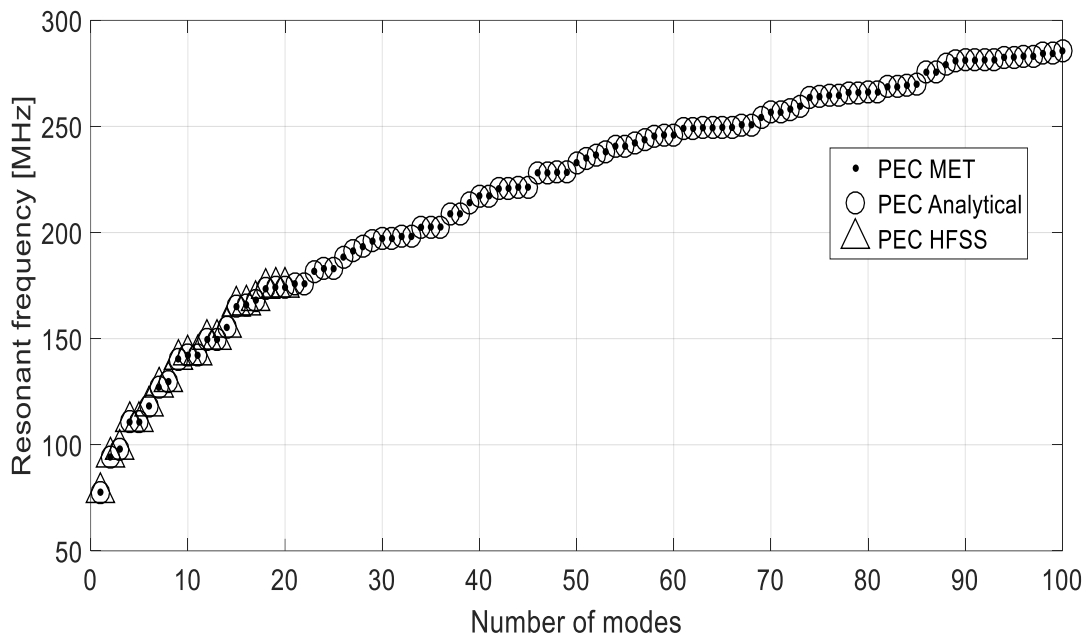
To validate this model, resonant frequencies of two cases are computed with the analytical MET in-house code and compared to the analytical theory results of the resonant modes in rectangular cavity for one case (metallic walls) and compared to ANSYS-HFSS simulation results for the other case (isotropic walls).



The reverberation chamber dimension is  $a \times b \times d = 1.90 \text{ m} \times 2.58 \text{ m} \times 2.91 \text{ m}$ . The value of the surface impedance here is considered as constant over different frequency points and incident angles.

### 3.1.2.1. Metallic walls or PEC case ( $Z_t = Z_z = 0 \Omega$ )

In the first case, the value of the surface impedance of the walls at  $x = 0$  and at  $x = a$  are set as  $Z_{t1} = Z_{z1} = 0 \Omega$  and  $Z_{t2} = Z_{z2} = 0 \Omega$ . This case is equivalent to the case of the chamber with all metallic walls or PEC case. So, the results of the resonant frequencies from the MET method in this case can be compared to the resonant mode frequency results from the analytical theory of the rectangular cavity as in [98].



*Figure 3.2 : The resonant frequencies of the PEC walls RC*

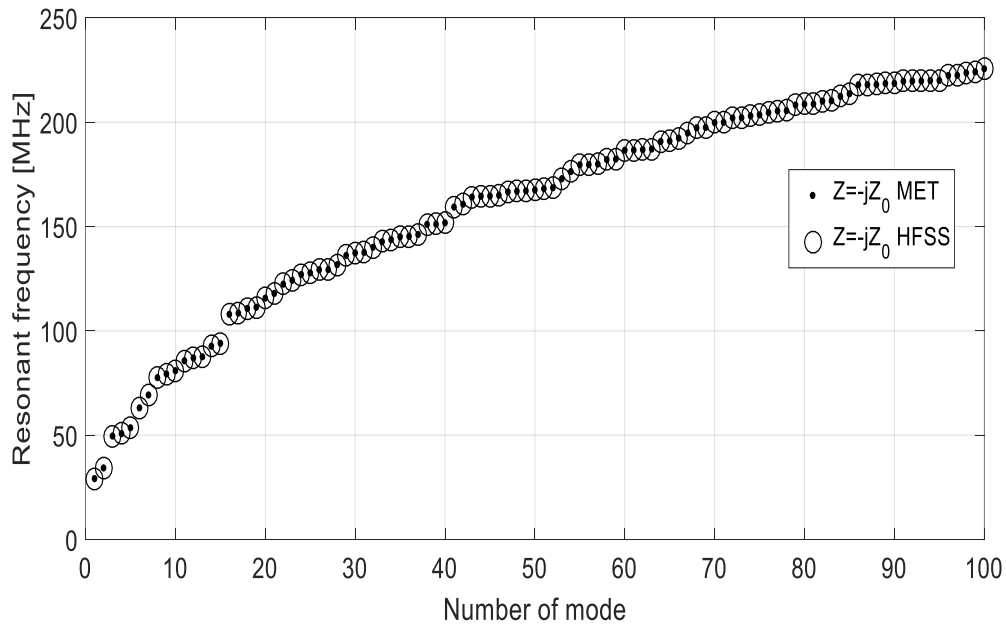
The LUF in this analysis is considered as the frequency of the 60<sup>th</sup> resonant mode. The resonant frequency obtained with the MET method and the rectangular cavity theory sorting from low to the high frequency are plotted in Figure 3.2 for comparison purpose. Because the main purpose in this section is to validate the MET method with the exact solution from the rectangular cavity theory, only the first 20 frequencies are extracted from the HFSS simulation. The HFSS simulation is done with Eigen-mode solver with the conditions  $\Delta f = 0.01 \%$  accuracy, maximum 30 number of pass and solved for 20 number of modes. With CPU Core i5 @ 2.3 GHz RAM 12 GB, it spends 2mn44s for simulation with HFSS for all the 20 modes. It is only 1mn 52s for 100 resonant modes computation with MET in MATLAB with the same computer.

The results show that the resonant frequencies from the MET method coincide well with those from the exact solution. The first 20 resonant frequencies of both methods fit well with results

from the Eigen mode solver of the commercial software (ANSYS-HFSS). The LUF value found in this case is 246 MHz. Additionally, the MET computational method is faster than HFSS simulation.

### 3.1.2.2. Isotropic walls case (with $Z_t = Z_z = -jZ_0$ )

In this section, one isotropic case is chosen to validate the MET method by comparison with HFSS results. In this case, the values of the surface impedance at the walls  $x = 0$  and walls  $x = a$  are chosen as  $Z_{t1} = Z_{z1} = Z_t = -jZ_0$  and  $Z_{t2} = Z_{z2} = Z_z = -jZ_0$  where  $Z_0 = 120\pi \Omega$ . Since no exact solutions exist, results from the commercial software ANSYS-HFSS are used as reference for comparison.



**Figure 3.3 : Resonant frequencies in the RC with two isotropic walls  $Z_t = Z_z = -jZ_0$**

Figure 3.3 shows the MET and HFSS results comparison. A good agreement between these two methods is shown. So, MET can be used confidently to compute the number of resonant modes in the isotropic walls reverberation chamber. It should be noticed that for the case of  $Z_t = Z_z = -jZ_0$ , the LUF is 186 MHz for 60 resonant modes. A reduction is observed by using the metamaterial walls instead of the PEC walls ( $LUF = 246$  MHz). With the same computer specification as in the PEC case, the simulation parameters in HFSS are  $\Delta f = 0.01$  % accuracy, 30 maximum number of pass and for 3 to 6 modes per simulation. With simulation until 100 modes, it takes 58mn2s with HFSS simulation for all 100 modes (with 3 to 5 modes for 1 simulation) and only 3mn2s by MET for all the 100 modes in one time.

### 3.1.3. Sensitivity analysis to the surface impedance

In this section, the reverberation chamber LUF with two anisotropic walls is analyzed according to the surface impedance variations. The MET method is used to provide the LUF since its computation time is lower than the Eigenmode solver of Ansys-HFSS.

In this analysis,  $Z_t$  the transversal component and  $Z_z$  the longitudinal component of the anisotropic impedance walls are substituted with several values to get their effect on the chamber LUF. Table 3.1 shows the resulting LUF values from several combinations of surface impedance. Here, the values are set to  $Z_{t1} = Z_{t2} = Z_t$  and  $Z_{z1} = Z_{z2} = Z_z$ .

**Table 3.1 : LUF table for first 60 resonant modes of the anisotropic walls reverberation chamber**

Frequency of the 60th resonant mode		$Z_z/(jZ_0)$							
		1	0.5	0.25	0.1	-0.1	-0.25	-0.5	-1
$Z_t/(jZ_0)$	1	202MHz	214MHz	218MHz	225MHz	214MHz	211MHz	196MHz	223MHz
	0.5	214MHz	225MHz	230MHz	234MHz	219MHz	218MHz	196MHz	205MHz
	0.25	220MHz	230MHz	235MHz	238MHz	224MHz	210MHz	198MHz	195MHz
	0.1	223MHz	236MHz	237MHz	244MHz	218MHz	214MHz	184MHz	190MHz
	-0.1	217MHz	223MHz	223MHz	223MHz	120MHz	152MHz	129MHz	163MHz
	-0.25	208MHz	212MHz	212MHz	192MHz	172MHz	75MHz	119MHz	157MHz
	-0.5	197MHz	197MHz	189MHz	167MHz	129MHz	124MHz	131MHz	159MHz
	-1	224MHz	203MHz	188MHz	192MHz	165MHz	146MHz	155MHz	186MHz

In table 3.1, cells in green correspond to the surface impedance cases that allow good LUF reduction compared to the PEC case (246 MHz). The cell in blue is the best reduction of the LUF. This region corresponds to negative surface impedance components. This sign represents a capacitive metamaterial. In this region, the minimum LUF value is 75 MHz for  $Z_t = Z_z = -j0.25Z_0$ . Compared to the PEC case LUF, the reduction presents a factor 3.

### 3.2. Design and characterization of the metamaterial unit cell

To achieve at the end a prototype in the laboratory and observe a significant reduction of the LUF, the cavity size is changed for  $W \times H \times L = 30 \text{ cm} \times 40 \text{ cm} \times 50 \text{ cm}$ . This size will be kept until the end of the thesis. According to the section 3.1, to reduce the LUF, the metamaterial walls should present a small negative imaginary surface impedance. In this part, the required unit cell is designed and characterized to meet this criterion. First, some unit cell structures are introduced and analyzed to highlight which structure can present the required surface impedance. Then the selected structure of unit cell has been simulated and analyzed. Finally, validation samples are proposed and measured.

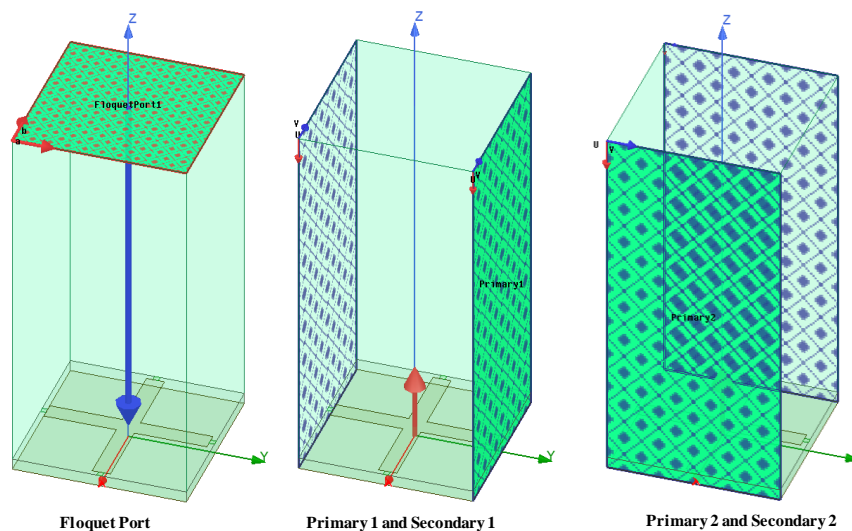
### 3.2.1. Unit cell structures

Several unit cell structures are simulated to qualify their surface impedances. Table 3.2 shows a list of unit cell structures. A *Floquet port* simulation as shown in Figure 3.4 is performed with *Master/Slave boundaries* in commercial software ANSYS HFSS to qualify them. The impedance results are obtained with the de-embedding from the top surface of the metamaterial unit cell.

If the imaginary part of surface impedance walls is considered as negative constant as  $-j94.25 \Omega$ , the LUF will be reduced from  $1.53 \text{ GHz}$  (in the PEC case) to  $454 \text{ MHz}$  for  $60^{\text{th}}$  resonant mode and  $582 \text{ MHz}$  for  $100^{\text{th}}$  resonant mode criteria (in the metamaterial case). Since the general metamaterial cannot present constant impedance for the whole frequency band, the frequency of  $600 \text{ MHz}$  is considered as the baseline for the unit cell design. Hence, the unit cell must be designed to present a capacitive value below  $600 \text{ MHz}$  and up to  $1.5 \text{ GHz}$ .


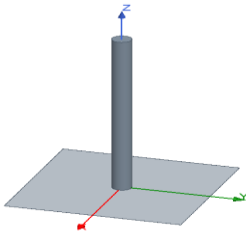
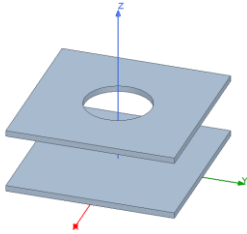
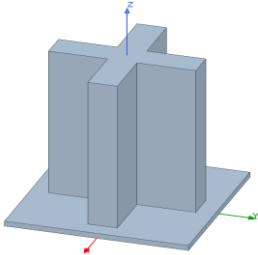
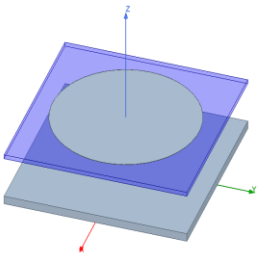
For small reverberation chamber box with size  $30 \text{ cm} \times 40 \text{ cm} \times 50 \text{ cm}$ , the metamaterial walls must be placed on the opposite walls distant of  $30 \text{ cm}$ , since the best LUF reduction is observed in this case with the explanation in **Annex 6.5**. The metamaterial walls have a  $40 \text{ cm} \times 50 \text{ cm}$  size.

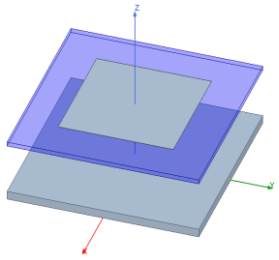
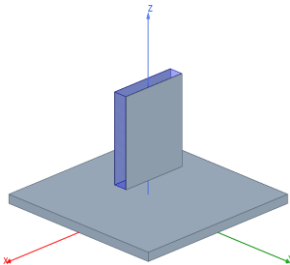
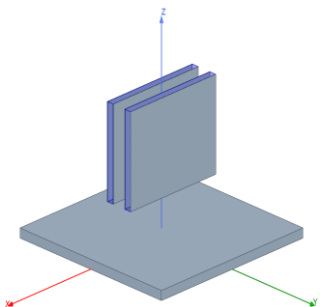
The unit cell size is supposed to be close to  $\lambda/20$ , the length and width of the unit cell are  $L_{\text{cell}} = W_{\text{cell}} = 2.5 \text{ cm}$ , to have many cells ( $16 \text{ cells} \times 20 \text{ cells}$ ) on the reverberation chamber walls. First, to find the suitable structure of the unit cell, the simulation is only done for normal incident angle. Then, one suitable structure is selected. So, the oblique incidence for special angle is studied to see the varying properties of the unit cell. All the simulations to study the surface impedance of one-unit cell is done by using the periodic boundary conditions.

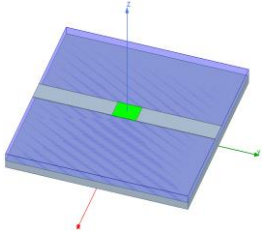


*Figure 3.4: One example of unit cell simulation using Floquet port and Master/Slave (Primary/Secondary) boundary conditions*

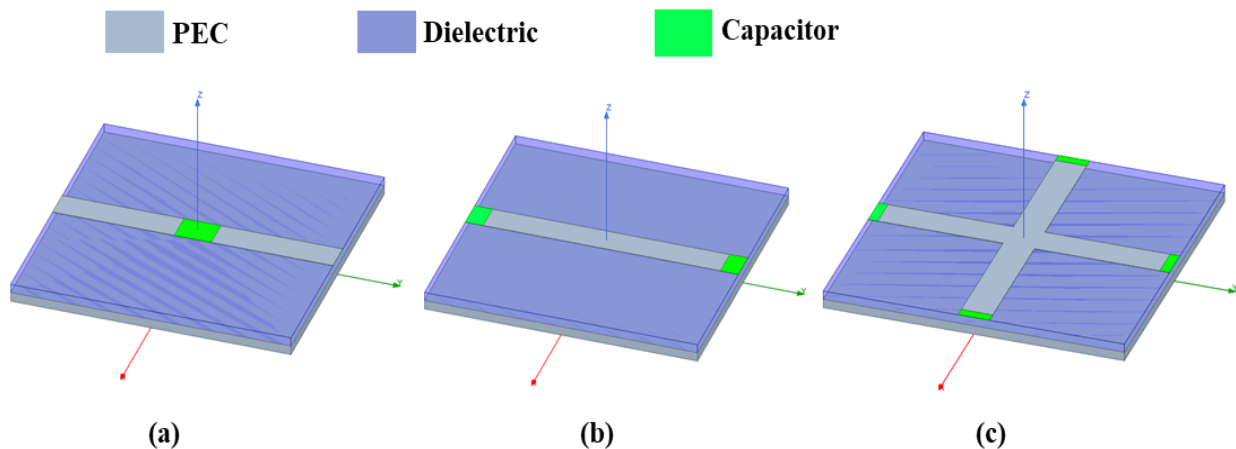
**Table 3.2 : Some structures of unit cell for observation of resonant frequency for specific parameters value**

No	<b>Unit Cell Structure</b> 	Parameters Values	Resonant Frequency	Observation
1.		<ul style="list-style-type: none"> <li>- Height of the via (1 mm)</li> <li>- Radius of the via (50 mm)</li> </ul>	1.57 GHz	Resonant frequency is too high after several parameter tests
2.		<ul style="list-style-type: none"> <li>- Radius of the circular hole on the square roof (5 mm)</li> <li>- Height of the roof from the ground plane (10 mm)</li> </ul>	2.19 GHz	Resonant frequency is too high after several parameter tests
3.		<ul style="list-style-type: none"> <li>- Height of the vertical bar (30 mm)</li> <li>- Width of the vertical bar (4 mm)</li> <li>- Length of the vertical bar (20 mm)</li> </ul>	2.47 GHz	Resonant frequency is too high after several parameter tests
4.		<ul style="list-style-type: none"> <li>- Radius of the circular roof (12.4 mm)</li> <li>- Height of the circular roof from the ground plane (10 mm)</li> <li>- Substrate RO3003 (<math>\epsilon_r = 3, \tan\delta =</math></li> </ul>	2.20 GHz	Resonant frequency is too high after several parameters test

		0.0013) with thickness $508 \mu m$		
5.		<ul style="list-style-type: none"> <li>- Side of square patch on the roof (<math>2.49 \text{ mm}</math>)</li> <li>- The height of the roof above the ground plane (<math>30 \text{ mm}</math>)</li> <li>- Substrate RO3003 (<math>\epsilon_r = 3, \tan\delta = 0.0013</math>) with thickness <math>508 \mu m</math></li> </ul>	400 MHz	Low resonant frequency is obtained with large height of the roof.
6.		<ul style="list-style-type: none"> <li>- Height of substrate (<math>10 \text{ mm}</math>)</li> <li>- Length of substrate (<math>10 \text{ mm}</math>)</li> <li>- Distance of substrate to the ground plane (<math>2 \text{ mm}</math>)</li> <li>- Substrate RO3003 (<math>\epsilon_r = 3, \tan\delta = 0.0013</math>) with thickness <math>2 \text{ mm}</math></li> </ul>	3.4 GHz	Resonant frequency is too high after several parameters test.
7.		<ul style="list-style-type: none"> <li>- Height of substrate (<math>10 \text{ mm}</math>)</li> <li>- Length of substrate (<math>24 \text{ mm}</math>)</li> <li>- Distance of substrate to the ground plane (<math>10 \text{ mm}</math>)</li> <li>- Distance between both substrate (<math>2 \text{ mm}</math>)</li> <li>- Substrate RO3003 (<math>\epsilon_r = 3, \tan\delta = 0.0013</math>) with thickness <math>2 \text{ mm}</math></li> </ul>	3.55 GHz	Resonant frequency is too high after several parameters test

8.		<ul style="list-style-type: none"> <li>- Width of line (2.6 mm)</li> <li>- Length of each line (10.85 mm)</li> <li>- Capacitance value (130 pF)</li> <li>- Substrate RO4350 (<math>\epsilon_r = 3.66, \tan\delta = 0.004</math>) with thickness 762 <math>\mu\text{m}</math></li> </ul>	210 MHz	The capacitor value significantly affects the resonant frequency. To lower the frequency, the capacitor value must be high.
----	---	---	---------	---

Amongst these structures, the unit cell number 8 leads to lower the resonant frequency. This selected structure is chosen to build our unit cell. Several combinations are tested. For example, by shifting capacitor location from center to the sides as in Figure 3.5 (b) or using half capacitor for each side. In this case, the value of capacitor on each side is double compared to the case in Figure 3.5 (a). This new configuration does not change the unit-cell characteristic but allow to synthesize the structure against polarization. Then to ease the capacitor inclusion for both orthogonal polarizations, the unit cell as in Figure 3.5 (c) is simulated. The capacitor value on each side is the same to the case in Figure 3.5 (b). This final unit cell structure can fully support all the electromagnetic field incident from both orthogonal directions.

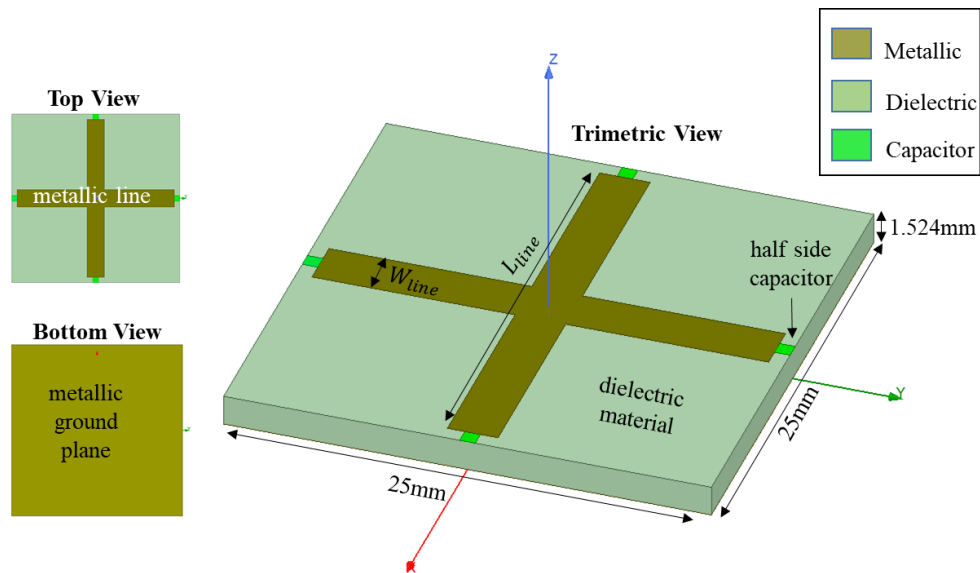


**Figure 3.5 : The modification of the unit-cell with lumped capacitor (a) Capacitor in the center (b) Haft capacitor on both sides (c) The orthogonal line and capacitor are added in both polarization.**

### 3.2.2. Metamaterial unit cell design

#### 3.2.2.1. Simulation model of the cross-bar unit cell with lumped capacitor

The HFSS model of the cross-bar unit cell with lumped capacitors on each side of metallic line is shown in Figure 3.6. The dielectric material is the RO4003 with the permittivity of 3.55, thickness 1.524 mm and loss tangent 0.0021. It should be noticed that this unit cell is not including metallic losses since lines and ground plane have PEC conditions. The selected size of one unit cell is 25 mm x 25 mm resulting in 16 cells x 20 cells on each 40 cm x 50 cm wall. The surface impedance of the unit cell is obtained through the simulation in HFSS by using the *Floquet port* and the Primary/Secondary boundary conditions (alternatively named as the Master/Slave boundary conditions). With the *Floquet port*, the surface impedance has been simulated by setting de-embedding on the surface of the metamaterial cell. The simulation is done by setting maximum accuracy  $\Delta S = 0.005$ . The model of the capacitor here is the 2D sheet which the capacitor value and the direction of the flow current are defined by the user.



**Figure 3.6 : HFSS model of the selected metamaterial surface**

This part of the unit cell design starts by studying the impact of the line widths. The parametric study shows that the effect of the line width can be neglected. So, the width is finally fixed to 2.6 mm to ease the capacitors welding.

The ends of each line are attached to half capacitor since the cell is bounded by periodic walls. The chosen capacitor is the surface mount multilayer ceramic capacitor (SMD MLCCs) from KEMET. The capacitor type is HiQ-CBR Series [99]. This capacitor is commonly used for high power application at RF & Microwave frequency. This capacitor can operate in the frequency band 1 MHz ~ 50 GHz. The available package size of the small capacitor is the package 0402



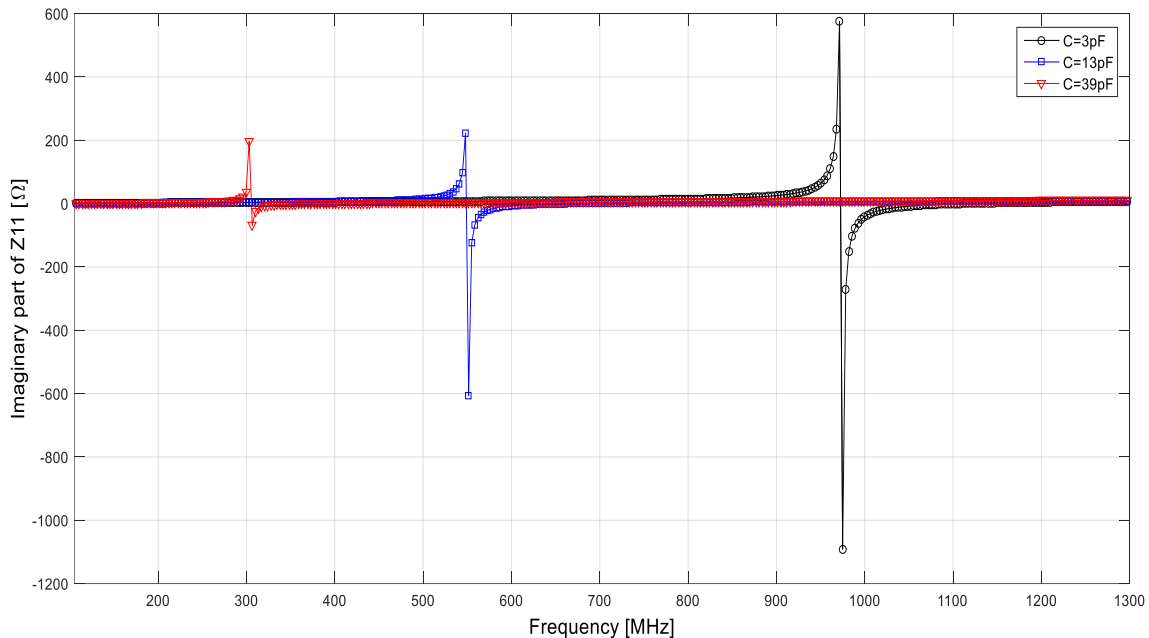
(length = 1 mm, width = 0.5 mm). The capacitor size is respected to the suitable and available product with package size of model 0603 which has 1.6 mm length and 0.8 mm width. The length and the width of each metallic line are chosen as  $L_{line} = 23.4 \text{ mm}$  and  $W_{line} = 2.6 \text{ mm}$ . Table 3.3 shows the structure properties of the unit cell.

**Table 3.3 : Unit cell dimensions**

Parameters	Value
Size of unit cell	25 mm × 25 mm
Substrate thickness	1.524 mm
Metallic film thickness	35 μm
Width of metallic line	2.6 mm
Length of metallic line	23.4 mm

### 3.2.2.2. Sensitivity to the capacitor value

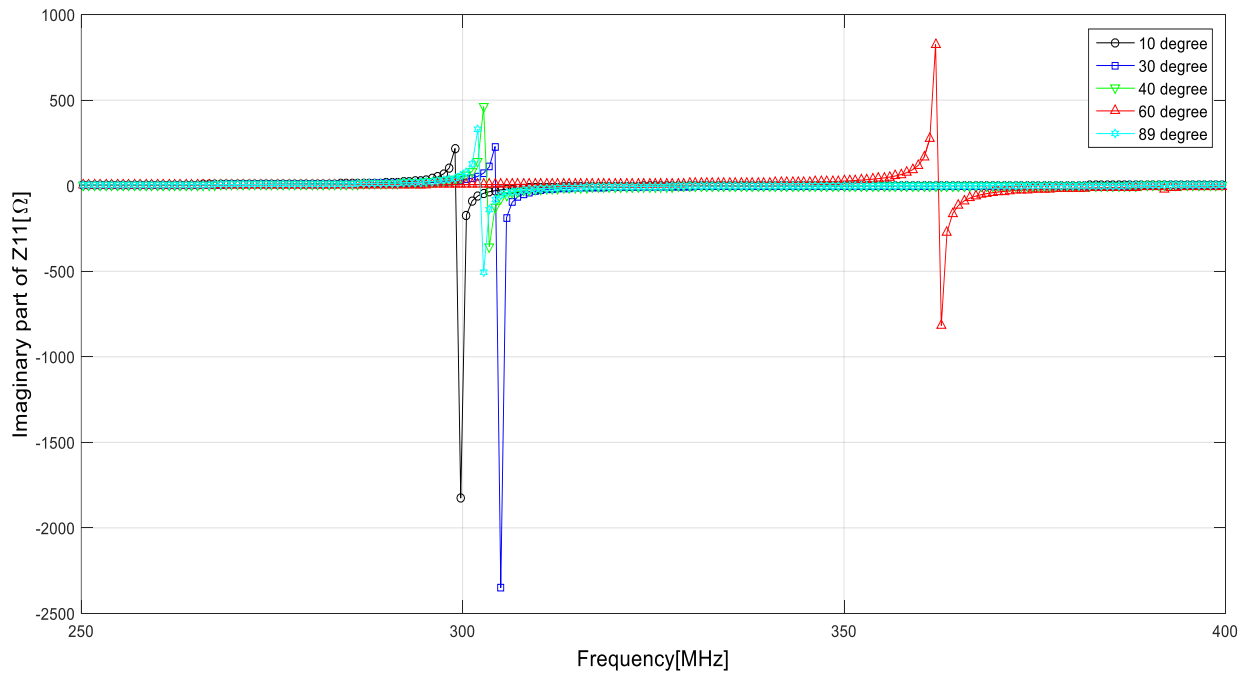
In this section, three different values of capacitor (3 pF, 13 pF and 39 pF) are tested. These values are chosen from the available values in the SMD capacitor data sheet. The purpose is to see how the capacitor affects the resonant frequency of the unit cell. The simulation frequency band is 100 MHz to 1.5 GHz with 401 frequency points (interpolating). The simulation accuracy is set as maximum  $\Delta S = 0.005$ . The analysis is done for normal incidence, so the incident angle of *Floquet port* is set to zero. The simulation result is shown in Figure 3.7. To have capacitor behavior at lowest frequencies, 39 pF capacitor is chosen with a resonant frequency close to 300 MHz. This unit cell is then analyzed with consideration on the incident angle.



**Figure 3.7 : The unit cell surface impedance for 3 different capacitors.**

### 3.2.2.3. Sensitivity to the incident angle

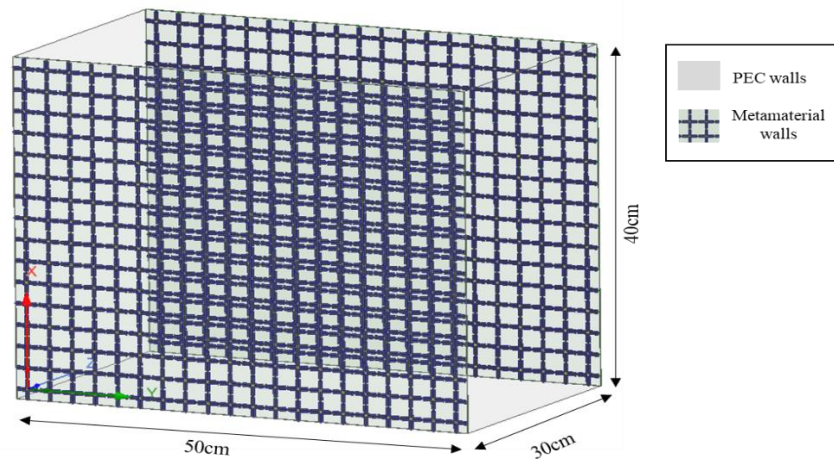
In this section, the effect of the incident angle is observed. The purpose is to evaluate the variation of the unit cell properties according to the incident angle since this angle is different and uncontrolled for each mode. Figure 3.8 shows the impedance variation according to the incident angle. It shows that resonant frequencies change between 300 MHz and 370 MHz. These variations are small. The RC with metamaterial walls shall however be simulated to check if the effect on the LUF is the one attended.



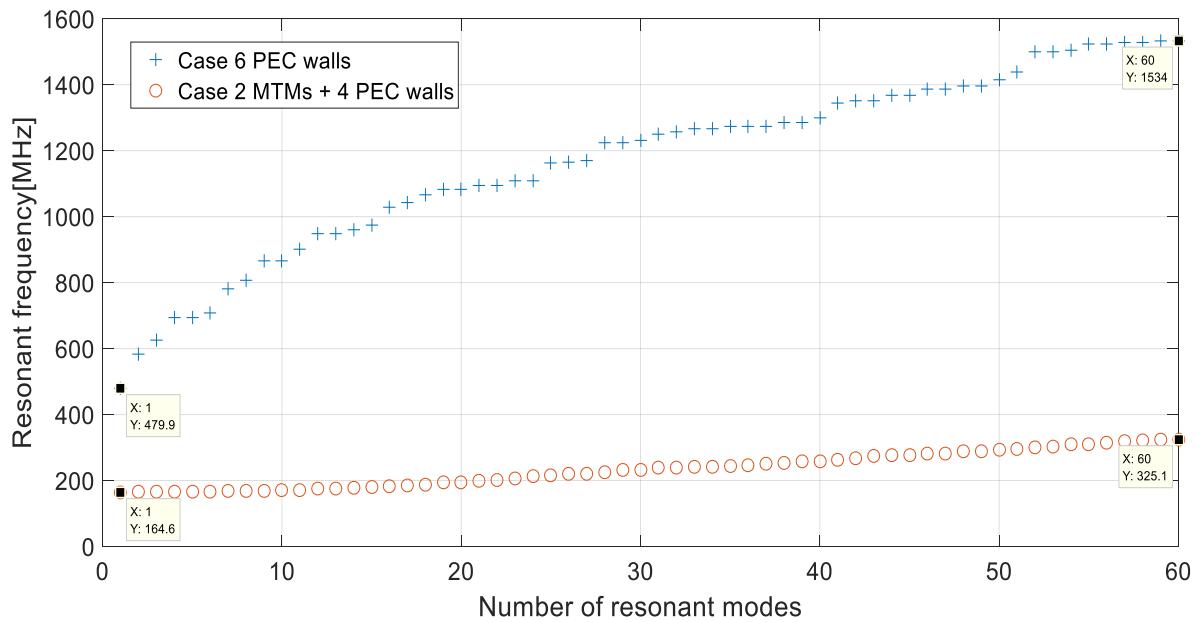
*Figure 3.8 : The surface impedance for different incident angle, capacitor value is 39 pF.*

### 3.2.2.4. Simulation of the reverberation chamber with two metamaterial walls

In this section, the rectangular box of 30 cm x 40 cm x 50 cm size with two metamaterial walls of size 40 cm x 50 cm is tested. It should be reminded that the size of each unit cell is 2.5 cm x 2.5 cm. So, the unit cell number is 16 cells x 20 cells on each wall. The simulation is done with the Eigen-mode solver in HFSS. The simulation model is shown in Figure 3.9 for an accuracy of  $\Delta f = 1 \%$ .



**Figure 3.9 : Rectangular metallic box with two metamaterial walls**



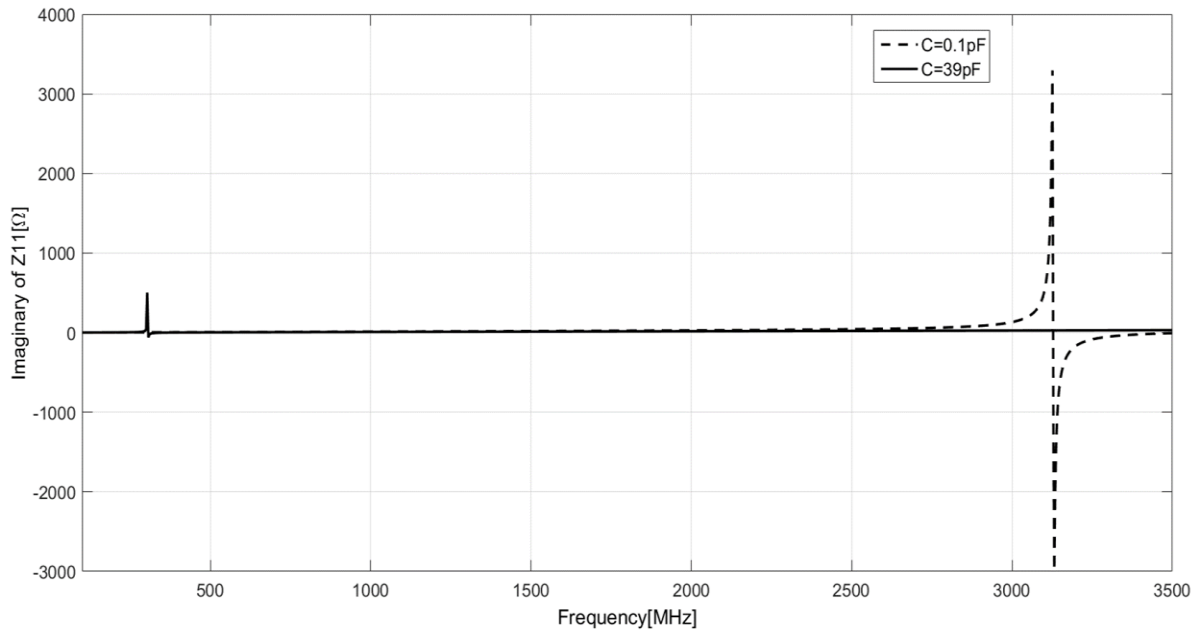
**Figure 3.10 : Resonant mode frequencies for the PEC cavity by theory Vs. Metamaterial cavity simulated with Eigen-mode solver in HFSS**

The resonant frequencies and the LUF for the metamaterial RC are compared to the PEC RC and shown in Figure 3.10. This figure shows that the resonant frequency of the 60<sup>th</sup> resonant mode for the PEC RC is at 1534 MHz while it is at 325.1 MHz for the metamaterial RC. Hence, the metamaterial RC reduces the LUF 5 times compared to PEC RC.

### 3.2.3. Characterization of the metamaterial unit cell

Since a capacitor is needed in the unit cell, its HFSS model is also validated. Two unit cells are therefore embedded on the cross-section of a waveguide for characterization in terms of reflection coefficient ( $S_{11}$ ). The calibration kit used is the waveguide WR229 from the FLANN microwave. The waveguide is 11A440. The waveguide length is  $360.25\text{ mm}$ . The cross section of this waveguide is  $29.08\text{ mm} \times 58.17\text{ mm}$ . According to the calibration kit datasheet, the operation frequency of the waveguide is from  $3.22\text{ GHz}$  to  $4.9\text{ GHz}$ .

First, the capacitor value must be adjusted to have a resonance in this frequency band. Figure 3.11 shows the shift in frequency when the  $39\text{ pF}$  capacitor is replaced with the  $0.1\text{ pF}$  capacitor. For  $0.1\text{ pF}$  capacitor value, the frequency is shifted to  $3.13\text{ GHz}$ . The package size of this capacitor is the package 0402 ( $length = 1\text{ mm}, width = 0.5\text{ mm}$ ) while for the  $39\text{ pF}$  capacitor, it was the package 0603 ( $length = 1.6\text{ mm}, width = 0.8\text{ mm}$ ). These dimensions have been used previously in the last section to simulate the capacitor with a surface polarized impedance. The simulation model and prototype of the two unit cells embedded in the waveguide are modeled, simulated, constructed, measured and compared in the following sub-section.



*Figure 3.11 : Choice of the new capacitor value by simulation with HFSS of the unit cell.*

### 3.2.3.1. Simulation model and prototype

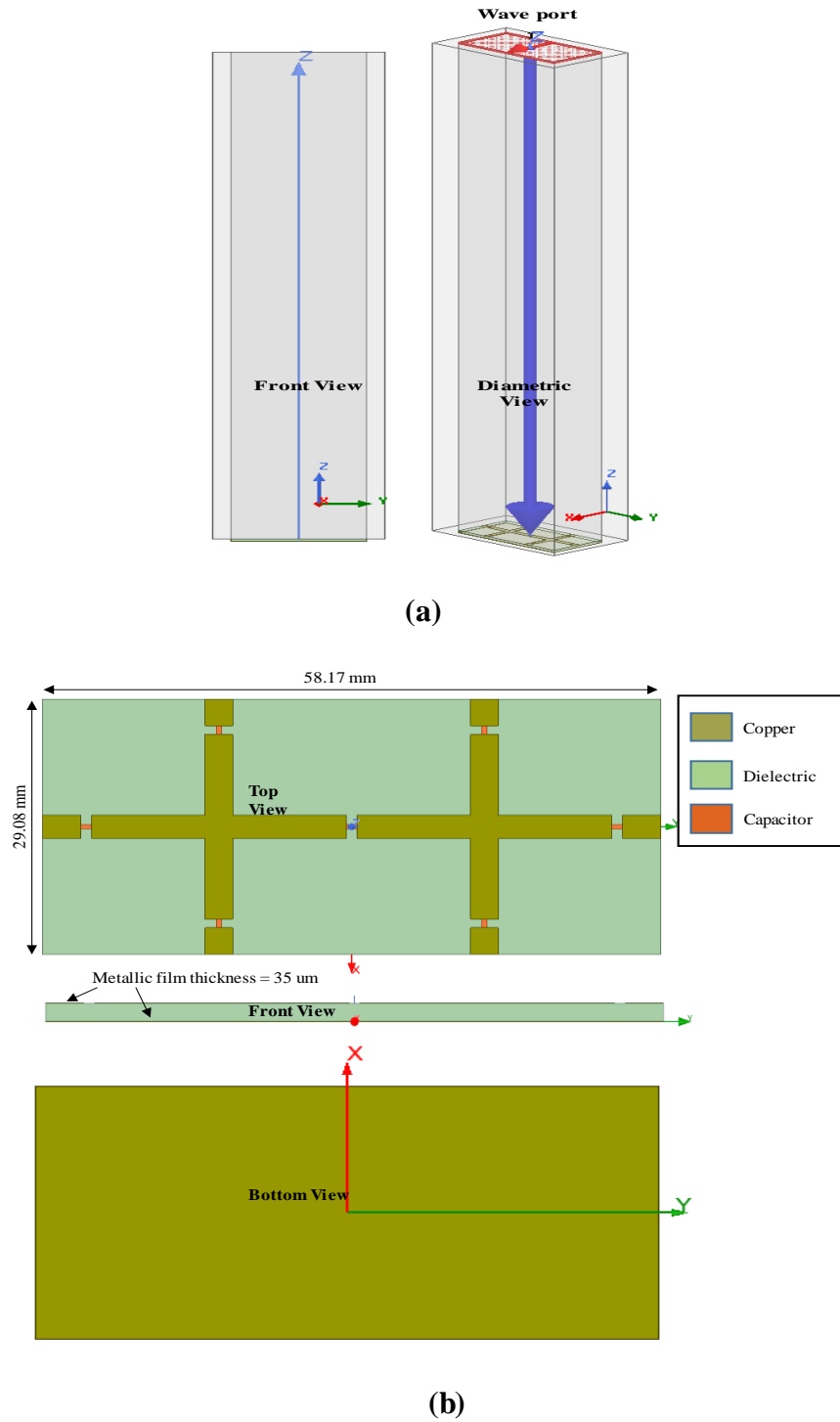
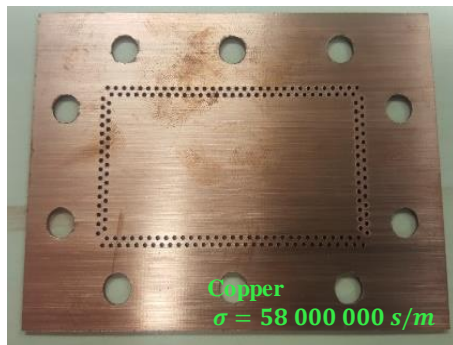


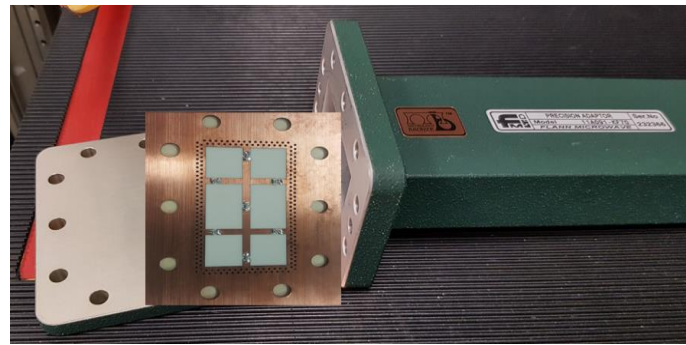
Figure 3.12 : Two unit cells test in waveguide (a) 3D views (b) 2D views

According to the waveguide cross-section, two unit cells are inserted. Since the size of each unit cell is  $25\text{ mm} \times 25\text{ mm}$ , there are remaining gaps that are completed by metallic lines. The model is presented in Figure 3.12.

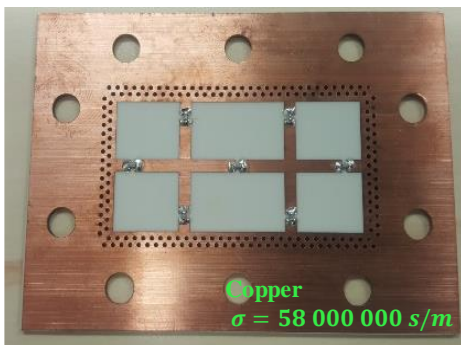
In this model, the copper lines and ground plane have  $35\text{ }\mu\text{m}$  thickness. The waveguide walls is in aluminum with  $8\text{ mm}$  thickness. The prototype is constructed and photos are presented in Figure 3.13.



(a)



(c)



(b)

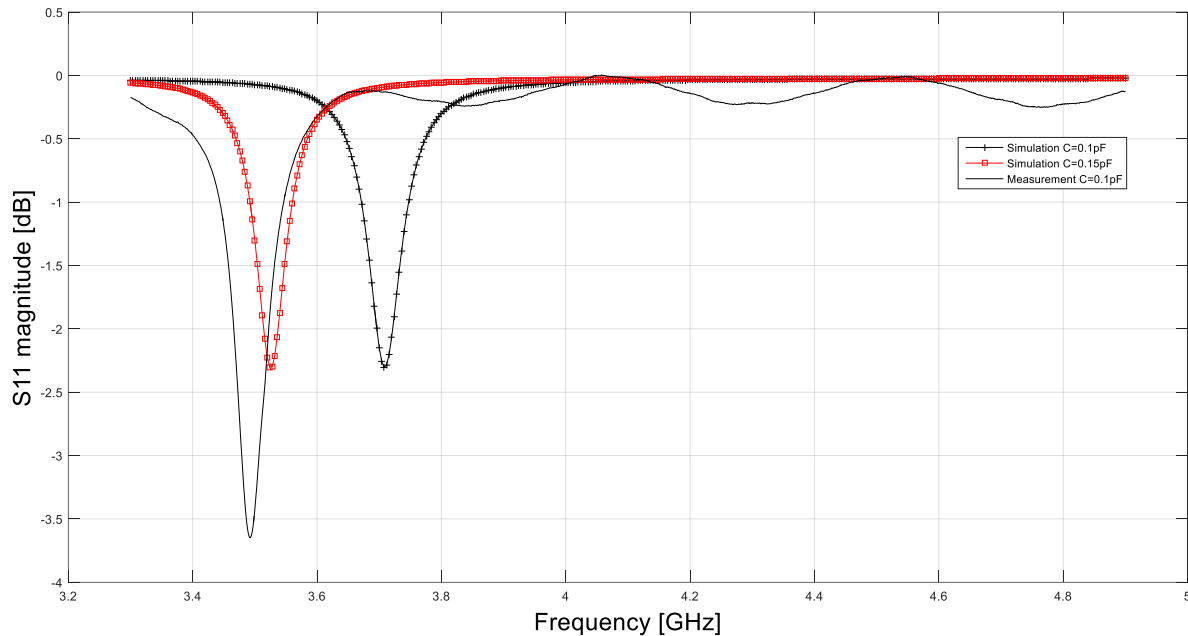


(d)

**Figure 3.13 : The prototype of the two unit cells inserted in the WR229 waveguide: (a) Back view (b) Top view (c) Place to insert two unit cells (d) Two unit cells attached in the waveguide and locked with screws.**

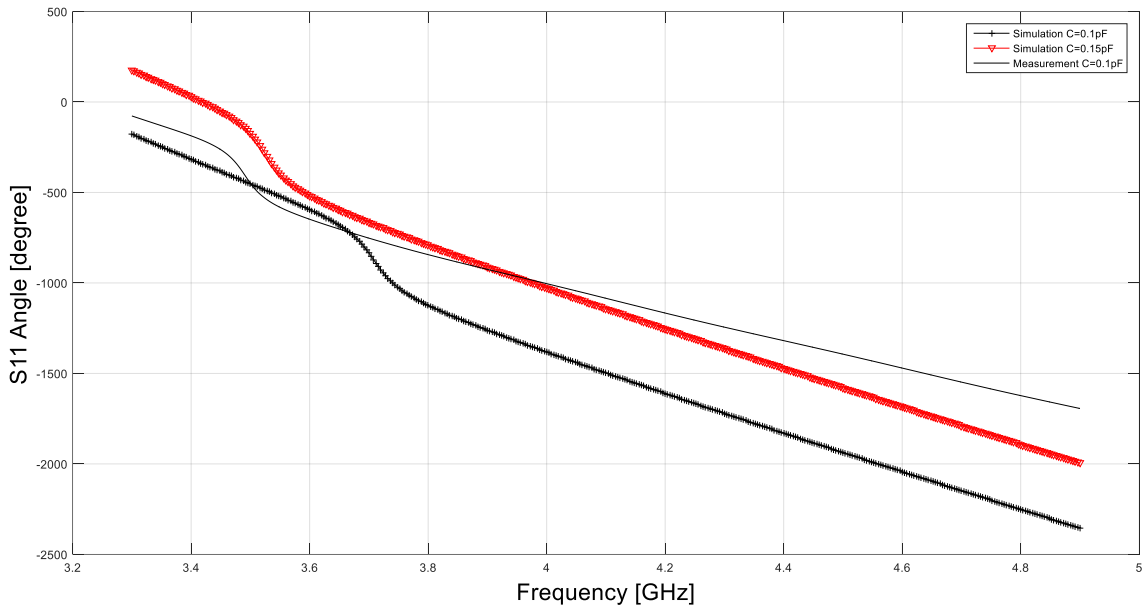
### 3.2.3.2. Measurement data vs. simulation results

In the simulations and measurements, we focus in the  $3.22\text{ GHz}\sim 4.9\text{ GHz}$  frequency band because the waveguide for the unit cell test operates in this frequency band. Simulation and measurement results are now compared in same graph as shown in Figure 3.14 and 3.15. The resonance happens at  $3.708\text{ GHz}$  in the simulation but only at  $3.492\text{ GHz}$  in the measurement for  $C = 0.1\text{ pF}$ . This frequency shift may be the effect from the capacitor tolerance. In the datasheet of the SMD capacitor, for  $C = 0.1\text{ pF}$ , it indicates that the tolerance value is  $\pm 0.05\text{ pF}$ . So, the simulation model with the capacitor  $0.1\text{ pF}$  and  $0.15\text{ pF}$  will be compared to the measurement. The capacitor value increase leads to the reduction of the resonant frequency as presented in Figure 3.14. The resonance gets closer to the measurement one with a level difference. For the comparison of phase as presented in Figure 3.15, the measurement results almost fit to the case of  $C = 0.15\text{ pF}$  as well.



**Figure 3.14 :**  $S_{11}$  magnitude in dB for model simulation vs. measurement data

After comparison, it comes to the conclusion that the capacitor real value in the prototype board seems to be  $0.15\text{ pF}$  so that the resonant frequency is at  $3.5\text{ GHz}$  as in the measurement results. There are still some differences in the magnitude and frequency due to tolerance in capacitor width, length and height as well as the real value of loss tangent and the conductivity of the dielectric material. The way the capacitor is simulated in the unit cell can however be considered as efficient regarding the measurement and simulation comparison on this case.



*Figure 3.15 :  $S_{11}$  phase for model simulation vs. measurement data*

### **3.3. Conclusion**

In this chapter, the MET is developed for the analysis and selection of metamaterial type in order to use it on the walls of the reverberation chamber. The surface impedance of several unit cell structures are observed through the Ansys-HFSS simulation to find the suitable one. Then a unit cell structure is selected and characterized through simulation and measurement. A good agreement is observed between the simulation and the measurement of the metamaterial unit cell prototype.



# Chapter 4: Sensitivity analysis and characterization of reverberation chamber prototype

In this section, the reverberation chamber with the metallic and the metamaterial walls will be designed and characterized. This chapter is divided into three parts. In the first part, the rectangular cavity with metallic walls is analyzed to choose the suitable material. Then the rectangular cavity with metamaterial walls is studied through parametric analysis to refine the cell's parameters. These studies are achieved with the Eigen-mode solver of Ansys-HFSS software. In the second part, the reverberation chamber with metamaterial walls is characterized by the full-wave Ansys-HFSS software. The antenna and the stirrer are selected to generate homogeneous electromagnetic field into the chamber. The antenna positions, the number of measurement points and stirrer positions are justified to get the standard deviation. The LUF value is extracted from the simulation data. In the third part, the RC with metallic and metamaterial walls are measured to extract the LUF. Results are compared to simulations.

## Content

---

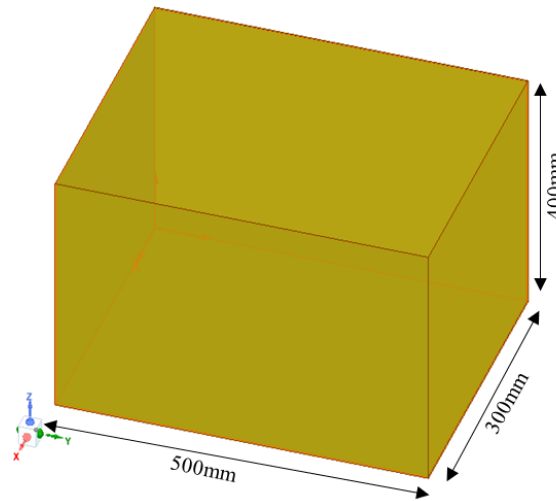
4.1.	Sensitivity analysis on the cavity .....	56
4.1.1.	Metallic walls selection .....	56
4.1.2.	Material and capacitor selection for the metamaterial walls .....	57
4.2.	Reverberation chamber prototype .....	61
4.2.1.	Stirrer design and position .....	62
4.2.2.	Working volume and field probe location in the reverberation chamber .....	65
4.2.3.	Antenna selection and position .....	67
4.2.4.	Configuration set up .....	72
4.3.	Measurement and qualification of the chamber .....	76
4.3.1.	Measurement configuration and data extraction .....	76
4.3.2.	Chamber prototype with metallic and with metamaterial walls .....	79
4.3.3.	LUF results, comparison and discussion .....	80
4.4.	Conclusion .....	82

## 4.1. Sensitivity analysis on the cavity

In this section, several parametric analyses are done to choose properly the materials (dielectric, metal) and the capacitor used in the unit cell. The cavity is first qualified “empty” which means without the antenna, the stirrer or the probe through HFSS simulations.

### 4.1.1. Metallic walls selection

The internal dimension of the reverberation chamber is defined, as stated before as (300 mm, 500 mm, 400 mm) along x, y and z axis as shown in Figure 4.1.



*Figure 4.1 : The simulation model of small cavity box*

Initially, only the metallic walls reverberation chamber is analyzed to choose the walls material. The resonant frequencies with aluminum and copper walls are computed with HFSS. In both cases, the thickness of the metallic walls is set to 1mm which is much higher than the skin depth.

For the first resonant frequency at 479 MHz, the skin depth is 5.14  $\mu\text{m}$  for the aluminum walls. So, thickness is ruled by the strength of the aluminum sheet not by the RF properties. To have strong walls and be confident with skin effect, the thickness for the prototype walls is 3mm.

The quality factor depends on the frequency and the metallic conductivity. The Q-factor of the chamber defines the ability of the chamber to store the excited energy in the chamber for a period of time  $\tau$ . This value gives the information on how much power needs to be inserted to get the specific field strength for EMC test (normally for immunity test). The formula of the Q-factor, which is the modified form of (2.2), is function of the metallic conductivity  $\sigma$  as shown in equation (4.1).

$$Q(f) = \frac{8Vf^{3/2}\sqrt{\pi\sigma\mu_0}}{cS\left(\frac{1}{a} + \frac{1}{b} + \frac{1}{d}\right)} \quad (4.1)$$

where  $V$  is the total volume of the chamber ( $V = a \times b \times d$ ),  $S$  is the total internal surface of the metallic walls ( $S = 2ab + 2bd + 2da$ ),  $c$  is the speed of light in free space,  $f$  is the frequency,  $\sigma$  is the metallic conductivity,  $\mu_0$  is the free space permeability and  $(a, b, d)$  are the three dimensions of the rectangular cavity.

The HFSS model of reverberation chamber is simulated with the aluminum and copper walls. The aluminum conductivity is  $\sigma_{aluminum} = 20 \times 10^6 S/m$ . The copper material has the conductivity  $\sigma_{copper} = 57 \times 10^6 S/m$ .

Table 4.1 shows the comparison of the Q factor for aluminum and copper walls. The criteria in this simulation is a maximum  $\Delta f = 1\%$ .

**Table 4.1 : The first 10 resonant frequencies and Q-factor for chamber with aluminum versus copper walls**

Mode	PEC	Aluminum Box		Copper Box	
	f [MHz]	f [MHz]	Q-factor	f [MHz]	Q-factor
1	479.902	479.902	9719	479.912	16408
2	582.691	582.692	11697	582.724	19748
3	624.567	624.567	12470	624.622	21053
4	692.791	692.792	13691	692.888	23116
5	692.791	692.792	13691	692.924	23117
6	707.059	707.059	13940	707.160	23537
7	780.484	780.485	15195	780.576	25655
8	807.215	807.216	15640	807.219	26403
9	865.786	865.787	16593	865.796	28013
10	865.786	865.787	16593	865.801	28014

The results indicate that the Q factor with copper walls is higher than with aluminum walls, even if, both cases give high values of Q-factor. These high values of Q-factors are related to the high conductivity of both metallic materials. The resonant frequencies in both cases are almost identical and very close to those calculated from the perfect electric conductivity cavity. As known from the theory, the LUF will therefore not be dependent on metal type but only on the chamber dimensions.

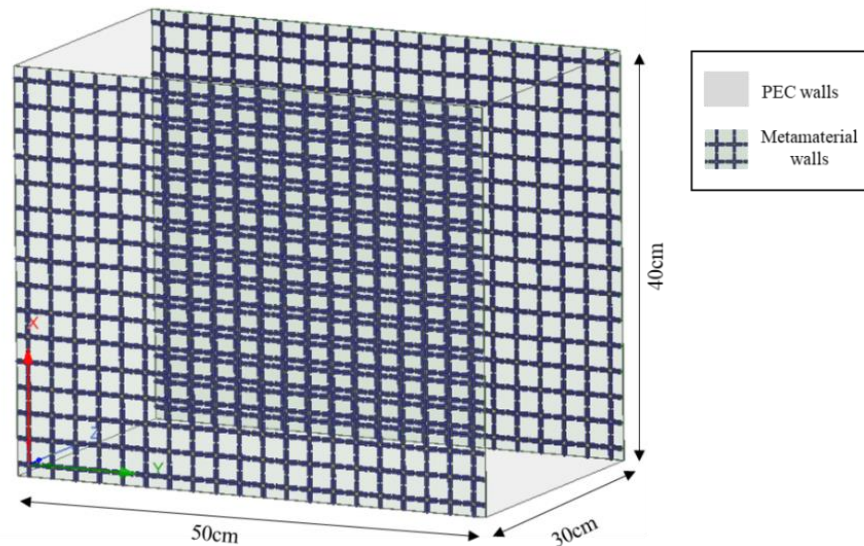
In conclusion, the reverberation chamber with aluminum walls is chosen because it allows high Q-factor for lower price than with copper walls, since the copper is 3 to 4 times more expensive than aluminum. Moreover, aluminum presents acceptable solidity strength and is easy to mill, punch, bend, cut, drill or join.

#### **4.1.2. Material and capacitor selection for the metamaterial walls**

The unit cell dimension and structure are defined in section 3.2.1. The metamaterial walls parameters of the reverberation chamber are now analyzed in this section. The effect of the

dielectric loss tangent and dielectric thickness is observed on the resonant frequencies and the Q-factor of the cavity. Then, the capacitor is selected to have the resonance below the LUF. This condition gives the negative surface impedance of metamaterial. The HFSS simulation model is shown in Figure 4.2. In this model, two metamaterial walls are inserted, all the other walls remain in PEC. The metallic lines that connect the capacitors are also defined as PEC sheets to save computation time and memory storage.

Two dielectric materials are selected to compare their effects on the LUF and Q-factor. Those dielectric are Roger RO4003 and RO4232 because these dielectric boards present different permittivity, loss tangent and multiple choice of thickness. Five simulations are performed so that only one parameter is changed between two of them. The analysis is performed on the dielectric relative permittivity, the dielectric thickness, the dielectric losses and the capacitor value of the unit cell. According to **Annex 6.5**, both walls with distance 30 cm are chosen to hang the metamaterial walls on them.



*Figure 4.2 : HFSS model of the rectangular cavity with two metamaterial walls*

#### **4.1.2.1. Dielectric relative permittivity effect**

In this section, performances are observed against dielectric permittivity. The chosen relative permittivity values are 3.2 in the first case and 3.55 in the second case, which correspond to Roger RO4232 and RO4003, respectively. For both cases, the thickness is 1.524mm, the loss tangent is 0.0021 and the capacitor is 39pF. The simulation results are shown in Table 4.2, for the maximum  $\Delta f = 1\%$  in Ansys-HFSS software.

**Table 4.2 : Comparison table for RO4232 and RO4003 substrates with relative permittivity 3.2 and 3.55, respectively.**

Mode	Permittivity = 3.2		Permittivity = 3.55	
	f [MHz]	Q-factor	f [MHz]	Q-factor
1	164.348	46450	164.588	41440
2	164.490	46085	165.084	41418
3	164.927	46110	165.428	41193
4	165.618	45211	165.510	41080
5	165.733	44985	166.389	39900
6	165.809	45768	167.048	40451
7	166.946	44830	167.931	40059
8	168.152	44240	169.094	39726
9	168.247	44601	169.122	38849
10	169.182	43719	171.649	34932

According to Table 4.2, the material with lower permittivity gives slightly lower resonant frequencies and higher Q-factor than material with high permittivity. In this part, the cavity walls are PEC, which explain the high Q-factor observed compared to Table 4.1. However, due to the availability of the PCB board Roger RO4003 in the market, the Roger RO4003 is preferred as PCB board since performances are comparable to the RO4232.

#### **4.1.2.2. Dielectric thickness effect**

The effects of dielectric material thickness on the resonant frequencies and Q factor are observed in this section. The dielectric material for both cases is RO4003 with a permittivity of 3.55 and loss tangent of 0.0021. The capacitor value is still 39 pF. The thickness of the dielectric material is 0.762 mm in the first simulation and 1.524 mm in the second simulation. The simulation criteria is set as maximum  $\Delta f = 1\%$ . Table 4.3 shows both simulation results.

**Table 4.3 : Comparison of resonant modes when changing thickness of dielectric material**

Mode	Thickness = 0.762mm		Thickness = 1.524mm	
	f [MHz]	Q-factor	f (GHz)	Q-factor
1	199.264	26357	164.588	41440
2	200.281	26020	165.084	41418
3	200.351	26125	165.428	41193
4	202.319	25423	165.51	41080
5	203.397	25276	166.389	39900
6	206.085	24517	167.048	40451
7	207.848	24804	167.931	40059
8	209.913	23923	169.094	39726
9	212.85	24026	169.122	38849

10	214.31	23032	171.649	34932
----	--------	-------	---------	-------

According to Table 4.3, the resonances move to lower frequencies for larger dielectric thickness. It should be resulting from the fact that both impedance walls get closer while the dielectric thickness increases and according to **Annex 6.5**, more resonant modes at low frequencies are created. The Q-factor is high at low frequency and decreases at high frequencies since losses are more important in the dielectric at high frequencies [100, 101].

Since, large dielectric thickness presents better performances, the dielectric material with 1.524 mm thickness is chosen for the metamaterial walls.

#### 4.1.2.3. Dielectric losses effect

In this part, the effects of the dielectric losses on the resonant modes and Q-factor of the metamaterial walls RC are studied. The first simulation model contains the PCB board RO4003C with 3.55 relative permittivity and 0.0021 loss tangent and 1.524 mm thickness. The second simulation model contains the same PCB board but with the modified loss tangent to 0.0042 to analyze its effect. Table 4.4 shows the comparison between both simulations with the simulation criteria as maximum  $\Delta f = 1\%$ .

*Table 4.4 : Two cases with different dielectric loss tangent*

Mode	Loss tangent = 0.0021		Loss tangent = 0.0042	
	f [MHz]	Q-factor	f [MHz]	Q-factor
1	164.588	41440	164.556	20926
2	165.084	41418	165.352	20795
3	165.428	41193	165.375	20616
4	165.51	41080	166.549	20759
5	166.389	39900	168.552	20441
6	167.048	40451	173.185	19377
7	167.931	40059	174.067	18973
8	169.094	39726	177.443	18045
9	169.122	38849	178.013	18011
10	171.649	34932	182.817	18010

The results indicate that the dielectric loss tangent has major effect on the Q-factor of the chamber. When the loss tangent is increased, the Q-factor is drastically decreased (factor 2). Furthermore, the loss tangent of the material has also an effect on the resonant frequencies in particular at high frequencies. It tends to increase the resonant frequency values.

In conclusion, the dielectric material with lower loss tangent is required to get high value of Q-factor. So, the PCB with loss tangent as 0.0021 is chosen as PCB for the design.

#### 4.1.2.4. Capacitor value effect

In this sub-section, the effect of the capacitor value used for the unit cell is evaluated through two simulation cases. The capacitor values are 39pF in the first case and 100pF in the second case. Table 4.5 shows the simulation results for the first 10 resonant modes.

The results from Table 4.5 indicate that the resonant frequencies of the chamber are shifted to lower value when the capacitor value of the unit cell is increased. The Q-factor is also higher for the case with high capacitor.

In conclusion, high value of capacitor in the unit cell could give a lower value of the resonant frequencies of the chamber. Due to the antenna dimension constraint, the chamber band is restricted to 1.5 GHz – 20 GHz, therefore it was decided to use the unit cell with capacitor 39 pF. However, in bigger reverberation chamber, such capacitor can be selected to reduce the LUF.

*Table 4.5 : The first 10 resonant frequencies for two capacitor values*

Mode	C=39pF		C=100pF	
	f [MHz]	Q-factor	f [MHz]	Q-factor
1	164.588	41440	103.181	107237
2	165.084	41418	103.678	104774
3	165.428	41193	103.784	105673
4	165.510	41080	104.512	103134
5	166.389	39900	105.092	102780
6	167.048	40451	105.893	101347
7	167.931	40059	106.209	98196
8	169.094	39726	107.855	97720
9	169.122	38849	109.217	97745
10	171.649	34932	109.265	99445

Finally, the unit cell is achieved on RO4003 substrate with 3.55 relative permittivity, 0.0021 loss tangent and thickness of 1.524 mm. The capacitors are 39 pF.


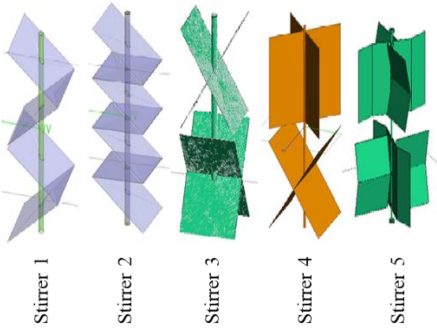
## 4.2. Reverberation chamber prototype

This section focuses on the complete structure of the reverberation chamber. A specific stirrer is designed and placed in the chamber. The antenna properties are underlined and the antenna position is justified. Then the chamber is qualified with and without the metamaterial walls against field uniformity properties. The two reverberation chambers (with aluminum walls and with metamaterial walls) are compared to attest from the LUF reduction.

### 4.2.1. Stirrer design and position

Stirrer is one important component in the reverberation chamber. It is used to achieve the electric field uniformity [87]. The shape, size and weight of the stirrer need to be carefully considered in the design. The design criteria of the mechanical stirrer in [92] indicates some guidelines for its construction. This guideline indicates that the stirrer shape must be asymmetric around the rotational axis in order to give different boundary conditions in the chamber for one cycle of rotation. Its weight must be balanced on the center of the rotating axis for the stability in long-term measurement operation. Its top and side view footprints must be as large as possible. The stirrer's shape should be simple to ease its construction. In order to select the suitable stirrer, some stirrer's structures are studied and compared according to the state of the art. Table 4.6 summarizes this comparison.

*Table 4.6 : Comparison of some stirrer shapes*

Ref	Shape of stirrer	Description	Selection	Reasons
[88]		The left side stirrer is the metallic plate, the middle side stirrer is the irregular Z-folded stirrer, the right side stirrer is the Z-folded with shift angle between each wings.	The irregular Z-folded stirrer (the middle)	The irregular Z-folded stirrer gives low value of standard deviation compared to other two.
[89]		There are 5 different shapes of the stirrer as presented in the figure and named from stirrer 1 to stirrer 5.	The stirrer 5 is selected.	Stirrer 5 gives LUF at 100 MHz. Stirrer 3 gives LUF at 200 MHz. Stirrer 1 gives LUF at 300 MHz.



[90]	<p>Stirrer Type I      Stirrer Type II      Stirrer Type III</p>	<p>Wings of stirrer type I rotate in the same direction. Wings of stirrer type II rotate in opposite direction with previous one. Stirrer type III moves in the line.</p>	<p>The stirrer Type I (the Z-shaped stirrer) is selected.</p>	<p>Stirrer type I has a simple form and gives the lowest value of the standard deviation amongst the three.</p>
[91]		<p>The rotational axis of both stirrer is the horizontal axis (u axis).</p>	<p>The stirrer at the left side is selected.</p>	<p>Both stirrers give almost same field uniformity but the Z-folded stirrer has simpler form.</p>

According to the table, the Z-folded stirrer seems to be the best choice because its structure is simple and its performances insure field uniformity compared to the other structures.

In [86] and [93], the stirrer rotational axis location has no significant effect on the chamber performance. Hence, the stirrer location is justified against the maximization of the chamber's working volume. In both studies, only one stirrer is used in the chamber.

In this thesis, the Z-folded stirrer is therefore selected due to its simple form and since it is generally used in conventional chamber. Only one stirrer will be used and placed in the chamber to maximize the working volume. According to [78], the stirrer should follow a few design rules as follow:

- The stirrer has one dimension that is at least one-quarter wavelength at the LUF
- The stirrer should have one dimension at least three-quarters of the smallest chamber dimension
- The stirrer volume should represent approximately 8% of the whole volume of RC
- The stirrer should be shaped asymmetrically to avoid the repetitive field pattern in the RC

The stirrer design for the small chamber in this thesis according to the above criteria is presented in **Annex 6.3**.

The proposed stirrer is designed as in Figure 4.3. The material for the stirrer wings and rod is the brass with conductivity  $15.9 \times 10^6 S/m$ . Its conductivity is comparable to aluminum ( $20 \times 10^6 S/m$ ) and brass is harder and stronger than aluminum in term of the mechanical properties. The thickness of the stirrer wings is 1 mm while the rod's diameter is 8 mm. See **Annex 6.3** for more detail on stirrer design. The location of the stirrer is shown in Figure 4.4 to have a maximum

working volume and the rotating axis is set on the aluminum walls. By using the location of the stirrer's rotational axis as in the Figure 4.4, the minimum distance from the stirrer wings to the nearest wall is  $10.2\text{ mm}$  which is reasonable for a safe margin.

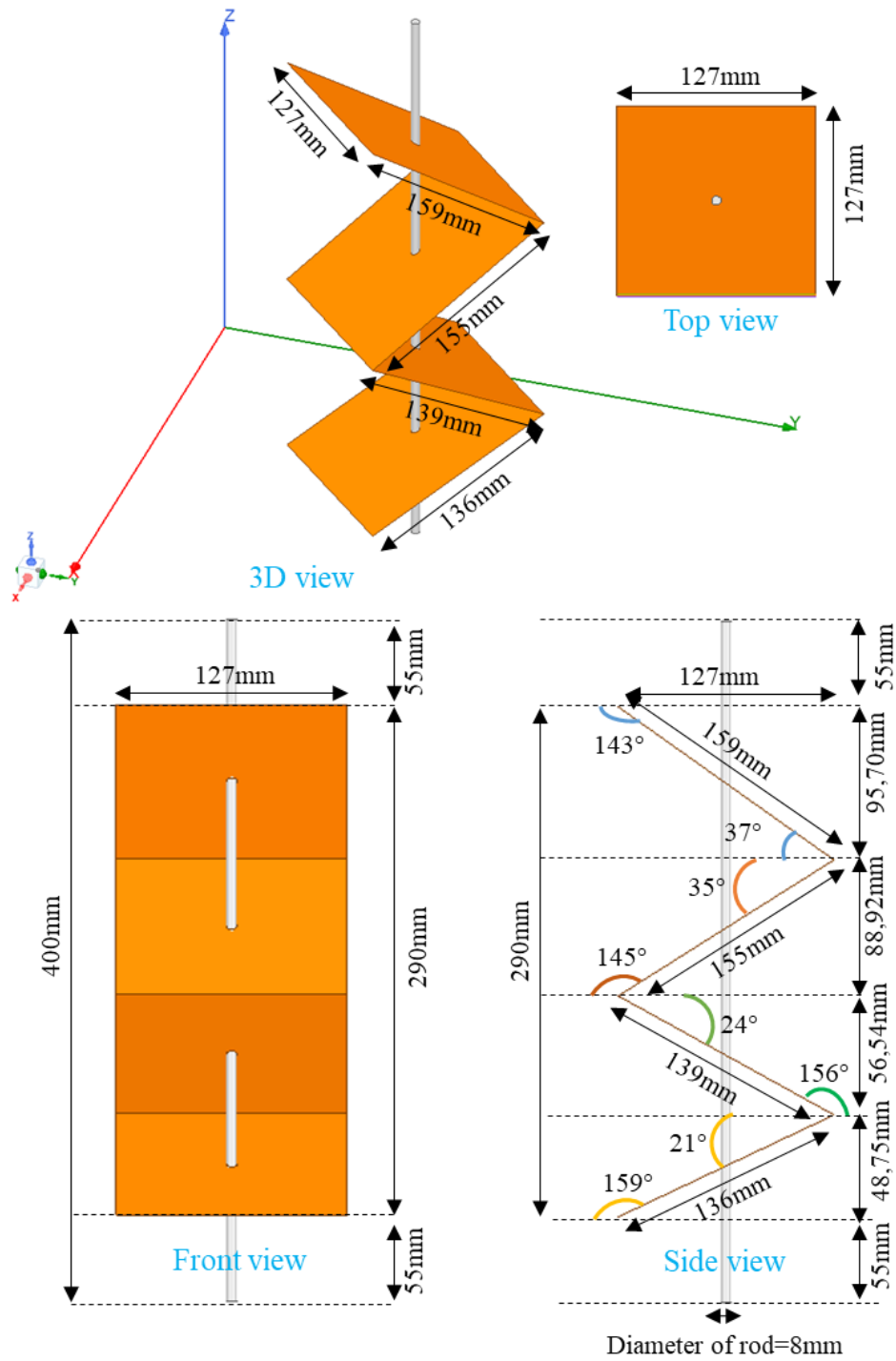


Figure 4.3 : Z-folded stirrer design

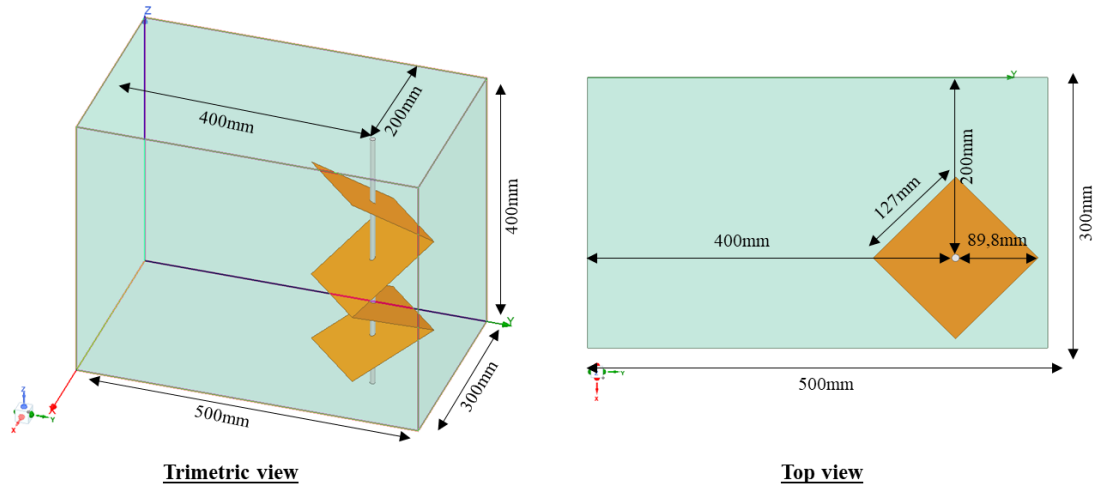


Figure 4.4 : Stirrer location in the reverberation chamber

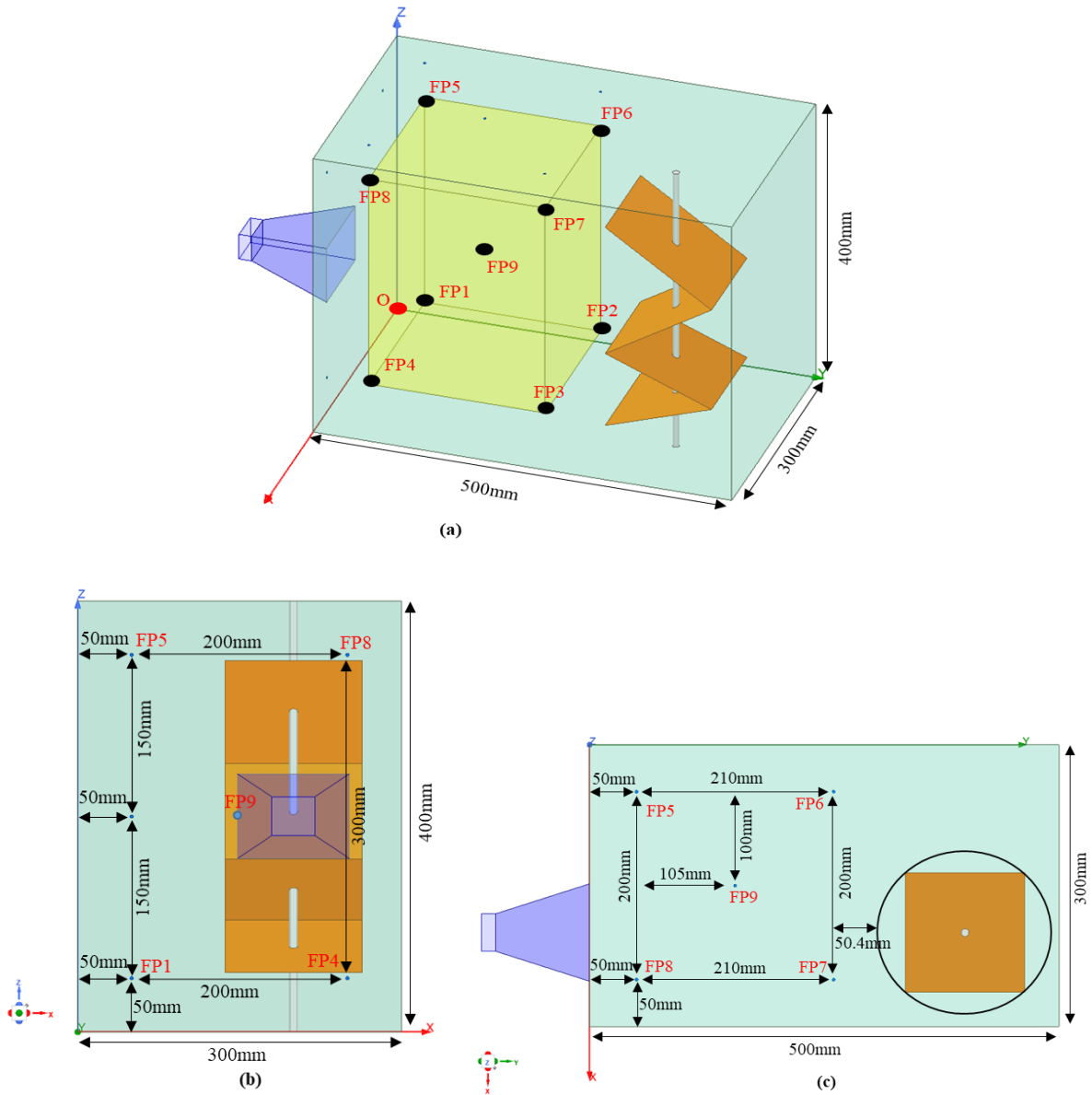
#### 4.2.2. Working volume and field probe location in the reverberation chamber

To qualify the chamber, the electric field needs to be measured at different locations within the working volume for several stirrer positions. Normally, 9 positions of the field probe are recommended by the IEC standard due to the time constraint in the measurement. To attest to the field uniformity, the number of measurement points is studied in simulation.

Along the x-axis and z-axis, the working volume is located at  $\frac{\lambda}{4} = 50 \text{ mm}$  (at the LUF as 1.533 GHz) from both walls (See the detailed analysis in **Annex 6.4**). Along the y-axis, it is located at 50 mm from the  $y = 0$  wall and at 50 mm from the stirrer. The working volume of the chamber is consequently  $W_{wv} \times L_{wv} \times H_{wv} = 200 \text{ mm} \times 210 \text{ mm} \times 300 \text{ mm}$  along  $x, y, z$  axis. Figure 4.5 shows the WV location and as example 9 possible locations of field probe in the WV.

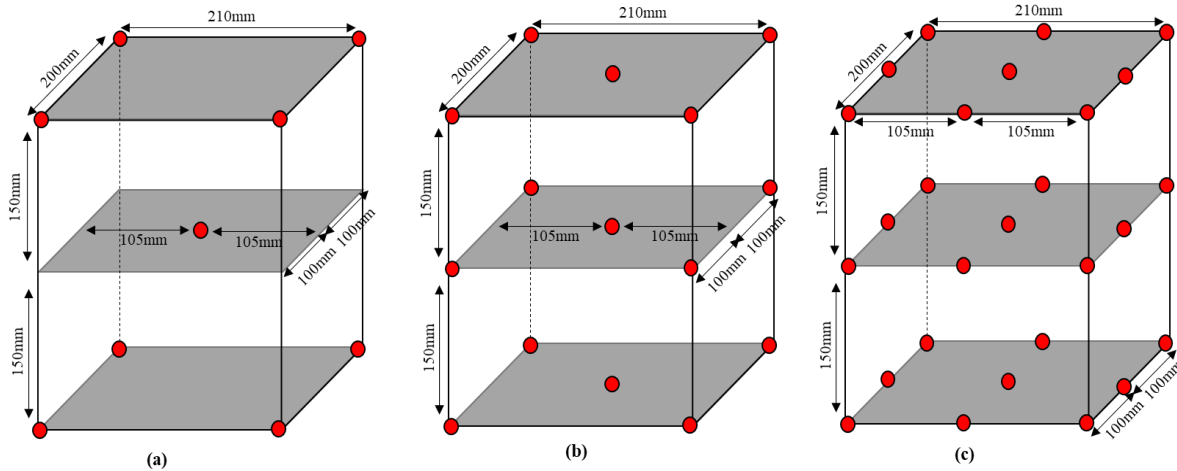
Amongst these 9 locations, 8 locations are at the 8 corners of the WV and one is located in the center of the working volume. By reference to the coordinate (0, 0, 0) of the origin O, the coordinate of each location of field probe FP1, FP2... FP9 are set as FP1 (5cm, 5cm, 5cm); FP2 (5cm, 26cm, 5cm); FP3 (25cm, 26cm, 5cm); FP4 (25cm, 5cm, 5cm); FP5 (5cm, 5cm, 35cm); FP6 (5cm, 26cm, 35cm); FP7 (25cm, 26cm, 35cm); FP8 (25cm, 5cm, 35cm); FP9 (15cm, 15.5cm, 20cm).

Within the working volume of the chamber, the locations of the field probe for the cases with 9, 15 and 27 probe locations lie on 3 horizontal planes as shown in Figure 4.6.



**Figure 4.5 :** The locations of field probe: (a) 3D view with the origin *O* set in red dot and the positions of field probe *FP1* to *FP9* are on black dot (b) Side view from the back of horn antenna (c) Top view

These positions will be used in a parametric analysis to choose the number of stirrer angular positions and probe positions in part 4.2.4.



**Figure 4.6 :** The location of field probe in the working volume identified by red dot (a) Case 9 field probe locations (b) Case 15 field probe locations (c) Case 27 field probe locations.

### 4.2.3. Antenna selection and position

#### 4.2.3.1. Antenna selection

To generate field in the cavity, the suitable antenna needs to be selected. Table 4.7 shows the antenna specification used in the calibration of some reverberation chambers following specific standard. The information of the calibration frequency band is also included. Table 4.7 shows that a wideband antenna which can cover all the calibration frequency band and with starting frequency below the LUF is required.

**Table 4.7 :** Antennas specification and frequency band for some reverberation chamber calibration

Ref.	Transmitter antenna		Receiver antenna		Chamber Size (W x L x H) $m^3$	Measurement LUF
	Type	Freq. band	Type	Freq. band		
[51]	LPDA	300MHz-1.3GHz	LPDA	300MHz-1.3GHz	$4.72 \times 7.52 \times 5.60$	370MHz
[44]	Not specified	153MHz-1GHz	Not specified	153MHz-1GHz	Not specified	530MHz
[63]	LPDA	50MHz-1GHz	Field probe and Biconilog antenna	50MHz-1GHz	$8.94 \times 6.00 \times 3.92$	66.76MHz
[102]	LPDA	80MHz-1GHz	E-field probe (AR FL7218)	80MHz-1GHz	$9.30 \times 6.10 \times 4.90$	82MHz

It should be noticed that the most common used excitation antennas for reverberation chamber are the Log-Periodic Dipole Array antennas (LPDA). An electric field probe is normally used at

the receiver part during the first calibration of the new constructed chamber following the IEC 61000-4-21 standard

In Table 4.8, the size and frequency band of some LDPA antennas are reported.

For small reverberation chamber, the antenna selection is a challenge since the frequency band and the size of the antenna must be compatible to the chamber's size. For the classical LPDA antenna, the size is too big for our the chamber size of  $W \times L \times H = 30\text{cm} \times 50\text{cm} \times 40\text{cm}$ .

**Table 4.8 : Some available LPDA antennas with specification of frequency range and size**

LPDA Antenna	Frequency range	Size
Com-Power ALC-100	300MHz-1000MHz	64.8cm x 54.6cm x 13cm
Com-Power AC-220	25MHz-2GHz	96cm x 127cm x 63cm
ETS-Lindgren 3148	200MHz-2GHz	6.4cm x 85.6cm x 73.7cm
SAS-510-2 Directional Log Periodic Antenna	290MHz-2GHz	57.4cm x 51.1cm
LPA2G-HP High Power Log Periodic Antenna	190MHz-2GHz	57.4cm x 51cm
ETS-Lindgren 3147 Log Periodic Antenna	200MHz-5GHz	7.6cm x 88cm x 97cm

Horn antennas can be an alternative to LDPA antennas since they are also directional and have high gain. Especially, horn antennas are smaller than LPDA antennas within the same frequency band of operation. Table 4.9 shows commercial horn antenna's size and frequency range specification.

The horn antenna can be fixed on the cavity wall of size  $300\text{ mm} \times 400\text{ mm}$  as presented in Figure 4.4. The biggest size of the horn aperture must therefore be compared to this surface.

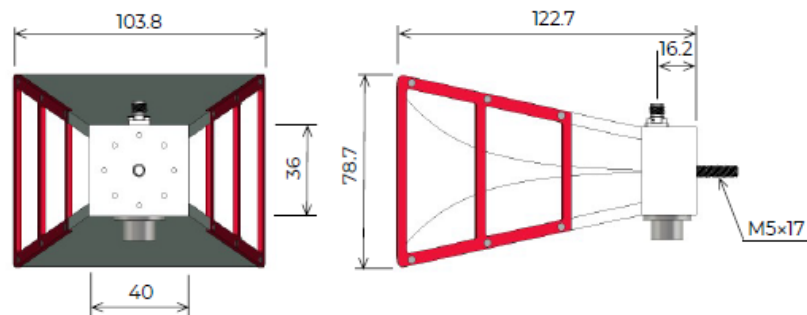
**Table 4.9 : Frequency bands and sizes of horn antennas**

Horn Antenna	Frequency range	Size (W x H x L)	Justification
H-1498	2GHz - 18GHz	9.9cm x 8.12cm x 12.44cm	Minimum frequency at 2GHz so higher than the expected LUF.
PowerLOG 10800	1GHz - 8GHz	23.5cm x 17.5cm x 25.2cm	Aperture maximum size is 23.5cm which is big compared to chamber size. So, it is not selected.
PowerLOG 70180	700MHz - 18GHz	23.5cm x 17.5cm x 25.2cm	Aperture maximum size is 23.5cm which is big compared to chamber size. So, it is not selected.
BBHA 9120 A	1GHz - 5GHz	24.5cm x 14.2cm x 22cm	Aperture maximum size is 24.5cm which is big compared to chamber size. So, it is not selected.

BBHA 9120 B	1.25GHz - 10GHz	18.2cm x 12.4cm x 27.2cm	Aperture maximum size is 18.2cm which is big compared chamber size. So, it is not selected.
BBHA 9120 C	2GHz - 18GHz	9.8cm x 6.8cm x 14cm	The minimum frequency at 2GHz so higher than the expected LUF.
BBHA 9120 D	1GHz - 18GHz	25cm x 14.2cm x 19.5cm	Aperture maximum size is 25cm which is big compared to chamber size. So, it is not selected.
SAS-571	700MHz - 18GHz	24.4cm x 14.2cm x 20.3cm	Aperture maximum size is 24.4cm which is big compared to chamber size. So, it is not selected.
TBMA4	1GHz - 18GHz	24.1cm x 15.3cm x 21.4cm	Aperture maximum size is 24.1cm which is big compared to chamber size. So, it is not selected.
DRH20E	1.6GHz - 20GHz	10.38cm x 7.87cm x 12.27cm	The lowest frequency and the size of the antenna are acceptable.

The advantage of the horn antenna is that only the aperture may be considered if the horn antenna is placed on the wall side while for the LDPA antenna, it is mandatory to put it in the chamber. It should be reminded that the size of the chamber is  $30\text{cm} \times 40\text{cm} \times 50\text{cm}$  and its estimated LUF is  $1.533\text{ GHz}$  for metallic walls chamber in empty case. Therefore, this antenna will satisfy the criteria to have the LUF in its band, since the required minimum operating frequency of the antenna must be lower than the expected LUF of the chamber.

The best option amongst the antennas in the table is the horn antenna model DRH20E with size  $10.38\text{cm} \times 7.87\text{cm} \times 12.27\text{cm}$  and frequency range from 1.6 GHz to 20 GHz. This is the most suitable choice for our selected chamber's size. The horn antenna DRH20E is shown in Figure 4.7. It is selected for the measurements.

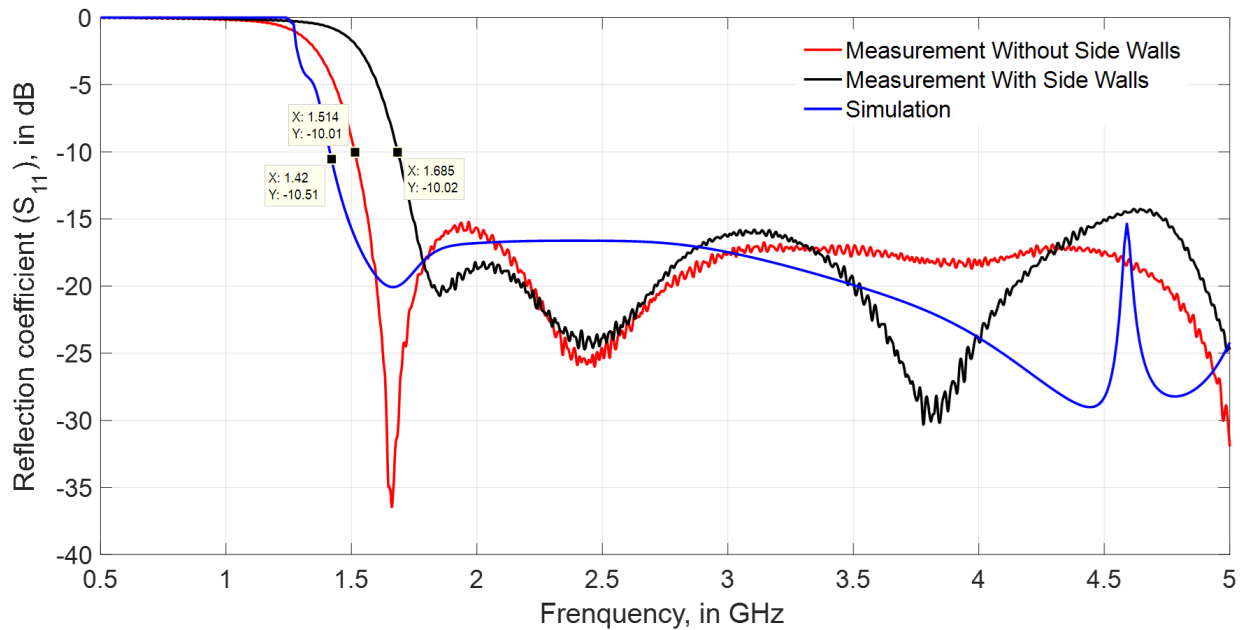


**Figure 4.7 : DRH20E double ridged horn antenna (dimension in mm)**

Due to the small size of chamber, the excitation antenna is placed outside of the chamber and fixed on chamber wall. The purpose is to have the largest working volume possible. Since the antenna walls are opened, tests must be done when filling them to verify that the performances at

lowest frequencies are still acceptable. So, the antenna is measured with and without the metallic walls on its sides.

The structure of the proposed horn antenna has been modeled and simulated with Ansys-HFSS. The purpose is to get a model with almost similar characteristic to the real antenna in order to estimate its best position to generate the field in the reverberation chamber model. The simulation and measurement results in term of reflection coefficient ( $S_{11}$ ) are presented in the Figure 4.8. Initially, the antenna is qualified against its physical parameters but the results were very different from the measured one since it was difficult to represent well its feeding access.



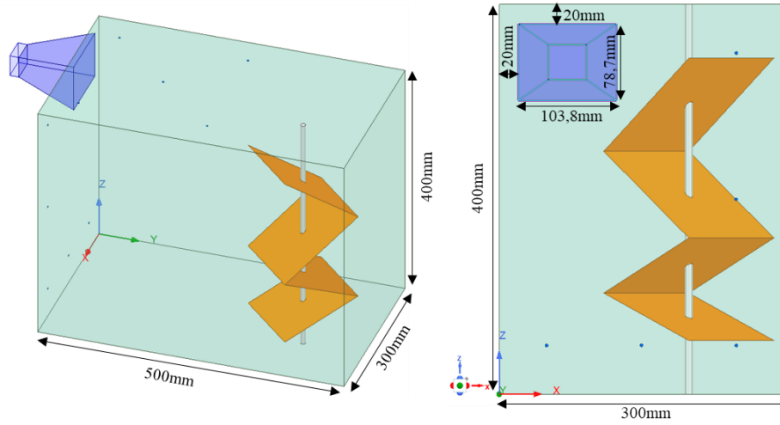
**Figure 4.8 :** Reflection coefficient of the horn antenna model vs. the real horn antenna with and without covering side walls by metallic sheets.

If we consider the band at  $|S_{11}| = -10 \text{ dB}$ , the antenna model can operate from 1.42 GHz up to 5 GHz while the real antenna can operate from 1.514 GHz and 1.685 GHz up to 5 GHz respectively in the case without and with metallic side walls. The differences between the model and antenna results is acceptable. Covering the open wall is also acceptable even if it is reducing the band.

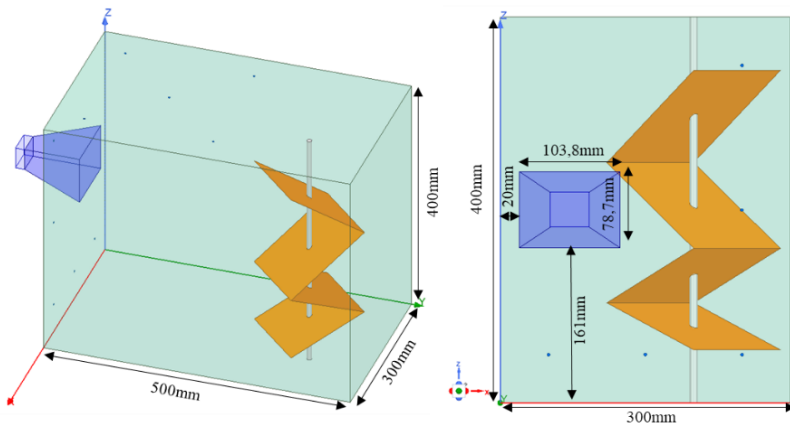
#### **4.2.3.2. Position of the excitation antenna**

To define the antenna position, three cases are considered and compared against the performance on the field uniformity. The antenna is placed at the top-left, the middle-left and the middle-right of the wall opposite to the stirrer for the case 1, case 2 and case 3, respectively. The detailed locations of the antenna on each case are shown in Figure 4.9 to 4.11.

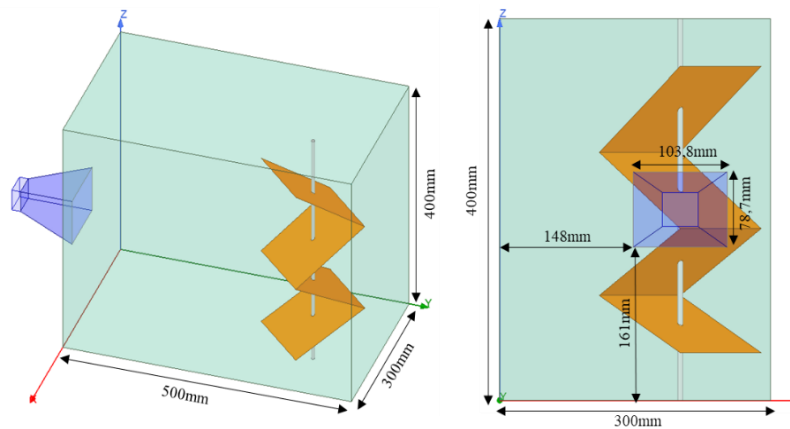




**Figure 4.9 : Position of case 1**



**Figure 4.10 : Position of case 2**



**Figure 4.11 : Position of case 3**

Simulations are now achieved with Ansys-HFSS to select according to the standard deviation one of these three excitation positions. The electric field data from various points in the working

volume are exported in a MATLAB code following the IEC 61000-4-21 standard. The electric field uniformity in the working volume is now observed with different number of field probe positions such as 9, 15 and 27 positions as shown Figure 4.6 and different number of stirrer angles since the number of field probe locations and number of stirrer angles must be defined for measurements. It is the purpose of next part.

#### **4.2.4. Configuration set up**

Simulation are performed with the accuracy  $\Delta S = 0.02$  for seven frequency points selected as 1.5 GHz, 1.683 GHz, 1.888 GHz, 2.118 GHz, 2.376 GHz, 2.665 GHz and 2.99 GHz. Due to time constraints and calculation resources, the simulation can only be done on these seven frequency points and with frequencies lower than 3 GHz.

In the results, the numbers in red color present a value higher than the threshold limit of 3dB according to the IEC 61000-4-21, since it indicates that from the frequency of 400 MHz, the standard deviation limit for the field uniformity is 3 dB. The ones in green are close to the limit and may be due to numerical error. They can be considered as acceptable. Next sub-sections present the method to get the set up configuration for measurements.

##### **4.2.4.1. Selection of number of stirrer angles**

In this section, the required number of stirrer angle is observed. The full wave simulation is done for position of the excitation antenna as in case 1 (as shown in Figure 4.8), for 12, 18 and 36 stirrer angles, and for 27 probe locations. The measurement points are set as 27 locations in the working volume as presented in Figure 4.5 (c). Table 4.10 shows the results of the standard deviation for metallic walls reverberation chamber. Since data from 27 probe locations are recorded, it ensures that there are enough data points for statistical estimation of the field uniformity. So, in this section, only the stirrer angles are under consideration.

According to Table 4.10, with the increase of the number of stirrer angle, the standard deviation of the electric field is more accurate. This is due to the fact that some boundary conditions are not presented with limited stirrer angles. Amongst the 3 cases, the case with 36 stirrer angles gives the accurate estimation of the field uniformity since results are comparable to the simulations and stable when compared to lower number of stirrer positions.

Since large number of stirrer angles is not difficult to achieved in the measurement, 36 stirrer angles will be used as measurement parameter. From Table 4.10, the LUF of the chamber is found to be above 2.118 GHz.

**Table 4.10 : Standard deviation (in dB) for antenna in position of case 1, metallic chamber, for 12, 18 and 36 stirrer angles, and for 27 locations of field probe**

12 stirrer step, 27FP							
Antenna Position	Frequency[GHz]						
Case1	1.5	1.683	1.888	2.118	2.376	2.665	2.99
SigmaX dB	2.616889539	3.359766989	3.202556214	3.965597138	3.079866356	2.871667809	3.010048861
SigmaY dB	0.018942261	0.998611841	0.632627546	0.065598487	2.095924198	0.189546285	0.847181375
SigmaZ dB	0.476210375	1.487239529	1.204066527	0.090856333	2.71856321	1.141546774	2.648793204
SigmaXYZ dB	1.617421004	2.50399495	2.194512719	2.442612689	2.781391621	2.198887005	3.00552213
18 stirrer step, 27FP							
Antenna Position	Frequency[GHz]						
Case1	1.5	1.683	1.888	2.118	2.376	2.665	2.99
SigmaX dB	4.212914713	3.570883769	2.766255237	3.776870457	2.909922525	2.267501511	2.757421867
SigmaY dB	1.799635435	2.57063272	1.161004028	1.967276962	2.050104247	0.790440359	0.846978167
SigmaZ dB	3.697023797	1.155289958	0.304878018	0.269537778	1.759720539	2.095219822	1.975737595
SigmaXYZ dB	4.701099475	3.033772124	2.319315551	2.995238405	2.273969074	1.930399551	3.217263474
36 stirrer step, 27FP							
Antenna Position	Frequency[GHz]						
Case1	1.5	1.683	1.888	2.118	2.376	2.665	2.99
SigmaX dB	3.897710831	3.052054228	3.296562822	3.165894832	2.714513148	2.684706415	2.607855642
SigmaY dB	0.309420053	1.794407013	2.097796187	1.458040862	1.9536536	2.27007906	0.872396367
SigmaZ dB	2.306655119	1.777720495	0.515808866	1.582623769	1.751115515	2.689342969	2.312708488
SigmaXYZ dB	3.703941653	2.541531049	3.666916589	2.538367223	2.171203843	2.682615924	2.866089061

#### 4.2.4.2. Selection of number of field probe locations

According to the statistical rules, numerous measurement points would give more accurate estimation of the results but it is time consuming since the probe location must be changed manually. The simulation in this section is used to decide on the appropriated number of field probe locations to be chosen. With only one available field probe and with time constraint in the measurement, a minimal number of field probe locations is preferred. Table 4.11 shows the results of the standard deviation for metallic walls reverberation chamber in the antenna position of case 1, with 36 stirrer angles and with 9, 15 and 27 field probe's locations as presented in Figure 4.6. Due to Table 4.11, the case with 15 locations of field probe is the best case for predicting the field uniformity since 9 positions lead to a little over estimation of the LUF. However, since the overestimated values are close to 3 dB and may also be due to numerical errors, 9 positions can therefore be acceptable. To save time, 9 points location is chosen as measurement parameters.

Hence, the measurement will be done with 36 stirrer positions and with 9 locations of field probe.

**Table 4.11 : Standard deviation (in dB) for antenna in position of case 1, metallic chamber, for 36 stirrer angles, and for 9, 15 and 27 locations of field probe**

36 stirrer step, 9FP							
Antenna Position	Frequency[GHz]						
Case1	1.5	1.683	1.888	2.118	2.376	2.665	2.99
SigmaX dB	3.223217928	3.21760294	2.902128509	2.494385704	3.149475074	2.513420721	2.87505521
SigmaY dB	1.192500017	2.604806027	2.444663964	2.025267683	3.265665295	2.373570788	3.057898494
SigmaZ dB	2.019307124	1.761942089	3.185995901	2.209536996	1.733813054	2.495834247	0.096160274
SigmaXYZ dB	4.020413406	2.614728311	4.229683093	2.470084669	2.790956411	2.429680094	2.406251551
36 stirrer step, 15FP							
Antenna Position	Frequency[GHz]						
Case1	1.5	1.683	1.888	2.118	2.376	2.665	2.99
SigmaX dB	3.864425609	2.755020093	3.022790386	3.191177545	2.868545736	2.960442464	2.796187496
SigmaY dB	0.248460604	1.782786218	2.267149532	1.463318102	2.10945427	2.380824813	0.789773191
SigmaZ dB	1.715372324	1.670531273	0.637470283	1.782233243	1.84572756	3.041633192	2.652512095
SigmaXYZ dB	3.846819856	2.334208946	3.395172162	2.568333408	2.297199446	2.820929662	2.984224372
36 stirrer step, 27FP							
Antenna Position	Frequency[GHz]						
Case1	1.5	1.683	1.888	2.118	2.376	2.665	2.99
SigmaX dB	3.897710831	3.052054228	3.296562822	3.165894832	2.714513148	2.684706415	2.607855642
SigmaY dB	0.309420053	1.794407013	2.097796187	1.458040862	1.9536536	2.27007906	0.872396367
SigmaZ dB	2.306655119	1.777720495	0.515808866	1.582623769	1.751115515	2.689342969	2.312708488
SigmaXYZ dB	3.703941653	2.541531049	3.666916589	2.538367223	2.171203843	2.682615924	2.866089061

#### 4.2.4.3. Selection of the antenna location on RC's wall

In this section, the position of the excitation antenna is observed. The full wave simulation is being done on each position of the excitation antenna as presented in Figure 4.9, 4.10 and 4.11 with 36 stirrer angles and 9 locations of field probe. Simulation criteria remain identical as in previous parts.

Table 4.12 shows the standard deviation results for these three cases of antenna position. Simulations are done only from 2.99 GHz down to 2.118 GHz since these 4 frequency points give enough data for LUF determination. According Table 4.12, the antenna position in case 1 gives the best field uniformity amongst the 3 cases. So, the antenna position of case 1 is used in the measurement.

**Table 4.12 : Standard deviation (in dB) for antenna in position of case 1, case 2 and case 3, metallic chamber, for 36 stirrer angles and for 9 positions of field probe**

36 stirrer step, 9FP				
Antenna Position	Frequency[GHz]			
Case1	2.118	2.376	2.665	2.99
SigmaX dB	2.494385704	3.149475074	2.513420721	2.87505521
SigmaY dB	2.025267683	3.265665295	2.373570788	3.057898494
SigmaZ dB	2.209536996	1.733813054	2.495834247	0.096160274
SigmaXYZ dB	2.470084669	2.790956411	2.429680094	2.406251551
36 stirrer step, 9FP				
Antenna Position	Frequency[GHz]			
Case2	2.118	2.376	2.665	2.99
SigmaX dB	2.49436076	2.805352788	2.640029468	2.393935378
SigmaY dB	1.572133367	4.029896416	0.390771556	2.085449209
SigmaZ dB	1.714976755	3.839758741	1.109173099	1.454238822
SigmaXYZ dB	2.188891322	3.498434507	2.2277046	2.078610985
36 stirrer step, 9FP				
Antenna Position	Frequency[GHz]			
Case3	2.118	2.376	2.665	2.99
SigmaX dB	2.881775666	2.656610987	3.14068997	1.487555297
SigmaY dB	1.424890208	3.548318787	0.643140911	2.529342018
SigmaZ dB	2.940485191	3.113857494	0.851359427	0.119905756
SigmaXYZ dB	2.796808313	3.115180869	2.280349565	1.762975703

Hence, for the measurement set up, the antenna position case 1, the 9 field probe locations and 36 stirrer angles are used as the measurement parameters. With such conditions, the LUF of the metallic RC is expected to be 2.376 GHz.

By using these set up parameters, the metamaterial walls reverberation chamber is also simulated. The field uniformity results are shown in Table 4.13. Due to limitation of computational resources, the simulation is done only up to 2.118 GHz. In this same conditions to the set up for metallic RC (antenna position case 1, 36 stirrer positions and 9 probe locations), the LUF of the metamaterial chamber is attended lower than 1.5 GHz even if the highest frequencies have not been tested due to computational resources.

**Table 4.13 : Standard deviation (in dB) for antenna in position of case 1, metamaterial chamber, for 36 stirrer angles and for 9 positions of field probe**

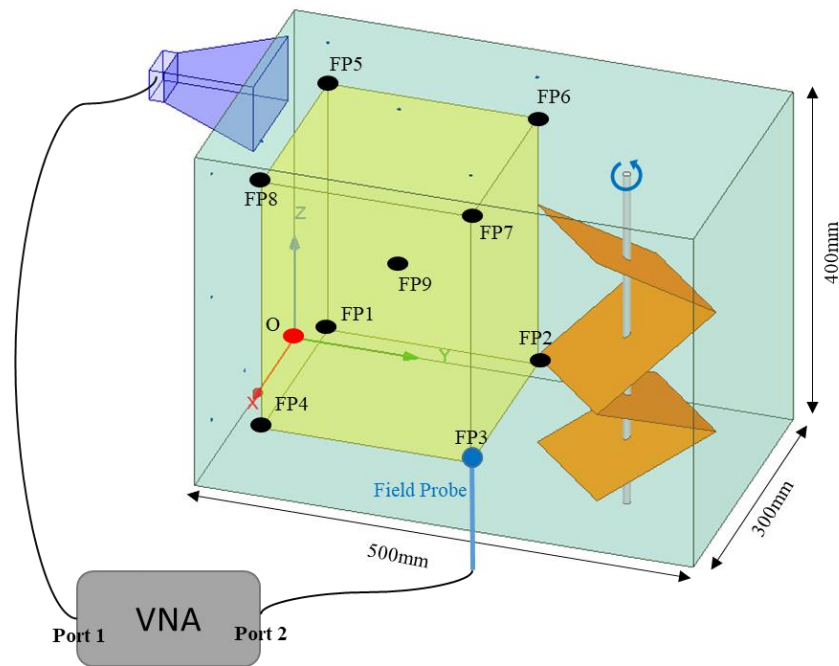
36 stirrer step, 9FP, Metamaterial walls				
Antenna Position	Frequency[GHz]			
Case1	1.5	1.683	1.888	2.118
SigmaX dB	1.431885346	1.682490752	1.984092756	2.855124549
SigmaY dB	0.727167319	1.823316547	0.257961959	2.470665907
SigmaZ dB	1.996895442	2.32190975	1.319452603	1.915800836
SigmaXYZ dB	1.543333704	1.933809346	3.082187683	3.013724628

### 4.3. Measurement and qualification of the chamber

This section is divided into three parts. The first part is related to the measurement configuration and data extraction from the S-parameters. The second part is related to the prototype of the reverberation chamber with metallic walls and metamaterial walls. And the third part is related to the LUF extracted from measurement results, the comparison with simulation and between the two prototypes.

#### 4.3.1. Measurement configuration and data extraction

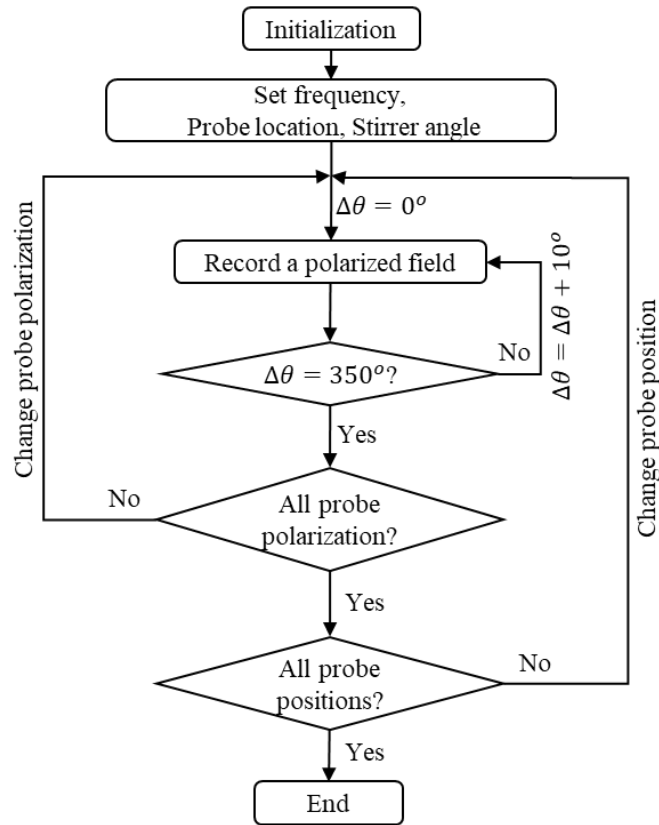
For the field uniformity validation by the measurement, the equipments are the reverberation chamber (with metallic walls and with metamaterial walls), the vector network analyzer model ANRITSU 37369C, the E-field probe system model EFS-105 and the double ridged horn antenna model DRH20E. In the reverberation chamber, the rotation of the stirrer is automatically controlled by the designed GUI on the stepper motors with built-in controller model ZABER X-NMS23. First, the chamber with aluminum walls is measured then two metamaterial panels are added on two metallic walls distant of 30 cm from each other to measure the metamaterials walls RC. The configuration of the measurement system is shown in Figure 4.12.



*Figure 4.12 : Measurement configuration for RC qualification*

In this configuration, the VNA is connected to the excitation antenna through port 1 and to the field probe base unit through port 2. The electric field probe will be moved along each point represented by  $FP1, \dots, FP9$  for 3 polarizations. During the measurement, the VNA is only sending power on port 1, for probe protection. It measures therefore only  $S_{21}$  and  $S_{11}$ . The measurement is

done for antenna position of case 1, 9 field probe locations and 36 stirrer step angles. For each polarization, the probe must be moved (position + polarization). So, the total number is  $9 \times 3 = 27$  positions of the probe. The measurement procedure is shown in Figure 4.13.



**Figure 4.13 : Measurement procedure**

In this procedure, the measurement frequency points, the 1<sup>st</sup> location and 1<sup>st</sup> polarization of the field probe are set. The stirrer angle is set to  $0^\circ$ . Then the  $S_{21}$  parameter is recorded. This data will be used to get the electric field strength as described below. Then, the stirrer's angle is increased by step of  $10^\circ$  and the  $S_{21}$  is recorded again. The stirrer's angle is increased until  $350^\circ$  which means that one cycle is completed and the  $S_{21}$  is recorded for each stirrer angle. In the 2<sup>nd</sup> step, the measurement is done on the 2<sup>nd</sup> polarization by changing the axis of the probe head to another direction. The measurements of the  $S_{21}$  for each stirrer angle are repeated again from  $0^\circ$  until  $350^\circ$  which corresponds to 36 angles in total. Then, the measurement on the 3<sup>rd</sup> polarization is done the same way. At the 3<sup>rd</sup> step, the measurement is done on a new location (FP points) of the field probe. The procedure of changing the polarization as in the 2<sup>nd</sup> step as well as changing the stirrer angle as in the 1<sup>st</sup> step is repeated again on this new location of field probe. The measurement is done the same way for the 9 locations of field probe. Finally, all the  $S_{21}$  data for all 9 probe locations, 3 polarizations and 36 stirrer angles are recorded on the 20 frequency points. The AF antenna factor and  $Z_0$  impedance are combined with measurement data to extract the electric field strength as presented in the next section.

The measurement frequency is from 1.5 GHz to 4.5 GHz within the 20 frequency points selected with the logarithmic distribution. The  $S_{21}$  parameters including the antenna factor (AF) and the impedance  $Z_0$  are used to calculate the electric field strength measured from the field probe. As example  $\hat{E}_{x,p}$  from the formula (2.4) of chapter 2 can be modified according to the measurement data as in the following analysis.

$$\hat{E}_{x,p} = \frac{\max_{\varphi \in \{0,10^\circ, \dots, 350^\circ\}} \|\vec{E}_{x,p}\|}{\sqrt{P_{input}}} \quad (4.2)$$

where  $\varphi$  is the stirrer angle position,  $p$  is the location of field probe,  $P_{input}$  is the input power.

The VNA measures  $S_{21}$ . So,

$$|S_{21}| = \sqrt{\frac{P_{trans}}{P_{input}}} \quad (4.3)$$

where  $P_{trans}$  is the transmitted power from port 1 to port 2:  $P_{trans} = \frac{V^2}{Z_0}$  with  $Z_0 = 50\Omega$ . The input power  $P_{input}$  is the injected power through port 1.

The relation between the electric field and voltage, in the probe use, is linked by the antenna factor (AF):

$$\hat{E}_{x,p} = AF \times V$$

Since  $P_{trans} = \frac{V^2}{Z_0}$ ,  $V$  is deduced with  $V = \sqrt{Z_0 P_{trans}}$

$$\text{So, } \hat{E}_{x,p} = |S_{21}| AF \sqrt{Z_0 P_{input}}$$

Finally, the normalized electric field is calculated as

$$\hat{E}_{x,p} = \frac{\max_{0 \leq \varphi \leq \varphi_N} (|S_{21}| AF \sqrt{Z_0 P_{input}})}{\sqrt{P_{input}}} \quad (4.4)$$

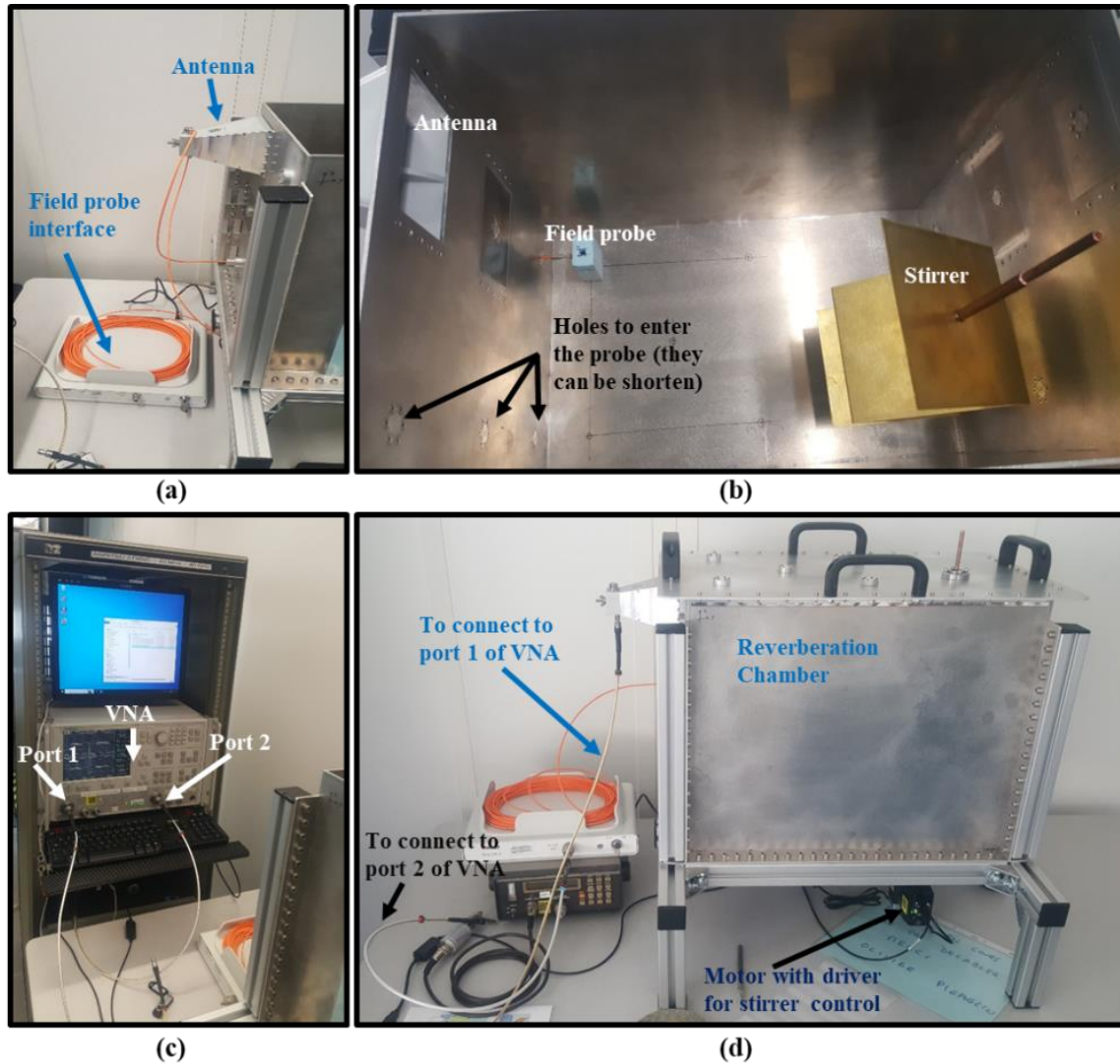
$$\hat{E}_{x,p} = \max_{\varphi \in \{0,10^\circ, \dots, 350^\circ\}} (|S_{21}| AF \sqrt{Z_0})$$



Finally, the normalized electric field strength for the  $y$  and  $z$  polarization as in formula (2.5) and (2.6) are calculated the same way. The formula (2.7) to (2.18) are then used to get the standard deviation of the electric field in the working volume.

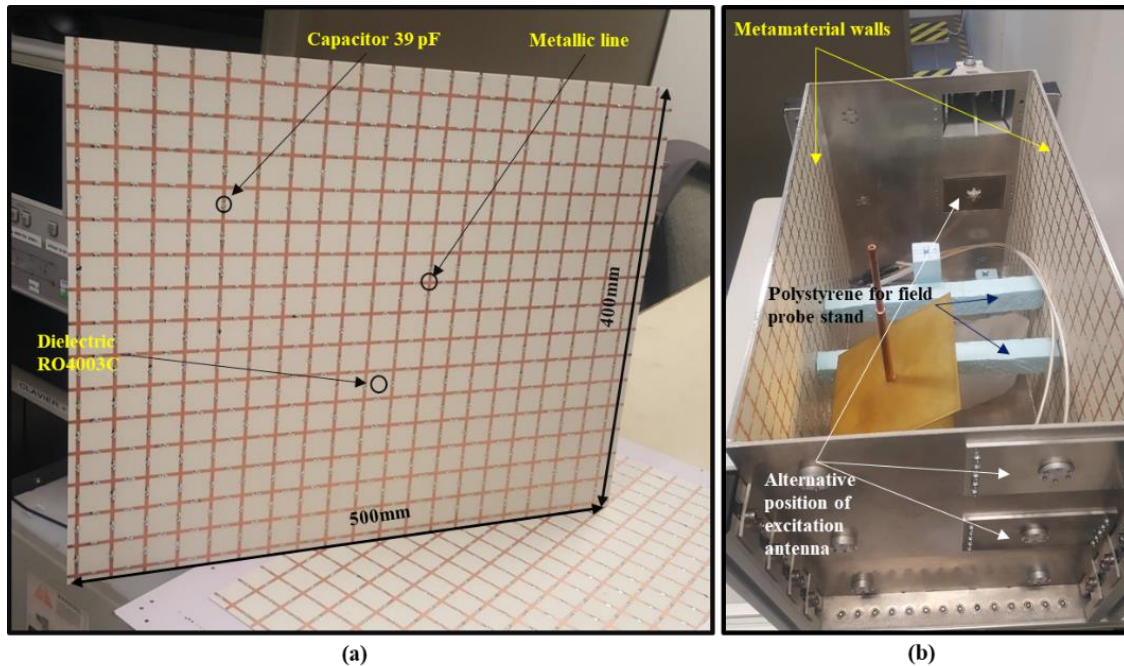
### 4.3.2. Chamber prototype with metallic and with metamaterial walls

The prototype of the reverberation chamber with aluminum walls is shown in Figure 4.14. The antenna, the electric field probe, the VNA, the coaxial cables, the optic fiber and the stirrer inside the chamber are also shown here. This configuration is used for the qualification of the reverberation chamber.



*Figure 4.14: The equipment for chamber qualification (a) Antenna and field probe (b) Inside view of aluminium walls chamber including field probe head and stirrer (c) VNA (d) Whole chamber structure*

As stated in the previous section, the prototype of the reverberation chamber with the metamaterial walls is achieved by adding the metamaterial panels on the metallic walls of the conventional chamber. This configuration gives the possibility to use only one chamber for the two cases. The other advantage is the possibility to use different metamaterial panels for future research. The reverberation chamber with metamaterial walls is shown in Figure 4.15. The metamaterial panel with  $16 \text{ cells} \times 20 \text{ cells}$  constructed on the RO4003C of size  $400\text{mm} \times 500\text{mm}$  which is also shown in the same figure. To ease the measurement, the polystyrene is used to support the probe head.



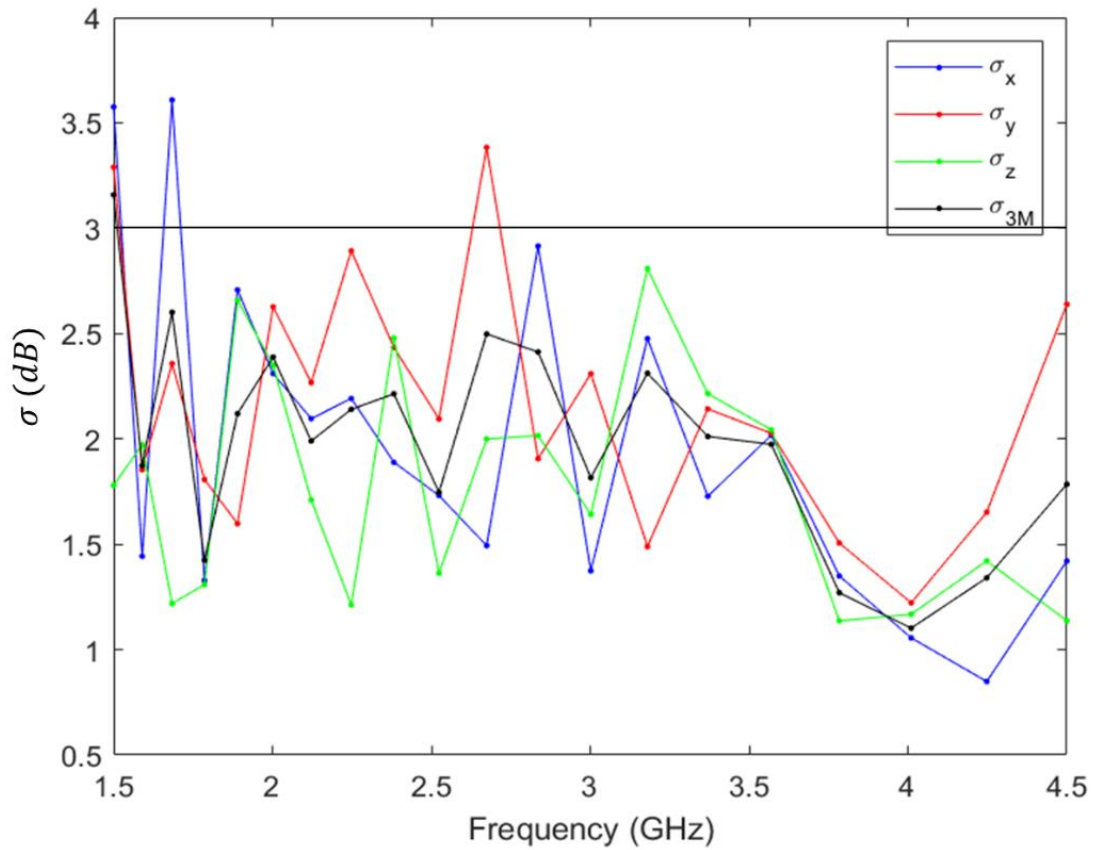
*Figure 4.15 : (a) One of the metamaterial wall (b) Inside view of reverberation chamber with metamaterial walls*

### **4.3.3. LUF results, comparison and discussion**

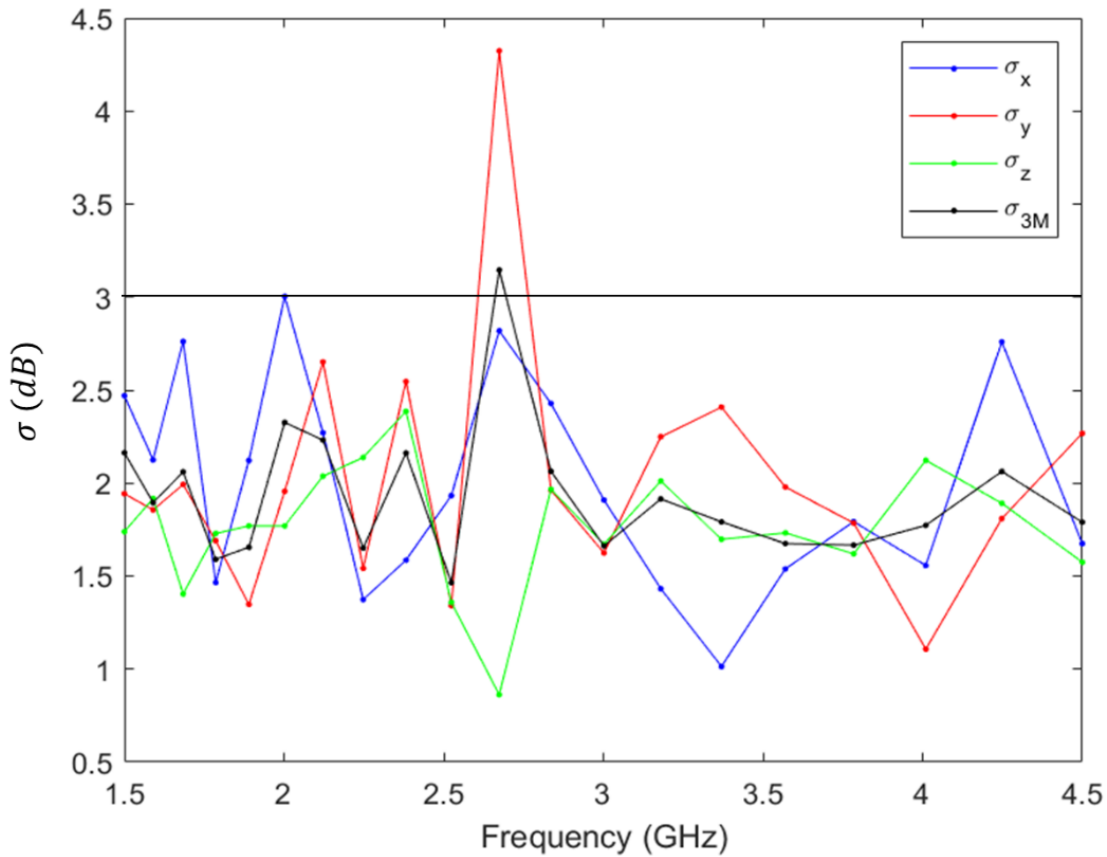
The standard deviation results extracted from the measurements of the chamber with aluminum walls is shown in Figure 4.16. The results show that the LUF of this aluminum walls reverberation chamber is around  $2.674 \text{ GHz}$ , with several peaks above  $3 \text{ dB}$  below this frequency. Compared to the simulation results in the same condition presented in Table 4.12, simulation and measurement are in good agreement.

The standard deviation results of the reverberation chamber with metamaterial walls extracted from the measurement data is shown in Figure 4.17. The results show that all the peaks are below the  $3 \text{ dB}$  limit except at  $2.674 \text{ GHz}$  frequency. This results can potentially be due to the lack of measurement points or the unsuitable optimal position of the antenna. Additional tests should be carried out to try to determine its origin and eliminate it. Nevertheless, the LUF could be reduced

below 1.5 GHz if this problematic point is excluded. Since simulations could not be performed above 2.118 GHz, the results at this frequency could not be predicted. Since results were slightly sensitive to antenna position, other test might be done in measurements for other antenna position.



*Figure 4.16 : The standard deviation result for the reverberation chamber with aluminum walls*



*Figure 4.17 : The standard deviation result for the reverberation chamber with metamaterial walls*

#### **4.4. Conclusion**

In this chapter, the analysis and design of the reverberation chamber has been done. The chamber components such as the metallic walls, the metamaterial walls, the stirrer, the excitation antenna, the location of the field probes and the number of stirrer angles are also analyzed and selected through standard deviation performances. The prototypes with and without the metamaterial walls are constructed and measured. The results indicate the improvement of the field uniformity of the chamber with metamaterial walls at low frequency and on the band even if at one particular frequency the 3 dB limit is exceeded.

## Chapter 5: Conclusions and future perspectives

In this manuscript, a small reverberation chamber with metallic walls and with metamaterial walls is designed, analyzed, constructed and measured. Field observation leads to evaluation of the lowest usable frequency. The reverberation chamber which is a choice amongst many testing environments is validated according to the IEC 61000-4-21 standard by using a vector network analyzer, a double ridged horn antenna and an electric field probe. Before the measurement validation, the reverberation chamber with two anisotropic walls is analyzed by using the modal expansion theory method modified for the rectangular cavity. The metamaterials are selected for characterization and measurement validation by using waveguide calibration kit. The materials and components of this reverberation chamber are reviewed, analyzed, selected and modeled through Ansys-HFSS simulations. The prototype of the metallic walls reverberation chamber is constructed for measurement validation, then two metamaterial panels are hanged on two parallel walls to test the reverberation chamber with metamaterial walls. Comparison is made between the chamber with metallic walls and with metamaterial walls. The results are promising for the reduction of the LUF with metamaterial walls.

From the beginning of the thesis until the measurement validation of the reverberation chamber, many tasks and results have been completed. However, several short-term and long-term perspectives are envisaged:

- Perspective 1: One possibility is the measurement validation with alternative location of the double ridged horn antenna hanged on the chamber walls. Changing the antenna position may lead to better results with metamaterial walls.
- Perspective 2: LUF may be improved by using different structures of the metamaterial. This improvement should spend less time since the prototype of the chamber is already constructed. For example, the capacitor value may be increased to reduce the LUF at lower frequencies.
- Perspective 3: Related to the excitation antenna, a small antenna which can operated at low frequency (lower than  $1.5\text{ GHz}$ ) could be designed to be used in this chamber. It allows tests at lower frequencies than  $1.5\text{ GHz}$  to search for the exact LUF in metamaterial case. This antenna may be inserted in the cavity if its size is small enough.
- Perspective 4: Related to the analysis of the chamber with metamaterial walls, only the anisotropic walls with constant surface impedance have been set in MET. To improve it, the MET should be combined to the FEM analysis on the metamaterial unit cell to give the information of the frequency dependency on the surface impedance of the unit cell. This improvement would help for LUF optimization with realistic metamaterial and limited computation time if the MET is used.

# Annex

## **6.1. Relation between the transverse and the longitudinal components of the electromagnetic field**

From Maxwell's equations:

$$\nabla \times \vec{E} = -j\omega\mu_0 \vec{H} \quad (6.1)$$

$$\nabla \times \vec{H} = j\omega\varepsilon_0\varepsilon_r \vec{E} \quad (6.2)$$

The electromagnetic field is the combination of the transverse and the longitudinal components as written in the form below:

$$\vec{E} = \vec{E}_T + E_z \vec{z} \quad (6.3)$$

$$\vec{H} = \vec{H}_T + H_z \vec{z} \quad (6.4)$$

$$\nabla = \nabla_T + \delta_z \vec{z} \quad (6.5)$$

### **6.1.1. Propagating in the forward direction (formula with term $e^{-\gamma_z z}$ )**

The equation (6.5) become:

$$\nabla = \nabla_T - \gamma_z \vec{z} \quad (6.6)$$

Then,

$$\begin{cases} (\nabla_T - \gamma_z \vec{z}) \times (\vec{E}_T + E_z \vec{z}) = -j\omega\mu_0 (\vec{H}_T + H_z \vec{z}) \\ (\nabla_T - \gamma_z \vec{z}) \times (\vec{H}_T + H_z \vec{z}) = j\omega\varepsilon_0\varepsilon_r (\vec{E}_T + E_z \vec{z}) \end{cases}$$

$$\begin{cases} \nabla_T \times \vec{E}_T + \nabla_T \times (E_z \vec{z}) - \gamma_z (\vec{z} \times \vec{E}_T) - \gamma_z E_z (\vec{z} \times \vec{z}) = -j\omega\mu_0 (\vec{H}_T + H_z \vec{z}) \\ \nabla_T \times \vec{H}_T + \nabla_T \times (H_z \vec{z}) - \gamma_z (\vec{z} \times \vec{H}_T) - \gamma_z H_z (\vec{z} \times \vec{z}) = j\omega\varepsilon_0\varepsilon_r (\vec{E}_T + E_z \vec{z}) \end{cases}$$

Because:

$$\gamma_z E_z (\vec{z} \times \vec{z}) = \gamma_z E_z (\vec{0}) = \vec{0}$$

$$\gamma_z H_z (\vec{z} \times \vec{z}) = \gamma_z H_z (\vec{0}) = \vec{0}$$

$$\nabla_T \times (E_z \vec{z}) = E_z \nabla_T \times \vec{z} + \nabla_T E_z \times \vec{z} = \vec{0} + \nabla_T E_z \times \vec{z} = \nabla_T E_z \times \vec{z}$$

$$\nabla_T \times (H_z \vec{z}) = H_z \nabla_T \times \vec{z} + \nabla_T H_z \times \vec{z} = \vec{0} + \nabla_T H_z \times \vec{z} = \nabla_T H_z \times \vec{z}$$

So,

$$\begin{cases} \nabla_T \times \vec{E}_T + (\nabla_T E_z) \times \vec{z} - \gamma_z (\vec{z} \times \vec{E}_T) = -j\omega\mu_0 (\vec{H}_T + H_z \vec{z}) \\ \nabla_T \times \vec{H}_T + (\nabla_T H_z) \times \vec{z} - \gamma_z (\vec{z} \times \vec{H}_T) = j\omega\varepsilon_0 \varepsilon_r (\vec{E}_T + E_z \vec{z}) \end{cases}$$

$$\begin{cases} \nabla_T \times \vec{E}_T + (\nabla_T E_z) \times \vec{z} - \gamma_z (\vec{z} \times \vec{E}_T) = -j\omega\mu_0 \vec{H}_T - j\omega\mu_0 H_z \vec{z} \\ \nabla_T \times \vec{H}_T + (\nabla_T H_z) \times \vec{z} - \gamma_z (\vec{z} \times \vec{H}_T) = j\omega\varepsilon_0 \varepsilon_r \vec{E}_T + j\omega\varepsilon_0 \varepsilon_r E_z \vec{z} \end{cases}$$

This system is projected on the transverse components in (6.7) and (6.8) equations and along the longitudinal components on (6.9) and (6.10) equations.

$$(\nabla_T E_z) \times \vec{z} - \gamma_z (\vec{z} \times \vec{E}_T) = -j\omega\mu_0 \vec{H}_T \quad (6.7)$$

$$(\nabla_T H_z) \times \vec{z} - \gamma_z (\vec{z} \times \vec{H}_T) = j\omega\varepsilon_0 \varepsilon_r \vec{E}_T \quad (6.8)$$

$$\nabla_T \times \vec{E}_T = -j\omega\mu_0 H_z \vec{z} \quad (6.9)$$

$$\nabla_T \times \vec{H}_T = j\omega\varepsilon_0 \varepsilon_r E_z \vec{z} \quad (6.10)$$

Applying to (6.7) with  $\gamma_z \vec{z}$  and multiplying (6.8) with  $j\omega\mu_0$  and adding these equations, we get:

$$+ \begin{cases} \gamma_z \vec{z} \times (\nabla_T E_z) \times \vec{z} - \gamma_z^2 \vec{z} \times (\vec{z} \times \vec{E}_T) = -j\omega\mu_0 \gamma_z (\vec{z} \times \vec{H}_T) \\ j\omega\mu_0 (\nabla_T H_z) \times \vec{z} - j\omega\mu_0 \gamma_z (\vec{z} \times \vec{H}_T) = -\omega^2 \mu_0 \varepsilon_0 \varepsilon_r \vec{E}_T \end{cases}$$

$$\gamma_z \vec{z} \times (\nabla_T E_z) \times \vec{z} - \gamma_z^2 \vec{z} \times (\vec{z} \times \vec{E}_T) + j\omega\mu_0 (\nabla_T H_z) \times \vec{z} = -\omega^2 \mu_0 \varepsilon_0 \varepsilon_r \vec{E}_T = -k_0^2 \varepsilon_r \vec{E}_T \quad (6.11)$$

where  $k_0^2 = \omega^2 \mu_0 \varepsilon_0$

From vector identity:  $\vec{A} \times (\vec{B} \times \vec{C}) = (\vec{A} \cdot \vec{C}) \vec{B} - (\vec{A} \cdot \vec{B}) \vec{C}$ , we got

$$\vec{z} \times (\nabla_T \mathbf{E}_z) \times \vec{z} = (\vec{z} \cdot \vec{z}) \nabla_T \mathbf{E}_z - (\vec{z} \cdot \nabla_T \mathbf{E}_z) \vec{z} = \nabla_T \mathbf{E}_z - 0 = \nabla_T \mathbf{E}_z$$

$$\vec{z} \times (\vec{z} \times \vec{E}_T) = (\vec{z} \cdot \vec{E}_T) \vec{z} - (\vec{z} \cdot \vec{z}) \vec{E}_T = 0 - \vec{E}_T = -\vec{E}_T$$

Then, (6.11) become,

$$+\gamma_z (\nabla_T \mathbf{E}_z) - \gamma_z^2 (-\vec{E}_T) + j\omega\mu_0 (\nabla_T \mathbf{H}_z) \times \vec{z} = -k_0^2 \epsilon_r \vec{E}_T$$

$$\gamma_z (\nabla_T \mathbf{E}_z) - \gamma_z^2 (-\vec{E}_T) + j\omega\mu_0 (\nabla_T \mathbf{H}_z) \times \vec{z} + k_0^2 \epsilon_r \vec{E}_T = \vec{0}$$

$$\gamma_z (\nabla_T \mathbf{E}_z) + \gamma_z^2 \vec{E}_T + j\omega\mu_0 (\nabla_T \mathbf{H}_z) \times \vec{z} + k_0^2 \epsilon_r \vec{E}_T = \vec{0}$$

$$(\gamma_z^2 + k_0^2 \epsilon_r) \vec{E}_T = -\gamma_z (\nabla_T \mathbf{E}_z) - j\omega\mu_0 (\nabla_T \mathbf{H}_z) \times \vec{z} \quad (6.12)$$

Applying (6.7) with  $j\omega\epsilon_0\epsilon_r$  and multiplying (6.8) with  $-\gamma_z \vec{z}$  and adding these equations, we get:

$$+\begin{cases} j\omega\epsilon_0\epsilon_r (\nabla_T \mathbf{E}_z) \times \vec{z} - j\omega\epsilon_0\epsilon_r \gamma_z (\vec{z} \times \vec{E}_T) = \omega^2 \mu_0 \epsilon_0 \epsilon_r \vec{H}_T \\ -\gamma_z \vec{z} \times (\nabla_T \mathbf{H}_z) \times \vec{z} + \gamma_z^2 \vec{z} \times (\vec{z} \times \vec{H}_T) = -j\omega\epsilon_0\epsilon_r \gamma_z (\vec{z} \times \vec{E}_T) \end{cases}$$

$$j\omega\epsilon_0\epsilon_r (\nabla_T \mathbf{E}_z) \times \vec{z} - \gamma_z \vec{z} \times (\nabla_T \mathbf{H}_z) \times \vec{z} + \gamma_z^2 \vec{z} \times (\vec{z} \times \vec{H}_T) = \omega^2 \mu_0 \epsilon_0 \epsilon_r \vec{H}_T = k_0^2 \epsilon_r \vec{H}_T \quad (6.13)$$

By using the vector identity formula, the same as the procedure above, we got:

$$\vec{z} \times (\nabla_T \mathbf{H}_z) \times \vec{z} = (\vec{z} \cdot \vec{z}) \nabla_T \mathbf{H}_z - (\vec{z} \cdot \nabla_T \mathbf{H}_z) \vec{z} = \nabla_T \mathbf{H}_z$$

$$\vec{z} \times (\vec{z} \times \vec{H}_T) = (\vec{z} \cdot \vec{H}_T) \vec{z} - (\vec{z} \cdot \vec{z}) \vec{H}_T = -\vec{H}_T$$

Then (6.14) become,

$$j\omega\epsilon_0\epsilon_r (\nabla_T \mathbf{E}_z) \times \vec{z} - \gamma_z (\nabla_T \mathbf{H}_z) + \gamma_z^2 (-\vec{H}_T) = k_0^2 \epsilon_r \vec{H}_T$$

$$j\omega\epsilon_0\epsilon_r (\nabla_T \mathbf{E}_z) \times \vec{z} - \gamma_z (\nabla_T \mathbf{H}_z) - \gamma_z^2 \vec{H}_T - k_0^2 \epsilon_r \vec{H}_T = \vec{0}$$

$$(\gamma_z^2 + k_0^2 \epsilon_r) \vec{H}_T = -\gamma_z (\nabla_T \mathbf{H}_z) + j\omega\epsilon_0\epsilon_r (\nabla_T \mathbf{E}_z) \times \vec{z} \quad (6.14)$$

### **6.1.2. Propagating in the backward direction (formula with term $e^{+\gamma_z z}$ )**

The equation (6.5) become:



$$\nabla = \nabla_T + \gamma_z \vec{z} \quad (6.15)$$

Then,

$$\begin{cases} (\nabla_T + \gamma_z \vec{z}) \times (\vec{E}_T + E_z \vec{z}) = -j\omega\mu_0 (\vec{H}_T + H_z \vec{z}) \\ (\nabla_T + \gamma_z \vec{z}) \times (\vec{H}_T + H_z \vec{z}) = j\omega\varepsilon_0\varepsilon_r (\vec{E}_T + E_z \vec{z}) \end{cases}$$

$$\begin{cases} \nabla_T \times \vec{E}_T + \nabla_T \times (E_z \vec{z}) + \gamma_z (\vec{z} \times \vec{E}_T) + \gamma_z E_z (\vec{z} \times \vec{z}) = -j\omega\mu_0 (\vec{H}_T + H_z \vec{z}) \\ \nabla_T \times \vec{H}_T + \nabla_T \times (H_z \vec{z}) + \gamma_z (\vec{z} \times \vec{H}_T) + \gamma_z H_z (\vec{z} \times \vec{z}) = j\omega\varepsilon_0\varepsilon_r (\vec{E}_T + E_z \vec{z}) \end{cases}$$

Because:

$$\begin{aligned} \gamma_z E_z (\vec{z} \times \vec{z}) &= \gamma_z E_z (0) = \vec{0} \\ \gamma_z H_z (\vec{z} \times \vec{z}) &= \gamma_z H_z (0) = \vec{0} \end{aligned}$$

$$\begin{aligned} \nabla_T \times (E_z \vec{z}) &= E_z \nabla_T \times \vec{z} + \nabla_T E_z \times \vec{z} = \vec{0} + \nabla_T E_z \times \vec{z} = \nabla_T E_z \times \vec{z} \\ \nabla_T \times (H_z \vec{z}) &= H_z \nabla_T \times \vec{z} + \nabla_T H_z \times \vec{z} = \vec{0} + \nabla_T H_z \times \vec{z} = \nabla_T H_z \times \vec{z} \end{aligned}$$

So,

$$\begin{cases} \nabla_T \times \vec{E}_T + (\nabla_T E_z) \times \vec{z} + \gamma_z (\vec{z} \times \vec{E}_T) = -j\omega\mu_0 (\vec{H}_T + H_z \vec{z}) \\ \nabla_T \times \vec{H}_T + (\nabla_T H_z) \times \vec{z} + \gamma_z (\vec{z} \times \vec{H}_T) = j\omega\varepsilon_0\varepsilon_r (\vec{E}_T + E_z \vec{z}) \end{cases}$$

$$\begin{cases} \nabla_T \times \vec{E}_T + (\nabla_T E_z) \times \vec{z} + \gamma_z (\vec{z} \times \vec{E}_T) = -j\omega\mu_0 \vec{H}_T - j\omega\mu_0 H_z \vec{z} \\ \nabla_T \times \vec{H}_T + (\nabla_T H_z) \times \vec{z} + \gamma_z (\vec{z} \times \vec{H}_T) = j\omega\varepsilon_0\varepsilon_r \vec{E}_T + j\omega\varepsilon_0\varepsilon_r E_z \vec{z} \end{cases}$$

This system is projected on the transverse components in (6.16) and (6.17) equations and along the longitudinal components on (6.18) and (6.19) equations.

$$(\nabla_T E_z) \times \vec{z} + \gamma_z (\vec{z} \times \vec{E}_T) = -j\omega\mu_0 \vec{H}_T \quad (6.16)$$

$$(\nabla_T H_z) \times \vec{z} + \gamma_z (\vec{z} \times \vec{H}_T) = j\omega\varepsilon_0\varepsilon_r \vec{E}_T \quad (6.17)$$

$$\nabla_T \times \vec{E}_T = -j\omega\mu_0 H_z \vec{z} \quad (6.18)$$

$$\nabla_T \times \vec{H}_T = j\omega\varepsilon_0\varepsilon_r E_z \vec{z} \quad (6.19)$$

Applying (6.16) with  $-\gamma_z \vec{z}$  and multiplying (6.17) with  $j\omega\mu_0$  and adding these equations, we get:

$$\begin{aligned}
& + \begin{cases} -\gamma_z \vec{z} \times (\nabla_T E_z) \times \vec{z} - \gamma_z^2 \vec{z} \times (\vec{z} \times \vec{E}_T) = -j\omega\mu_0 \gamma_z (\vec{z} \times \vec{H}_T) \\ j\omega\mu_0 (\nabla_T H_z) \times \vec{z} + j\omega\mu_0 \gamma_z (\vec{z} \times \vec{H}_T) = -\omega^2 \mu_0 \varepsilon_0 \varepsilon_r \vec{E}_T \end{cases} \\
& -\gamma_z \vec{z} \times (\nabla_T E_z) \times \vec{z} - \gamma_z^2 \vec{z} \times (\vec{z} \times \vec{E}_T) + j\omega\mu_0 (\nabla_T H_z) \times \vec{z} = -\omega^2 \mu_0 \varepsilon_0 \varepsilon_r \vec{E}_T = -k_0^2 \varepsilon_r \vec{E}_T \quad (6.20)
\end{aligned}$$

where  $k_0^2 = \omega^2 \mu_0 \varepsilon_0$

From vector identity:  $\vec{A} \times (\vec{B} \times \vec{C}) = (\vec{A} \cdot \vec{C}) \vec{B} - (\vec{A} \cdot \vec{B}) \vec{C}$ , we got

$$\vec{z} \times (\nabla_T E_z) \times \vec{z} = (\vec{z} \cdot \vec{z}) \nabla_T E_z - (\vec{z} \cdot \nabla_T E_z) \vec{z} = \nabla_T E_z - 0 = \nabla_T E_z$$

$$\vec{z} \times (\vec{z} \times \vec{E}_T) = (\vec{z} \cdot \vec{E}_T) \vec{z} - (\vec{z} \cdot \vec{z}) \vec{E}_T = 0 - \vec{E}_T = -\vec{E}_T$$

Then, (6.12) become,

$$\begin{aligned}
& -\gamma_z (\nabla_T E_z) - \gamma_z^2 (-\vec{E}_T) + j\omega\mu_0 (\nabla_T H_z) \times \vec{z} = -k_0^2 \varepsilon_r \vec{E}_T \\
& -\gamma_z (\nabla_T E_z) - \gamma_z^2 (-\vec{E}_T) + j\omega\mu_0 (\nabla_T H_z) \times \vec{z} + k_0^2 \varepsilon_r \vec{E}_T = \vec{0} \\
& -\gamma_z (\nabla_T E_z) + \gamma_z^2 \vec{E}_T + j\omega\mu_0 (\nabla_T H_z) \times \vec{z} + k_0^2 \varepsilon_r \vec{E}_T = \vec{0} \\
& (\gamma_z^2 + k_0^2 \varepsilon_r) \vec{E}_T = \gamma_z (\nabla_T E_z) - j\omega\mu_0 (\nabla_T H_z) \times \vec{z} \quad (6.21)
\end{aligned}$$

Applying (6.16) with  $j\omega\varepsilon_0\varepsilon_r$  and multiplying (6.17) with  $\gamma_z \vec{z}$  and adding these equations, we get:

$$\begin{aligned}
& + \begin{cases} j\omega\varepsilon_0\varepsilon_r (\nabla_T E_z) \times \vec{z} + j\omega\varepsilon_0\varepsilon_r \gamma_z (\vec{z} \times \vec{E}_T) = \omega^2 \mu_0 \varepsilon_0 \varepsilon_r \vec{H}_T \\ \gamma_z \vec{z} \times (\nabla_T H_z) \times \vec{z} + \gamma_z^2 \vec{z} \times (\vec{z} \times \vec{H}_T) = j\omega\varepsilon_0\varepsilon_r \gamma_z (\vec{z} \times \vec{E}_T) \end{cases} \\
& j\omega\varepsilon_0\varepsilon_r (\nabla_T E_z) \times \vec{z} + \gamma_z \vec{z} \times (\nabla_T H_z) \times \vec{z} + \gamma_z^2 \vec{z} \times (\vec{z} \times \vec{H}_T) = \omega^2 \mu_0 \varepsilon_0 \varepsilon_r \vec{H}_T = k_0^2 \varepsilon_r \vec{H}_T \quad (6.22)
\end{aligned}$$

By using the vector identity formula, the same as the procedure above, we got:

$$\vec{z} \times (\nabla_T H_z) \times \vec{z} = (\vec{z} \cdot \vec{z}) \nabla_T H_z - (\vec{z} \cdot \nabla_T H_z) \vec{z} = \nabla_T H_z$$

$$\vec{z} \times (\vec{z} \times \vec{H}_T) = (\vec{z} \cdot \vec{H}_T) \vec{z} - (\vec{z} \cdot \vec{z}) \vec{H}_T = -\vec{H}_T$$

Then (6.14) become,

$$j\omega\varepsilon_0\varepsilon_r(\nabla_T E_z) \times \vec{z} + \gamma_z(\nabla_T H_z) + \gamma_z^2(-\vec{H}_T) = k_0^2\varepsilon_r\vec{H}_T$$

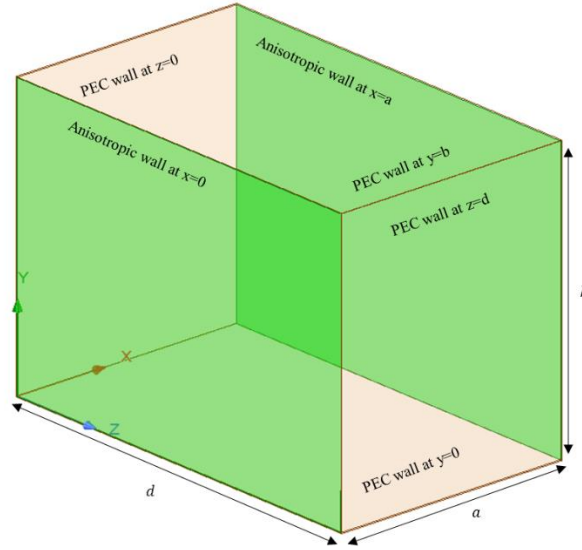
$$j\omega\varepsilon_0\varepsilon_r(\nabla_T E_z) \times \vec{z} + \gamma_z(\nabla_T H_z) - \gamma_z^2\vec{H}_T - k_0^2\varepsilon_r\vec{H}_T = \vec{0}$$

$$(\gamma_z^2 + k_0^2\varepsilon_r)\vec{H}_T = \gamma_z(\nabla_T H_z) + j\omega\varepsilon_0\varepsilon_r(\nabla_T E_z) \times \vec{z} \quad (6.23)$$

## 6.2. MET analysis for the rectangular cavity with two anisotropic walls

In this annex, the detailed analysis of the rectangular cavity with two anisotropic surface impedance walls will be presented. In this analysis, the expression of the longitudinal components, the transverse components and their substitution in the surface boundary conditions will be showed in detail.

### 6.2.1. Longitudinal components of electromagnetic field



*Figure 6.1 : Representation model of reverberation chamber with two anisotropic walls*

According to the PEC boundary condition at the walls  $y = 0, y = b, z = 0, z = d$  and the anisotropic boundary condition at  $x = 0$  and  $x = a$  as represented in Figure 6.1. Suppose the expression  $k_z = \frac{p\pi}{d}$  is the phase constant along  $z$  direction, then the expression  $\gamma_z = jk_z = j\frac{p\pi}{d}$  is the propagation constant along  $z$  direction. The parameters  $n$  and  $p$  are the integers. The planes  $x = 0$  and  $x = a$  are anisotropic impedance surfaces. The propagation constant along  $x$  direction here is represented by the variable  $\gamma_x$  which is unknown and needs to be found.

The expression of the longitudinal components of the EM field can be written as:

$$E_z = P_z \left[ A_x \cosh(\gamma_x x) + B_x \sinh(\gamma_x x) \right] e^{-\gamma_z z} \sin(k_y y) + Q_z \left[ A_x \cosh(\gamma_x x) + B_x \sinh(\gamma_x x) \right] e^{+\gamma_z z} \sin(k_y y) \quad (6.24)$$

$$\begin{aligned}
H_z &= R_z \left[ C_x \cosh(\gamma_x x) + D_x \sinh(\gamma_x x) \right] e^{-\gamma_z z} \cos(k_y y) \\
&\quad + T_z \left[ C_x \cosh(\gamma_x x) + D_x \sinh(\gamma_x x) \right] e^{+\gamma_z z} \cos(k_y y)
\end{aligned} \tag{6.25}$$

By simplifying (6.24):

$$\begin{aligned}
E_z &= \left[ P_z A_x \cosh(\gamma_x x) + P_z B_x \sinh(\gamma_x x) \right] e^{-\gamma_z z} \sin(k_y y) \\
&\quad + \left[ Q_z A_x \cosh(\gamma_x x) + Q_z B_x \sinh(\gamma_x x) \right] e^{+\gamma_z z} \sin(k_y y) \\
E_z &= \left[ \alpha_1 \cosh(\gamma_x x) + \alpha_2 \sinh(\gamma_x x) \right] e^{-\gamma_z z} \sin(k_y y) \\
&\quad + \left[ \alpha_3 \cosh(\gamma_x x) + \alpha_4 \sinh(\gamma_x x) \right] e^{+\gamma_z z} \sin(k_y y)
\end{aligned} \tag{6.26}$$

where  $\alpha_1 = P_z A_x$ ;  $\alpha_2 = P_z B_x$ ;  $\alpha_3 = Q_z A_x$ ;  $\alpha_4 = Q_z B_x$

By simplifying (6.25):

$$\begin{aligned}
H_z &= \left[ R_z C_x \cosh(\gamma_x x) + R_z D_x \sinh(\gamma_x x) \right] e^{-\gamma_z z} \cos(k_y y) \\
&\quad + \left[ T_z C_x \cosh(\gamma_x x) + T_z D_x \sinh(\gamma_x x) \right] e^{+\gamma_z z} \cos(k_y y) \\
H_z &= \left[ \beta_1 \cosh(\gamma_x x) + \beta_2 \sinh(\gamma_x x) \right] e^{-\gamma_z z} \cos(k_y y) \\
&\quad + \left[ \beta_3 \cosh(\gamma_x x) + \beta_4 \sinh(\gamma_x x) \right] e^{+\gamma_z z} \cos(k_y y)
\end{aligned} \tag{6.27}$$

where  $\beta_1 = R_z C_x$ ;  $\beta_2 = R_z D_x$ ;  $\beta_3 = T_z C_x$ ;  $\beta_4 = T_z D_x$

**The boundary conditions at walls  $z = 0$  and  $z = d$  are**

$$\left. \frac{\delta E_z}{\delta z} \right|_{z=0} = 0 ; \left. \frac{\delta E_z}{\delta z} \right|_{z=d} = 0 ; H_z \Big|_{z=0} = 0 ; H_z \Big|_{z=d} = 0$$

Deriving (6.26) with  $\delta z$

$$\begin{aligned}
\frac{\delta E_z}{\delta z} &= -\gamma_z \left[ \alpha_1 \cosh(\gamma_x x) + \alpha_2 \sinh(\gamma_x x) \right] e^{-\gamma_z z} \sin(k_y y) \\
&\quad + \gamma_z \left[ \alpha_3 \cosh(\gamma_x x) + \alpha_4 \sinh(\gamma_x x) \right] e^{+\gamma_z z} \sin(k_y y)
\end{aligned}$$

At wall  $z = 0$

$$\gamma_z \sin(k_y y) \left[ -\alpha_1 \cosh(\gamma_x x) - \alpha_2 \sinh(\gamma_x x) + \alpha_3 \cosh(\gamma_x x) + \alpha_4 \sinh(\gamma_x x) \right] = 0$$

$$(\alpha_3 - \alpha_1) \cosh(\gamma_x x) + (\alpha_4 - \alpha_2) \sinh(\gamma_x x) = 0 \quad (6.28)$$

Knowing that  $\alpha_1, \alpha_2, \alpha_3, \alpha_4$  are corresponding to constant coefficients. So, to verify (6.28) for all value of  $x$ , it requires that  $\alpha_3 = \alpha_1$  and  $\alpha_4 = \alpha_2$ .

At wall  $z = d$

$$\gamma_z \sin(k_y y) \left[ -\alpha_1 e^{-\gamma_z d} \cosh(\gamma_x x) - \alpha_2 e^{-\gamma_z d} \sinh(\gamma_x x) + \alpha_3 e^{+\gamma_z d} \cosh(\gamma_x x) + \alpha_4 e^{+\gamma_z d} \sinh(\gamma_x x) \right] = 0$$

$$(\alpha_3 e^{+\gamma_z d} - \alpha_1 e^{-\gamma_z d}) \cosh(\gamma_x x) + (\alpha_4 e^{+\gamma_z d} - \alpha_2 e^{-\gamma_z d}) \sinh(\gamma_x x) = 0$$

$$\alpha_3 (e^{+\gamma_z d} - e^{-\gamma_z d}) \cosh(\gamma_x x) + \alpha_4 (e^{+\gamma_z d} - e^{-\gamma_z d}) \sinh(\gamma_x x) = 0$$

$$\alpha_3 (2 \sinh(\gamma_z d)) \cosh(\gamma_x x) + \alpha_4 (2 \sinh(\gamma_z d)) \sinh(\gamma_x x) = 0$$

$$2 \sinh(\gamma_z d) \left[ \alpha_3 \cosh(\gamma_x x) + \alpha_4 \sinh(\gamma_x x) \right] = 0 \quad (6.29)$$

Knowing that  $\alpha_3$  and  $\alpha_4$  cannot be zero. So, for (6.29) to verify for all  $x$  value, it requires that  $\sinh(\gamma_z d) = 0$ .

If  $\gamma_z = \alpha$  (real value) corresponding to the attenuation constant, then it implies that  $\sinh(\alpha d) = 0$  or  $\alpha = 0$ .

If  $\gamma_z = jk_z$  (pure imaginary value) corresponding to the phase constant, then it implies  $\sinh(jk_z d) = j \sin(k_z d) = 0$  or  $k_z = p\pi / d$ .

Putting (6.27) in the boundary condition of  $H_z|_{z=0} = 0$ ,

$$\left[ \beta_1 \cosh(\gamma_x x) + \beta_2 \sinh(\gamma_x x) + \beta_3 \cosh(\gamma_x x) + \beta_4 \sinh(\gamma_x x) \right] \cos(k_y y) = 0$$

$$(\beta_1 + \beta_3) \cosh(\gamma_x x) + (\beta_2 + \beta_4) \sinh(\gamma_x x) = 0 \quad (6.30)$$

To verify (6.30) for all  $x$  value, it implies that  $\beta_3 = -\beta_1$  and  $\beta_4 = -\beta_2$ .

Then, after putting (6.27) in the boundary condition  $H_z|_{z=d} = 0$ ,

$$\left[ \beta_1 e^{-\gamma_z d} \cosh(\gamma_x x) + \beta_2 e^{-\gamma_z d} \sinh(\gamma_x x) + \beta_3 e^{+\gamma_z d} \cosh(\gamma_x x) + \beta_4 e^{+\gamma_z d} \sinh(\gamma_x x) \right] \cos(k_y y) = 0$$

$$(\beta_1 e^{-\gamma_z d} + \beta_3 e^{+\gamma_z d}) \cosh(\gamma_x x) + (\beta_2 e^{-\gamma_z d} + \beta_4 e^{+\gamma_z d}) \sinh(\gamma_x x) = 0$$

$$\beta_1 (e^{-\gamma_z d} - e^{+\gamma_z d}) \cosh(\gamma_x x) + \beta_2 (e^{-\gamma_z d} - e^{+\gamma_z d}) \sinh(\gamma_x x) = 0$$

$$-2 \sinh(\gamma_z d) [\beta_1 \cosh(\gamma_x x) + \beta_2 \sinh(\gamma_x x)] = 0 \quad (6.31)$$

So, to verify (6.31) for all  $x$  value, it is requires that  $\sinh(\gamma_z d) = 0$ . It leads to the same results as the previous analysis which shows that  $\gamma_z = \alpha = 0$  if it is a real value and  $\gamma_z = jk_z = jp\pi / d$  if it is a pure imaginary value.

Since  $\alpha_3 = \alpha_1$  and  $\alpha_4 = \alpha_2$ , the equation (6.26) can be rewritten as:

$$E_z = [\alpha_1 \cosh(\gamma_x x) + \alpha_2 \sinh(\gamma_x x)] e^{-\gamma_z z} \sin(k_y y) + [\alpha_1 \cosh(\gamma_x x) + \alpha_2 \sinh(\gamma_x x)] e^{+\gamma_z z} \sin(k_y y) \quad (6.32)$$

$$E_z = 2 \cosh(\gamma_z z) \sin(k_y y) [\alpha_1 \cosh(\gamma_x x) + \alpha_2 \sinh(\gamma_x x)] \quad (6.33)$$

Since  $\beta_3 = -\beta_1$  and  $\beta_4 = -\beta_2$ , the equation (6.27) can be rewritten as:

$$H_z = [\beta_1 \cosh(\gamma_x x) + \beta_2 \sinh(\gamma_x x)] e^{-\gamma_z z} \cos(k_y y) + [-\beta_1 \cosh(\gamma_x x) - \beta_2 \sinh(\gamma_x x)] e^{+\gamma_z z} \cos(k_y y) \quad (6.34)$$

$$H_z = -2 \sinh(\gamma_z z) \cos(k_y y) [\beta_1 \cosh(\gamma_x x) + \beta_2 \sinh(\gamma_x x)] \quad (6.35)$$

With the coefficients  $A_1, A_2, B_1, B_2$  as  $A_1 = 2\alpha_1$ ;  $A_2 = 2\alpha_2$ ;  $B_1 = 2\beta_1$ ;  $B_2 = 2\beta_2$ , the equations (6.33) and (6.35) become

$$E_z = [A_1 \cosh(\gamma_x x) + A_2 \sinh(\gamma_x x)] \sin(k_y y) \cosh(\gamma_z z) \quad (6.36)$$

$$H_z = [-B_1 \cosh(\gamma_x x) - B_2 \sinh(\gamma_x x)] \cos(k_y y) \sinh(\gamma_z z) \quad (6.37)$$

where  $A_1, A_2, B_1, B_2$  are constant complex coefficients of the longitudinal components.

According to (6.32) and (6.34), The electric and magnetic field can be expressed as the summation of the forward and the backward components as:

$$E_z = [\alpha_1 \cosh(\gamma_x x) + \alpha_2 \sinh(\gamma_x x)] e^{-\gamma_z z} \sin(k_y y) + [\alpha_1 \cosh(\gamma_x x) + \alpha_2 \sinh(\gamma_x x)] e^{+\gamma_z z} \sin(k_y y)$$

$$E_z = E_z^+ + E_z^-$$

where:

$$E_z^+ = [\alpha_1 \cosh(\gamma_x x) + \alpha_2 \sinh(\gamma_x x)] e^{-\gamma_z z} \sin(k_y y) \quad (6.38)$$

$$E_z^- = [\alpha_1 \cosh(\gamma_x x) + \alpha_2 \sinh(\gamma_x x)] e^{+\gamma_z z} \sin(k_y y) \quad (6.39)$$

And,

$$H_z = [\beta_1 \cosh(\gamma_x x) + \beta_2 \sinh(\gamma_x x)] e^{-\gamma_z z} \cos(k_y y) + [-\beta_1 \cosh(\gamma_x x) - \beta_2 \sinh(\gamma_x x)] e^{+\gamma_z z} \cos(k_y y)$$

$$H_z = H_z^+ + H_z^-$$

where:

$$H_z^+ = [\beta_1 \cosh(\gamma_x x) + \beta_2 \sinh(\gamma_x x)] e^{-\gamma_z z} \cos(k_y y) \quad (6.40)$$

$$H_z^- = [-\beta_1 \cosh(\gamma_x x) - \beta_2 \sinh(\gamma_x x)] e^{+\gamma_z z} \cos(k_y y) \quad (6.41)$$

## **6.2.2. Expression of the transverse components of the EM field**

To get the expression of the transverse components  $(\vec{E}_x, \vec{E}_y)$  and  $(\vec{H}_x, \vec{H}_y)$  of the EM field, the relations between those components and the longitudinal components  $E_z$  and  $H_z$  are required. It should be noticed that  $\vec{E}_T = \vec{E}_x + \vec{E}_y$  and  $\vec{H}_T = \vec{H}_x + \vec{H}_y$ .

### **6.2.2.1. Propagation in z direction:**

From **annex 6.1.1**, the relation of EM propagation in the forward direction is recalled in **(6.42)** and **(6.43)**

$$(\gamma_z^2 + k_0^2 \epsilon_r) \vec{E}_T = -\gamma_z (\nabla_T E_z) - j\omega\mu_0 (\nabla_T H_z) \times \vec{z} \quad (6.42)$$

$$(\gamma_z^2 + k_0^2 \epsilon_r) \vec{H}_T = j\omega\epsilon_0 \epsilon_r (\nabla_T E_z) \times \vec{z} - \gamma_z (\nabla_T H_z) \quad (6.43)$$

**The equation of  $E_y^+$  and  $H_y^+$**

From **(6.42)**,



$$(\gamma_z^2 + k_0^2 \epsilon_r) \vec{E}_T = -\gamma_z (\nabla_T E_z) - j\omega\mu_0 (\nabla_T H_z) \times \vec{z}$$

$$k_c^2 (\vec{E}_x + \vec{E}_y) = -\gamma_z (\nabla_T E_z) - j\omega\mu_0 (\nabla_T H_z) \times \vec{z}$$

where  $k_c^2 = \gamma_z^2 + k_0^2 \epsilon_r$

$$\nabla_T E_z = \begin{bmatrix} \frac{\partial E_z}{\partial x} \\ \frac{\partial E_z}{\partial y} \end{bmatrix} = \frac{\partial E_z}{\partial x} \vec{x} + \frac{\partial E_z}{\partial y} \vec{y}$$

$$\nabla_T H_z = \begin{bmatrix} \frac{\partial H_z}{\partial x} \\ \frac{\partial H_z}{\partial y} \end{bmatrix} = \frac{\partial H_z}{\partial x} \vec{x} + \frac{\partial H_z}{\partial y} \vec{y}$$

$$(\nabla_T H_z) \times \vec{z} = \begin{bmatrix} \frac{\partial H_z}{\partial x} \\ \frac{\partial H_z}{\partial y} \\ 0 \end{bmatrix} \wedge \begin{bmatrix} 0 \\ 0 \\ 1 \end{bmatrix} = \frac{\partial H_z}{\partial y} \vec{x} - \frac{\partial H_z}{\partial x} \vec{y}$$

So,

$$k_c^2 (\vec{E}_x + \vec{E}_y) = -\gamma_z \left( \frac{\partial E_z}{\partial x} \vec{x} + \frac{\partial E_z}{\partial y} \vec{y} \right) - j\omega\mu_0 \left( \frac{\partial H_z}{\partial y} \vec{x} - \frac{\partial H_z}{\partial x} \vec{y} \right)$$

$$k_c^2 \vec{E}_x + k_c^2 \vec{E}_y = \left( -\gamma_z \frac{\partial E_z}{\partial x} - j\omega\mu_0 \frac{\partial H_z}{\partial y} \right) \vec{x} + \left( -\gamma_z \frac{\partial E_z}{\partial y} + j\omega\mu_0 \frac{\partial H_z}{\partial x} \right) \vec{y}$$

Then,

$$E_y^+ = \frac{1}{k_c^2} \left[ -\gamma_z \frac{\partial E_z^+}{\partial y} + j\omega\mu_0 \frac{\partial H_z^+}{\partial x} \right] \quad (6.44)$$

From (6.43), the same procedure is applied:

$$k_c^2 \vec{H}_T = j\omega\epsilon_0 \epsilon_r (\nabla_T E_z) \times \vec{z} - \gamma_z (\nabla_T H_z)$$

$$k_c^2(H_x + H_y) = j\omega\varepsilon_0\varepsilon_r(\nabla_T E_z) \times \vec{z} - \gamma_z(\nabla_T H_z)$$

$$\text{with, } (\nabla_T E_z) \times \vec{z} = \begin{bmatrix} \frac{\partial E_z}{\partial x} \\ \frac{\partial E_z}{\partial y} \\ 0 \end{bmatrix} \wedge \begin{bmatrix} 0 \\ 0 \\ 1 \end{bmatrix} = \frac{\partial E_z}{\partial y} \vec{x} - \frac{\partial E_z}{\partial x} \vec{y}$$

It leads to:

$$k_c^2(\vec{H}_x + \vec{H}_y) = j\omega\varepsilon_0\varepsilon_r \left( \frac{\partial E_z}{\partial y} \vec{x} - \frac{\partial E_z}{\partial x} \vec{y} \right) - \gamma_z \left( \frac{\partial H_z}{\partial x} \vec{x} + \frac{\partial H_z}{\partial y} \vec{y} \right)$$

$$k_c^2 \vec{H}_x + k_c^2 \vec{H}_y = \left( j\omega\varepsilon_0\varepsilon_r \frac{\partial E_z}{\partial y} - \gamma_z \frac{\partial H_z}{\partial x} \right) \vec{x} + \left( -j\omega\varepsilon_0\varepsilon_r \frac{\partial E_z}{\partial x} - \gamma_z \frac{\partial H_z}{\partial y} \right) \vec{y}$$

$$H_y^+ = \frac{1}{k_c^2} \left[ -j\omega\varepsilon_0 \frac{\partial E_z^+}{\partial x} - \gamma_z \frac{\partial H_z^+}{\partial y} \right] \quad (6.45)$$

### 6.2.2.2. Propagation in - z direction:

In annex A.2, the relation of EM propagation in the backward direction is recalled in (6.46) and (6.47)

$$(\gamma_z^2 + k_0^2 \varepsilon_r) \vec{E}_T = \gamma_z (\nabla_T E_z) - j\omega\mu_0 (\nabla_T H_z) \times \vec{z} \quad (6.46)$$

$$(\gamma_z^2 + k_0^2 \varepsilon_r) \vec{H}_T = j\omega\varepsilon_0\varepsilon_r (\nabla_T E_z) \times \vec{z} + \gamma_z (\nabla_T H_z) \quad (6.47)$$

**The equation of  $E_y^-$  and  $H_y^-$**

From (6.46),

$$(\gamma_z^2 + k_0^2 \varepsilon_r) \vec{E}_T = \gamma_z (\nabla_T E_z) - j\omega\mu_0 (\nabla_T H_z) \times \vec{z}$$

$$k_c^2 (\vec{E}_x + \vec{E}_y) = \gamma_z (\nabla_T E_z) - j\omega\mu_0 (\nabla_T H_z) \times \vec{z}$$

where  $k_c^2 = \gamma_z^2 + k_0^2 \varepsilon_r$

$$\nabla_T E_z = \begin{bmatrix} \frac{\partial E_z}{\partial x} \\ \frac{\partial E_z}{\partial y} \end{bmatrix} = \frac{\partial E_z}{\partial x} \vec{x} + \frac{\partial E_z}{\partial y} \vec{y}$$

$$\nabla_T H_z = \begin{bmatrix} \frac{\partial H_z}{\partial x} \\ \frac{\partial H_z}{\partial y} \end{bmatrix} = \frac{\partial H_z}{\partial x} \vec{x} + \frac{\partial H_z}{\partial y} \vec{y}$$

$$(\nabla_T H_z) \times \vec{z} = \begin{bmatrix} \frac{\partial H_z}{\partial x} \\ \frac{\partial H_z}{\partial y} \\ 0 \end{bmatrix} \wedge \begin{bmatrix} 0 \\ 0 \\ 1 \end{bmatrix} = \frac{\partial H_z}{\partial y} \vec{x} - \frac{\partial H_z}{\partial x} \vec{y}$$

So,

$$k_c^2 (\vec{E}_x + \vec{E}_y) = \gamma_z \left( \frac{\partial E_z}{\partial x} \vec{x} + \frac{\partial E_z}{\partial y} \vec{y} \right) - j\omega\mu_0 \left( \frac{\partial H_z}{\partial y} \vec{x} - \frac{\partial H_z}{\partial x} \vec{y} \right)$$

$$k_c^2 \vec{E}_x + k_c^2 \vec{E}_y = \left( \gamma_z \frac{\partial E_z}{\partial x} - j\omega\mu_0 \frac{\partial H_z}{\partial y} \right) \vec{x} + \left( \gamma_z \frac{\partial E_z}{\partial y} + j\omega\mu_0 \frac{\partial H_z}{\partial x} \right) \vec{y}$$

Hence,

$$E_y^- = \frac{1}{k_c^2} \left[ \gamma_z \frac{\partial E_z^-}{\partial y} + j\omega\mu_0 \frac{\partial H_z^-}{\partial x} \right] \quad (6.48)$$

From (6.47), the same procedure is applied:

$$k_c^2 \vec{H}_T = j\omega\epsilon_0\epsilon_r (\nabla_T E_z) \times \vec{z} + \gamma_z (\nabla_T H_z)$$

$$k_c^2 (H_x + H_y) = j\omega\epsilon_0\epsilon_r (\nabla_T E_z) \times \vec{z} + \gamma_z (\nabla_T H_z)$$

$$\text{with, } (\nabla_T E_z) \times \vec{z} = \begin{bmatrix} \frac{\partial E_z}{\partial x} \\ \frac{\partial E_z}{\partial y} \\ 0 \end{bmatrix} \wedge \begin{bmatrix} 0 \\ 0 \\ 1 \end{bmatrix} = \frac{\partial E_z}{\partial y} \vec{x} - \frac{\partial E_z}{\partial x} \vec{y}$$

It leads to:

$$k_c^2 (\vec{H}_x + \vec{H}_y) = j\omega\epsilon_0\epsilon_r \left( \frac{\partial E_z}{\partial y} \vec{x} - \frac{\partial E_z}{\partial x} \vec{y} \right) + \gamma_z \left( \frac{\partial H_z}{\partial x} \vec{x} + \frac{\partial H_z}{\partial y} \vec{y} \right)$$

$$k_c^2 \vec{H}_x + k_c^2 \vec{H}_y = \left( j\omega\epsilon_0\epsilon_r \frac{\partial E_z}{\partial y} + \gamma_z \frac{\partial H_z}{\partial x} \right) \vec{x} + \left( -j\omega\epsilon_0\epsilon_r \frac{\partial E_z}{\partial x} + \gamma_z \frac{\partial H_z}{\partial y} \right) \vec{y}$$

Hence,

$$H_y^- = \frac{1}{k_c^2} \left[ -j\omega\epsilon_0 \frac{\partial E_z^-}{\partial x} + \gamma_z \frac{\partial H_z^-}{\partial y} \right] \quad (6.49)$$

**The expression of  $E_y$**

Derive (6.38) with  $\partial y$ , we got:

$$\frac{\partial E_z^+}{\partial y} = \frac{\partial}{\partial y} \left\{ \left[ \alpha_1 \cosh(\gamma_x x) + \alpha_2 \sinh(\gamma_x x) \right] e^{-\gamma_z z} \sin(k_y y) \right\}$$

$$\frac{\partial E_z^+}{\partial y} = \left[ \alpha_1 \cosh(\gamma_x x) + \alpha_2 \sinh(\gamma_x x) \right] e^{-\gamma_z z} k_y \cos(k_y y) \quad (6.50)$$

Derive (6.40) with  $\partial x$

$$\frac{\partial H_z^+}{\partial x} = \frac{\partial}{\partial x} \left\{ \left[ \beta_1 \cosh(\gamma_x x) + \beta_2 \sinh(\gamma_x x) \right] e^{-\gamma_z z} \cos(k_y y) \right\}$$

$$\frac{\partial H_z^+}{\partial x} = \gamma_x \left[ \beta_1 \sinh(\gamma_x x) + \beta_2 \cosh(\gamma_x x) \right] e^{-\gamma_z z} \cos(k_y y) \quad (6.51)$$

By putting (6.50) and (6.51) into (6.44)

$$\begin{aligned}
E_y^+ &= \frac{1}{k_c^2} \left[ -\gamma_z \frac{\partial E_z^+}{\partial y} + j\omega\mu_0 \frac{\partial H_z^+}{\partial x} \right] \\
E_y^+ &= \frac{1}{k_c^2} [-\gamma_z [\alpha_1 \cosh(\gamma_x x) + \alpha_2 \sinh(\gamma_x x)] e^{-\gamma_z z} k_y \cos(k_y y) \\
&\quad + j\omega\mu_0 \gamma_x [\beta_1 \sinh(\gamma_x x) + \beta_2 \cosh(\gamma_x x)] e^{-\gamma_z z} \cos(k_y y)] \\
E_y^+ &= \frac{e^{-\gamma_z z} \cos(k_y y)}{k_c^2} [-\gamma_z k_y \cosh(\gamma_x x) \alpha_1 - \gamma_z k_y \sinh(\gamma_x x) \alpha_2 \\
&\quad + j\omega\mu_0 \gamma_x \sinh(\gamma_x x) \beta_1 + j\omega\mu_0 \gamma_x \cosh(\gamma_x x) \beta_2] \tag{6.52}
\end{aligned}$$

Derive (6.39) with  $\partial y$ , we got:

$$\begin{aligned}
\frac{\partial E_z^-}{\partial y} &= \frac{\partial}{\partial y} \left\{ [\alpha_1 \cosh(\gamma_x x) + \alpha_2 \sinh(\gamma_x x)] e^{+\gamma_z z} \sin(k_y y) \right\} \\
\frac{\partial E_z^-}{\partial y} &= [\alpha_1 \cosh(\gamma_x x) + \alpha_2 \sinh(\gamma_x x)] e^{+\gamma_z z} k_y \cos(k_y y) \tag{6.53}
\end{aligned}$$

Derive (6.41) with  $\partial x$

$$\begin{aligned}
\frac{\partial H_z^-}{\partial x} &= \frac{\partial}{\partial x} \left\{ [-\beta_1 \cosh(\gamma_x x) - \beta_2 \sinh(\gamma_x x)] e^{+\gamma_z z} \cos(k_y y) \right\} \\
\frac{\partial H_z^-}{\partial x} &= \gamma_x [-\beta_1 \sinh(\gamma_x x) - \beta_2 \cosh(\gamma_x x)] e^{+\gamma_z z} \cos(k_y y) \tag{6.54}
\end{aligned}$$

By putting (6.53) and (6.54) into (6.48)

$$\begin{aligned}
E_y^- &= \frac{1}{k_c^2} \left[ \gamma_z \frac{\partial E_z^-}{\partial y} + j\omega\mu_0 \frac{\partial H_z^-}{\partial x} \right] \\
E_y^- &= \frac{1}{k_c^2} [\gamma_z [\alpha_1 \cosh(\gamma_x x) + \alpha_2 \sinh(\gamma_x x)] e^{+\gamma_z z} k_y \cos(k_y y) \\
&\quad + j\omega\mu_0 \gamma_x [-\beta_1 \sinh(\gamma_x x) - \beta_2 \cosh(\gamma_x x)] e^{+\gamma_z z} \cos(k_y y)]
\end{aligned}$$

$$E_y^- = \frac{e^{+\gamma_z z} \cos(k_y y)}{k_c^2} [\gamma_z k_y \cosh(\gamma_x x) \alpha_1 + \gamma_z k_y \sinh(\gamma_x x) \alpha_2 - j\omega\mu_0\gamma_x \sinh(\gamma_x x) \beta_1 - j\omega\mu_0\gamma_x \cosh(\gamma_x x) \beta_2] \quad (6.55)$$

Summation of (6.52) and (6.55) lead to:

$$E_y = E_y^+ + E_y^-$$

$$E_y = \frac{e^{-\gamma_z z} \cos(k_y y)}{k_c^2} [-\gamma_z k_y \cosh(\gamma_x x) \alpha_1 - \gamma_z k_y \sinh(\gamma_x x) \alpha_2 + j\omega\mu_0\gamma_x \sinh(\gamma_x x) \beta_1 + j\omega\mu_0\gamma_x \cosh(\gamma_x x) \beta_2] + \frac{e^{+\gamma_z z} \cos(k_y y)}{k_c^2} [\gamma_z k_y \cosh(\gamma_x x) \alpha_1 + \gamma_z k_y \sinh(\gamma_x x) \alpha_2 - j\omega\mu_0\gamma_x \sinh(\gamma_x x) \beta_1 - j\omega\mu_0\gamma_x \cosh(\gamma_x x) \beta_2]$$

$$E_y = \frac{\cos(k_y y)}{k_c^2} [(e^{+\gamma_z z} - e^{-\gamma_z z}) \gamma_z k_y \cosh(\gamma_x x) \alpha_1 + (e^{+\gamma_z z} - e^{-\gamma_z z}) \gamma_z k_y \sinh(\gamma_x x) \alpha_2 - (e^{+\gamma_z z} - e^{-\gamma_z z}) j\omega\mu_0\gamma_x \sinh(\gamma_x x) \beta_1 - (e^{+\gamma_z z} - e^{-\gamma_z z}) j\omega\mu_0\gamma_x \cosh(\gamma_x x) \beta_2]$$

$$E_y = \frac{\cos(k_y y)}{k_c^2} [\gamma_z k_y \cosh(\gamma_x x) (2 \sinh(\gamma_z z)) \alpha_1 + \gamma_z k_y \sinh(\gamma_x x) (2 \sinh(\gamma_z z)) \alpha_2 - j\omega\mu_0\gamma_x \sinh(\gamma_x x) (2 \sinh(\gamma_z z)) \beta_1 - j\omega\mu_0\gamma_x \cosh(\gamma_x x) (2 \sinh(\gamma_z z)) \beta_2]$$

$$E_y = \frac{\cos(k_y y) \sinh(\gamma_z z)}{k_c^2} [\gamma_z k_y \cosh(\gamma_x x) 2\alpha_1 + \gamma_z k_y \sinh(\gamma_x x) 2\alpha_2 - j\omega\mu_0\gamma_x \sinh(\gamma_x x) 2\beta_1 - j\omega\mu_0\gamma_x \cosh(\gamma_x x) 2\beta_2]$$

$$E_y = \frac{\cos(k_y y) \sinh(\gamma_z z)}{k_c^2} [\gamma_z k_y \cosh(\gamma_x x) A_1 + \gamma_z k_y \sinh(\gamma_x x) A_2 - j\omega\mu_0\gamma_x \sinh(\gamma_x x) B_1 - j\omega\mu_0\gamma_x \cosh(\gamma_x x) B_2] \quad (6.56)$$

**The expression of  $H_y$**

Derive (6.38) with  $\partial x$ , we got:

$$\frac{\partial E_z^+}{\partial x} = \frac{\partial}{\partial x} \left\{ [\alpha_1 \cosh(\gamma_x x) + \alpha_2 \sinh(\gamma_x x)] e^{-\gamma_z z} \sin(k_y y) \right\}$$

$$\frac{\partial E_z^+}{\partial x} = \gamma_x [\alpha_1 \sinh(\gamma_x x) + \alpha_2 \cosh(\gamma_x x)] e^{-\gamma_z z} \sin(k_y y) \quad (6.57)$$

Derive (3.22) with  $\partial y$ , we got:

$$\begin{aligned} \frac{\partial H_z^+}{\partial y} &= \frac{\partial}{\partial y} \{ [\beta_1 \cosh(\gamma_x x) + \beta_2 \sinh(\gamma_x x)] e^{-\gamma_z z} \cos(k_y y) \} \\ \frac{\partial H_z^+}{\partial y} &= -k_y [\beta_1 \cosh(\gamma_x x) + \beta_2 \sinh(\gamma_x x)] e^{-\gamma_z z} \sin(k_y y) \end{aligned} \quad (6.58)$$

By putting (6.57) and (6.58) into (6.45),

$$\begin{aligned} H_y^+ &= \frac{1}{k_c^2} \{ -j\omega\epsilon_0 \gamma_x [\alpha_1 \sinh(\gamma_x x) + \alpha_2 \cosh(\gamma_x x)] e^{-\gamma_z z} \sin(k_y y) \\ &\quad + \gamma_z k_y [\beta_1 \cosh(\gamma_x x) + \beta_2 \sinh(\gamma_x x)] e^{-\gamma_z z} \sin(k_y y) \} \\ H_y^+ &= \frac{e^{-\gamma_z z} \sin(k_y y)}{k_c^2} [-j\omega\epsilon_0 \gamma_x \sinh(\gamma_x x) \alpha_1 - j\omega\epsilon_0 \gamma_x \cosh(\gamma_x x) \alpha_2 \\ &\quad + \gamma_z k_y \cosh(\gamma_x x) \beta_1 + \gamma_z k_y \sinh(\gamma_x x) \beta_2] \end{aligned} \quad (6.59)$$

Derive (6.39) with  $\partial x$ ,

$$\begin{aligned} \frac{\partial E_z^-}{\partial x} &= \frac{\partial}{\partial x} \{ [\alpha_1 \cosh(\gamma_x x) + \alpha_2 \sinh(\gamma_x x)] e^{+\gamma_z z} \sin(k_y y) \} \\ \frac{\partial E_z^-}{\partial x} &= \gamma_x [\alpha_1 \sinh(\gamma_x x) + \alpha_2 \cosh(\gamma_x x)] e^{+\gamma_z z} \sin(k_y y) \end{aligned} \quad (6.60)$$

Derive (6.41) with  $\partial y$  lead to:

$$\begin{aligned} \frac{\partial H_z^-}{\partial y} &= \frac{\partial}{\partial y} \{ [-\beta_1 \cosh(\gamma_x x) - \beta_2 \sinh(\gamma_x x)] e^{+\gamma_z z} \cos(k_y y) \} \\ \frac{\partial H_z^-}{\partial y} &= -k_y [-\beta_1 \cosh(\gamma_x x) - \beta_2 \sinh(\gamma_x x)] e^{+\gamma_z z} \sin(k_y y) \\ \frac{\partial H_z^-}{\partial y} &= k_y [\beta_1 \cosh(\gamma_x x) + \beta_2 \sinh(\gamma_x x)] e^{-\gamma_z z} \sin(k_y y) \end{aligned} \quad (6.61)$$

By putting (6.61) and (6.62) into (6.49)

$$\begin{aligned}
H_y^- &= \frac{1}{k_c^2} \{ -j\omega\varepsilon_0\gamma_x [\alpha_1 \sinh(\gamma_x x) + \alpha_2 \cosh(\gamma_x x)] e^{+\gamma_z z} \sin(k_y y) \\
&\quad + \gamma_z k_y [\beta_1 \cosh(\gamma_x x) + \beta_2 \sinh(\gamma_x x)] e^{-\gamma_z z} \sin(k_y y) \} \\
H_y^- &= \frac{e^{+\gamma_z z} \sin(k_y y)}{k_c^2} [-j\omega\varepsilon_0\gamma_x \sinh(\gamma_x x)\alpha_1 - j\omega\varepsilon_0\gamma_x \cosh(\gamma_x x)\alpha_2 \\
&\quad + \gamma_z k_y \cosh(\gamma_x x)\beta_1 + \gamma_z k_y \sinh(\gamma_x x)\beta_2] \tag{6.62}
\end{aligned}$$

Summation of (6.60) and (6.63) give the expression of  $H_y$

$$\begin{aligned}
H_y &= H_y^+ + H_y^- \\
H_y &= \frac{e^{-\gamma_z z} \sin(k_y y)}{k_c^2} [-j\omega\varepsilon_0\gamma_x \sinh(\gamma_x x)\alpha_1 - j\omega\varepsilon_0\gamma_x \cosh(\gamma_x x)\alpha_2 + \gamma_z k_y \cosh(\gamma_x x)\beta_1 + \gamma_z k_y \sinh(\gamma_x x)\beta_2] \\
&\quad + \frac{e^{+\gamma_z z} \sin(k_y y)}{k_c^2} [-j\omega\varepsilon_0\gamma_x \sinh(\gamma_x x)\alpha_1 - j\omega\varepsilon_0\gamma_x \cosh(\gamma_x x)\alpha_2 + \gamma_z k_y \cosh(\gamma_x x)\beta_1 + \gamma_z k_y \sinh(\gamma_x x)\beta_2] \\
H_y &= \frac{\sin(k_y y)}{k_c^2} [-(e^{-\gamma_z z} + e^{+\gamma_z z}) j\omega\varepsilon_0\gamma_x \sinh(\gamma_x x)\alpha_1 - (e^{-\gamma_z z} + e^{+\gamma_z z}) j\omega\varepsilon_0\gamma_x \cosh(\gamma_x x)\alpha_2 \\
&\quad + (e^{-\gamma_z z} + e^{+\gamma_z z}) \gamma_z k_y \cosh(\gamma_x x)\beta_1 + (e^{-\gamma_z z} + e^{+\gamma_z z}) \gamma_z k_y \sinh(\gamma_x x)\beta_2] \\
H_y &= \frac{\sin(k_y y)}{k_c^2} [-(2 \cosh(\gamma_z z)) j\omega\varepsilon_0\gamma_x \sinh(\gamma_x x)\alpha_1 - (2 \cosh(\gamma_z z)) j\omega\varepsilon_0\gamma_x \cosh(\gamma_x x)\alpha_2 \\
&\quad + (2 \cosh(\gamma_z z)) \gamma_z k_y \cosh(\gamma_x x)\beta_1 + (2 \cosh(\gamma_z z)) \gamma_z k_y \sinh(\gamma_x x)\beta_2] \\
H_y &= \frac{\sin(k_y y) \cosh(\gamma_z z)}{k_c^2} [-j\omega\varepsilon_0\gamma_x \sinh(\gamma_x x) 2\alpha_1 - j\omega\varepsilon_0\gamma_x \cosh(\gamma_x x) 2\alpha_2 \\
&\quad + \gamma_z k_y \cosh(\gamma_x x) 2\beta_1 + \gamma_z k_y \sinh(\gamma_x x) 2\beta_2] \\
H_y &= \frac{\sin(k_y y) \cosh(\gamma_z z)}{k_c^2} [-j\omega\varepsilon_0\gamma_x \sinh(\gamma_x x) A_1 - j\omega\varepsilon_0\gamma_x \cosh(\gamma_x x) A_2 \\
&\quad + \gamma_z k_y \cosh(\gamma_x x) B_1 + \gamma_z k_y \sinh(\gamma_x x) B_2] \tag{6.63}
\end{aligned}$$



### 6.2.3. Surface impedance boundary conditions

Suppose that the tangential and the longitudinal components of the anisotropic impedance at  $x = 0$  are  $(Z_{t1}; Z_{z1})$  and at  $x = a$  are  $(Z_{t2}; Z_{z2})$ . The boundary conditions at the anisotropic walls of the chamber can be recalled as in (6.65) to (6.68)

$$\left. \frac{E_y}{H_z} \right|_{x=0} = -Z_{t1} \quad (6.64)$$

$$\left. \frac{E_y}{H_z} \right|_{x=a} = Z_{t2} \quad (6.65)$$

$$\left. \frac{E_z}{H_y} \right|_{x=0} = Z_{z1} \quad (6.66)$$

$$\left. \frac{E_z}{H_y} \right|_{x=a} = -Z_{z2} \quad (6.67)$$

### 6.2.4. System of linear equation

From the boundary condition (6.64),  $\left. \frac{E_y}{H_z} \right|_{x=0} = -Z_{t1}$ , we got

$$E_y \Big|_{x=0} + Z_{t1} \cdot H_z \Big|_{x=0} = 0$$

From (6.56),

$$E_y = \frac{\cos(k_y y) \sinh(\gamma_z z)}{k_c^2} [\gamma_z k_y \cosh(\gamma_x x) A_1 + \gamma_z k_y \sinh(\gamma_x x) A_2 - j\omega\mu_0 \gamma_x \sinh(\gamma_x x) B_1 - j\omega\mu_0 \gamma_x \cosh(\gamma_x x) B_2]$$

$$E_y \Big|_{x=0} = \frac{\cos(k_y y) \sinh(\gamma_z z)}{k_c^2} [\gamma_z k_y A_1 + 0A_2 - 0B_1 - j\omega\mu_0 \gamma_x B_2]$$

From (6.37),

$$H_z = [-B_1 \cosh(\gamma_x x) - B_2 \sinh(\gamma_x x)] \cos(k_y y) \sinh(\gamma_z z)$$

$$H_z|_{x=0} = [-B_1 - 0B_2] \cos(k_y y) \sinh(\gamma_z z)$$

So,

$$\frac{\cos(k_y y) \sinh(\gamma_z z)}{k_c^2} [\gamma_z k_y A_1 + 0A_2 - 0B_1 - j\omega\mu_0\gamma_x B_2] + Z_{t1} [-B_1 - 0B_2] \cos(k_y y) \sinh(\gamma_z z) = 0$$

$$[\gamma_z k_y A_1 + 0A_2 - 0B_1 - j\omega\mu_0\gamma_x B_2] + Z_{t1} k_c^2 [-B_1 - 0B_2] = 0$$

$$(\gamma_z k_y) A_1 + (0) A_2 + (-Z_{t1} k_c^2) B_1 + (-j\omega\mu_0\gamma_x) B_2 = 0 \quad (6.68)$$

From the boundary condition (6.65),  $\frac{E_y}{H_z}|_{x=a} = Z_{t2}$ , we got

$$E_y|_{x=a} - Z_{t2} \cdot H_z|_{x=a}$$

with,

$$E_y|_{x=a} = \frac{\cos(k_y y) \sinh(\gamma_z z)}{k_c^2} [\gamma_z k_y \cosh(\gamma_x a) A_1 + \gamma_z k_y \sinh(\gamma_x a) A_2 - j\omega\mu_0\gamma_x \sinh(\gamma_x a) B_1 - j\omega\mu_0\gamma_x \cosh(\gamma_x a) B_2]$$

$$H_z|_{x=a} = [-B_1 \cosh(\gamma_x a) - B_2 \sinh(\gamma_x a)] \cos(k_y y) \sinh(\gamma_z z)$$

Then,

$$\frac{1}{k_c^2} [\gamma_z k_y \cosh(\gamma_x a) A_1 + \gamma_z k_y \sinh(\gamma_x a) A_2 - j\omega\mu_0\gamma_x \sinh(\gamma_x a) B_1 - j\omega\mu_0\gamma_x \cosh(\gamma_x a) B_2] - Z_{t2} [-B_1 \cosh(\gamma_x a) - B_2 \sinh(\gamma_x a)] = 0$$

$$[\gamma_z k_y \cosh(\gamma_x a) A_1 + \gamma_z k_y \sinh(\gamma_x a) A_2 - j\omega\mu_0\gamma_x \sinh(\gamma_x a) B_1 - j\omega\mu_0\gamma_x \cosh(\gamma_x a) B_2] + Z_{t2} k_c^2 [B_1 \cosh(\gamma_x a) + B_2 \sinh(\gamma_x a)] = 0$$

$$\gamma_z k_y \cosh(\gamma_x a) A_1 + \gamma_z k_y \sinh(\gamma_x a) A_2 - j\omega\mu_0\gamma_x \sinh(\gamma_x a) B_1 - j\omega\mu_0\gamma_x \cosh(\gamma_x a) B_2 + Z_{t2} k_c^2 \cosh(\gamma_x a) B_1 + Z_{t2} k_c^2 \sinh(\gamma_x a) B_2 = 0$$

$$[\gamma_z k_y \cosh(\gamma_x a)]A_1 + [\gamma_z k_y \sinh(\gamma_x a)]A_2 + [-j\omega\mu_0\gamma_x \sinh(\gamma_x a) + Z_{t2}k_c^2 \cosh(\gamma_x a)]B_1 + [-j\omega\mu_0\gamma_x \cosh(\gamma_x a) + Z_{t2}k_c^2 \sinh(\gamma_x a)]B_2 = 0 \quad (6.69)$$

From the boundary condition (6.66),  $\frac{E_z}{H_y}\Big|_{x=0} = Z_{z1}$ , we got

$$E_z\Big|_{x=0} - Z_{z1} \cdot H_y\Big|_{x=0} = 0$$

with (6.36),  $E_z = [A_1 \cosh(\gamma_x x) + A_2 \sinh(\gamma_x x)] \sin(k_y y) \cosh(\gamma_z z)$

$$E_z\Big|_{x=0} = [A_1 + 0A_2] \sin(k_y y) \cosh(\gamma_z z)$$

with (6.64),

$$H_y = \frac{\sin(k_y y) \cosh(\gamma_z z)}{k_c^2} [-j\omega\varepsilon_0\gamma_x \sinh(\gamma_x x) A_1 - j\omega\varepsilon_0\gamma_x \cosh(\gamma_x x) A_2 + \gamma_z k_y \cosh(\gamma_x x) B_1 + \gamma_z k_y \sinh(\gamma_x x) B_2]$$

$$H_y\Big|_{x=0} = \frac{\sin(k_y y) \cosh(\gamma_z z)}{k_c^2} [0A_1 - j\omega\varepsilon_0\gamma_x A_2 + \gamma_z k_y B_1 + 0B_2]$$

So,

$$[A_1 + 0A_2] \sin(k_y y) \cosh(\gamma_z z) - Z_{z1} \frac{\sin(k_y y) \cosh(\gamma_z z)}{k_c^2} [0A_1 - j\omega\varepsilon_0\gamma_x A_2 + \gamma_z k_y B_1 + 0B_2] = 0$$

$$k_c^2 [A_1 + 0A_2] - Z_{z1} [0A_1 - j\omega\varepsilon_0\gamma_x A_2 + \gamma_z k_y B_1 + 0B_2] = 0$$

$$(k_c^2)A_1 + (Z_{z1} j\omega\varepsilon_0\gamma_x)A_2 + (-Z_{z1}\gamma_z k_y)B_1 + (0)B_2 = 0 \quad (6.70)$$

From boundary condition (6.67),  $\frac{E_z}{H_y}\Big|_{x=a} = -Z_{z2}$ , we got

$$E_z\Big|_{x=a} + Z_{z2} \cdot H_y\Big|_{x=a} = 0$$

with,

$$E_z|_{x=a} = [A_1 \cosh(\gamma_x a) + A_2 \sinh(\gamma_x a)] \sin(k_y y) \cosh(\gamma_z z)$$

$$H_y|_{x=a} = \frac{\sin(k_y y) \cosh(\gamma_z z)}{k_c^2} [-j\omega \varepsilon_0 \gamma_x \sinh(\gamma_x a) A_1 - j\omega \varepsilon_0 \gamma_x \cosh(\gamma_x a) A_2 \\ + \gamma_z k_y \cosh(\gamma_x a) B_1 + \gamma_z k_y \sinh(\gamma_x a) B_2]$$

Then,

$$[A_1 \cosh(\gamma_x a) + A_2 \sinh(\gamma_x a)] \sin(k_y y) \cosh(\gamma_z z) + Z_{z2} \frac{\sin(k_y y) \cosh(\gamma_z z)}{k_c^2} [-j\omega \varepsilon_0 \gamma_x \sinh(\gamma_x a) A_1 \\ - j\omega \varepsilon_0 \gamma_x \cosh(\gamma_x a) A_2 + \gamma_z k_y \cosh(\gamma_x a) B_1 + \gamma_z k_y \sinh(\gamma_x a) B_2] = 0$$

$$k_c^2 [A_1 \cosh(\gamma_x a) + A_2 \sinh(\gamma_x a)] + Z_{z2} [-j\omega \varepsilon_0 \gamma_x \sinh(\gamma_x a) A_1 - j\omega \varepsilon_0 \gamma_x \cosh(\gamma_x a) A_2 \\ + \gamma_z k_y \cosh(\gamma_x a) B_1 + \gamma_z k_y \sinh(\gamma_x a) B_2] = 0$$

$$(k_c^2 \cosh(\gamma_x a) - Z_{z2} j\omega \varepsilon_0 \gamma_x \sinh(\gamma_x a)) A_1 + (k_c^2 \sinh(\gamma_x a) - Z_{z2} j\omega \varepsilon_0 \gamma_x \cosh(\gamma_x a)) A_2 \\ + (Z_{z2} \gamma_z k_y \cosh(\gamma_x a)) + (Z_{z2} \gamma_z k_y \sinh(\gamma_x a)) B_2 = 0 \quad (6.71)$$

By combining (6.68), (6.69), (6.70) and (6.71), we got the system of linear equations,

$$\begin{bmatrix} \gamma_z k_y & 0 & -Z_{z1} k_c^2 & -j\omega \mu_0 \gamma_x \\ \gamma_z k_y \cosh(\gamma_x a) & \gamma_z k_y \sinh(\gamma_x a) & -j\omega \mu_0 \gamma_x \sinh(\gamma_x a) + Z_{z2} k_c^2 \cosh(\gamma_x a) & -j\omega \mu_0 \gamma_x \cosh(\gamma_x a) + Z_{z2} k_c^2 \sinh(\gamma_x a) \\ k_c^2 & Z_{z1} j\omega \varepsilon_0 \gamma_x & -Z_{z1} \gamma_z k_y & 0 \\ k_c^2 \cosh(\gamma_x a) - Z_{z2} j\omega \varepsilon_0 \gamma_x \sinh(\gamma_x a) & k_c^2 \sinh(\gamma_x a) - Z_{z2} j\omega \varepsilon_0 \gamma_x \cosh(\gamma_x a) & Z_{z2} \gamma_z k_y \cosh(\gamma_x a) & Z_{z2} \gamma_z k_y \sinh(\gamma_x a) \end{bmatrix} \times \begin{bmatrix} A_1 \\ A_2 \\ B_1 \\ B_2 \end{bmatrix} = \begin{bmatrix} 0 \\ 0 \\ 0 \\ 0 \end{bmatrix}$$

It can be written

$$\begin{bmatrix} M_{11} & M_{12} & M_{13} & M_{14} \\ M_{21} & M_{22} & M_{23} & M_{24} \\ M_{31} & M_{32} & M_{33} & M_{34} \\ M_{41} & M_{42} & M_{43} & M_{44} \end{bmatrix} \times \begin{bmatrix} A_1 \\ A_2 \\ B_1 \\ B_2 \end{bmatrix} = \begin{bmatrix} 0 \\ 0 \\ 0 \\ 0 \end{bmatrix} \quad \text{or} \quad [M] \times [A] = \vec{0} \quad (6.72)$$

where:

$$[M] = \begin{bmatrix} M_{11} & M_{12} & M_{13} & M_{14} \\ M_{21} & M_{22} & M_{23} & M_{24} \\ M_{31} & M_{32} & M_{33} & M_{34} \\ M_{41} & M_{42} & M_{43} & M_{44} \end{bmatrix} \quad (6.73)$$

$$[A] = [A_1 \quad A_2 \quad B_1 \quad B_2]^T$$

with,

$$\begin{aligned} M_{11} &= \gamma_z k_y; \quad M_{12} = 0; \quad M_{13} = -Z_{t1} k_c^2; \quad M_{14} = -j\omega\mu_0\gamma_x; \quad M_{21} = \gamma_z k_y \cosh(\gamma_x a); \\ M_{22} &= \gamma_z k_y \sinh(\gamma_x a); \quad M_{23} = -j\omega\mu_0\gamma_x \sinh(\gamma_x a) + Z_{t2} k_c^2 \cosh(\gamma_x a); \\ M_{24} &= -j\omega\mu_0\gamma_x \cosh(\gamma_x a) + Z_{t2} k_c^2 \sinh(\gamma_x a); \\ M_{31} &= k_c^2; \quad M_{32} = Z_{z1} j\omega\varepsilon_0\gamma_x; \quad M_{33} = -Z_{z1} \gamma_z k_y; \quad M_{34} = 0; \\ M_{41} &= k_c^2 \cosh(\gamma_x a) - Z_{z2} j\omega\varepsilon_0\gamma_x \sinh(\gamma_x a); \quad M_{42} = k_c^2 \sinh(\gamma_x a) - Z_{z2} j\omega\varepsilon_0\gamma_x \cosh(\gamma_x a); \\ M_{43} &= Z_{z2} \gamma_z k_y \cosh(\gamma_x a); \quad M_{44} = Z_{z2} \gamma_z k_y \sinh(\gamma_x a) \end{aligned}$$

In order to get the value of  $\gamma_x$ , and then the resonant frequencies and the resonant modes, the condition with  $\det([M]) = 0$  needs to be calculated. From this condition, the value of  $\gamma_x$  will be found. Then the resonant frequency of each resonant mode is computed.

### **6.2.5. Special case with zero order modes**

#### **6.2.5.1. Case ( $n = 0$ & $p \neq 0$ )**

If  $n = 0$ , we got  $k_y = \frac{n\pi}{b} = 0$ . So,  $\sin(k_y y) = 0$  and  $\cos(k_y y) = 1$

From the expression of  $E_z$  in (6.36),  $E_z = [A_1 \cosh(\gamma_x x) + A_2 \sinh(\gamma_x x)] \sin(k_y y) \cosh(\gamma_z z) = 0$ .

In consequence, there is only one generator which is  $H_z$ . So, the resonant mode in this case is purely TE.

$$\text{From (6.44), } E_y^+ = \frac{1}{k_c^2} \left[ -\gamma_z \frac{\partial E_z^+}{\partial y} + j\omega\mu_0 \frac{\partial H_z^+}{\partial x} \right] = \frac{1}{k_c^2} \left[ j\omega\mu_0 \frac{\partial H_z^+}{\partial x} \right]$$

with,  $\frac{\partial H_z^+}{\partial x} = \gamma_x [\beta_1 \sinh(\gamma_x x) + \beta_2 \cosh(\gamma_x x)] e^{-\gamma_z z} \cos(k_y y)$  and  $\cos(k_y y) = 1$

$$E_y^+ = \frac{1}{k_c^2} \left[ j\omega\mu_0 \gamma_x \beta_1 \sinh(\gamma_x x) + j\omega\mu_0 \gamma_x \beta_2 \cosh(\gamma_x x) \right] e^{-\gamma_z z}$$

$$\text{From (6.46), } E_y^- = \frac{1}{k_c^2} \left[ \gamma_z \frac{\partial E_z^-}{\partial y} + j\omega\mu_0 \frac{\partial H_z^-}{\partial x} \right] = \frac{1}{k_c^2} \left[ j\omega\mu_0 \frac{\partial H_z^-}{\partial x} \right]$$

with,  $\frac{\partial H_z^-}{\partial x} = \gamma_x [-\beta_1 \sinh(\gamma_x x) - \beta_2 \cosh(\gamma_x x)] e^{+\gamma_z z} \cos(k_y y)$  and  $\cos(k_y y) = 1$

$$E_y^- = \frac{1}{k_c^2} [-j\omega\mu_0\gamma_x \sinh(\gamma_x x)\beta_1 - j\omega\mu_0\gamma_x \cosh(\gamma_x x)\beta_2] e^{+\gamma_z z}$$

$$\begin{aligned} E_y &= E_y^+ + E_y^- \\ &= \frac{e^{-\gamma_z z} - e^{+\gamma_z z}}{k_c^2} [j\omega\mu_0\gamma_x \sinh(\gamma_x x)\beta_1 + j\omega\mu_0\gamma_x \cosh(\gamma_x x)\beta_2] \end{aligned}$$

$$E_y = \frac{-2 \sinh(\gamma_z z)}{k_c^2} [j\omega\mu_0\gamma_x \sinh(\gamma_x x)\beta_1 + j\omega\mu_0\gamma_x \cosh(\gamma_x x)\beta_2]$$

$$E_y = \frac{-\sinh(\gamma_z z)}{k_c^2} [j\omega\mu_0\gamma_x \sinh(\gamma_x x)B_1 + j\omega\mu_0\gamma_x \cosh(\gamma_x x)B_2] \quad (6.74)$$

In this case of  $n = 0$ , the expression of  $H_y^+$  in (6.45) become:

$$H_y^+ = \frac{1}{k_c^2} \left[ -\gamma_z \frac{\partial H_z^+}{\partial y} \right]$$

$$\frac{\partial H_z^+}{\partial y} = -k_y [\beta_1 \cosh(\gamma_x x) + \beta_2 \sinh(\gamma_x x)] e^{-\gamma_z z} \sin(k_y y) = 0 \text{ for } n = 0$$

$$H_y^+ = 0$$

From (6.47) with  $n = 0$ , the expression of  $H_y^-$  become:

$$H_y^- = \frac{1}{k_c^2} \left[ \gamma_z \frac{\partial H_z^-}{\partial y} \right]$$

$$\frac{\partial H_z^-}{\partial y} = k_y [\beta_1 \cosh(\gamma_x x) + \beta_2 \sinh(\gamma_x x)] e^{-\gamma_z z} \sin(k_y y) = 0 \text{ for } n = 0$$

So,

$$H_y = H_y^+ + H_y^- = 0 \quad (6.75)$$

with the boundary condition in (6.64),  $\frac{E_y}{H_z}\Big|_{x=0} = -Z_{t1}$ , we got:

$$E_y\Big|_{x=0} + Z_{t1} H_z\Big|_{x=0} = 0$$

$$E_y\Big|_{x=0} = \frac{\sinh(\gamma_z z)}{k_c^2} [-j\omega\mu_0\gamma_x B_2]$$

$$H_z\Big|_{x=0} = [-B_1] \sinh(\gamma_z z)$$

$$\frac{1}{k_c^2} [-j\omega\mu_0\gamma_x B_2] + Z_{t1} [-B_1] = 0$$

$$-k_c^2 Z_{t1} B_1 - j\omega\mu_0\gamma_x B_2 = 0 \quad (6.76)$$

From the boundary condition (6.65),  $\frac{E_y}{H_z}\Big|_{x=a} = Z_{t2}$ , we got:

$$E_y\Big|_{x=a} - Z_{t2} H_z\Big|_{x=a} = 0$$

$$E_y\Big|_{x=a} = \frac{\sinh(\gamma_z z)}{k_c^2} [-j\omega\mu_0\gamma_x \sinh(\gamma_x a) B_1 - j\omega\mu_0\gamma_x \cosh(\gamma_x a) B_2]$$

$$H_z\Big|_{x=a} = [-B_1 \cosh(\gamma_x a) - B_2 \sinh(\gamma_x a)] \sinh(\gamma_z z)$$

$$\frac{\sinh(\gamma_z z)}{k_c^2} [-j\omega\mu_0\gamma_x \sinh(\gamma_x a) B_1 - j\omega\mu_0\gamma_x \cosh(\gamma_x a) B_2]$$

$$- Z_{t2} [-B_1 \cosh(\gamma_x a) - B_2 \sinh(\gamma_x a)] \sinh(\gamma_z z) = 0$$

$$[-j\omega\mu_0\gamma_x \sinh(\gamma_x a) B_1 - j\omega\mu_0\gamma_x \cosh(\gamma_x a) B_2] - Z_{t2} k_c^2 [-B_1 \cosh(\gamma_x a) - B_2 \sinh(\gamma_x a)] = 0$$

$$(-j\omega\mu_0\gamma_x \sinh(\gamma_x a) + Z_{t2} k_c^2 \cosh(\gamma_x a)) B_1 + (-j\omega\mu_0\gamma_x \cosh(\gamma_x a) + Z_{t2} k_c^2 \sinh(\gamma_x a)) B_2 = 0 \quad (6.77)$$

By combining (6.76) and (6.77), we got:

$$\begin{bmatrix} -k_c^2 Z_{t1} & -j\omega\mu_0\gamma_x \\ -j\omega\mu_0\gamma_x \sinh(\gamma_x a) + Z_{t2} k_c^2 \cosh(\gamma_x a) & -j\omega\mu_0\gamma_x \cosh(\gamma_x a) + Z_{t2} k_c^2 \sinh(\gamma_x a) \end{bmatrix} \times \begin{bmatrix} B_1 \\ B_2 \end{bmatrix} = \begin{bmatrix} 0 \\ 0 \end{bmatrix}$$

It can be written:

$$[M'] [B_1 \ B_2]^T = \vec{0} \quad (6.78)$$

where:

$$[M'] = \begin{bmatrix} M_{13} & M_{14} \\ M_{23} & M_{24} \end{bmatrix} \quad (6.79)$$

### 6.2.5.2. Case ( $n \neq 0$ & $p = 0$ )

If  $p = 0$ ,

$$\gamma_z = jk_z = j \frac{p\pi}{d} = 0$$

So,  $\sinh(\gamma_z z) = 0$  and  $\cosh(\gamma_z z) = 1$ , we got:

$$H_z = [-B_1 \cosh(\gamma_x x) - B_2 \sinh(\gamma_x x)] \cos(k_y y) \sinh(\gamma_z z) = 0$$

So, there are only TM modes in this case.

By doing the same procedure as in the previous section, the formula become

$$[M''] [A_1 \ A_2]^T = \vec{0} \quad (6.80)$$

where:

$$[M''] = \begin{bmatrix} M_{31} & M_{32} \\ M_{41} & M_{42} \end{bmatrix} \quad (6.81)$$



## **6.3. The Z-fold stirrer design**

### **6.3.1. The condition to select the dimension of the mechanical stirrer**

According to [78], the four design rules of the reverberation chamber's mechanical stirrer indicate that:

Criteria 1: "The stirrer has one dimension that is at least one-quarter wavelength at the LUF"

Criteria 2: "The stirrer should have one dimension at least three-quarters of the smallest chamber dimension"

Criteria 3: "Stirrer volume should represent approximately 8% of the whole volume of RC"

Criteria 4: "The stirrer should be shaped asymmetrically to avoid the repetitive field pattern in the RC"

### **6.3.2. Selection of stirrer structure and appropriate dimension**

The Z-fold stirrer is selected as the stirrer structure in this design because of its simple form and as it is generally used in several conventional chamber. Let us remember that the chamber size is (30 cm × 40 cm × 50 cm).

In case that LUF=325.1MHz (the case while the MTMs walls are installed in the chamber in which the wavelength is the biggest) as presented in section 3.2.2.4. These criteria will also be validated for the PEC RC since its LUF ( $f_{LUF,PEC} = 1.533 \text{ GHz}$ ) is higher so its dimension is smaller.

$$\lambda_{LUF} = \frac{C}{f_{LUF}} = \frac{3 \times 10^8 \text{ m/s}}{325.1 \times 10^6 \text{ Hz}} = 0.922 \text{ m}$$

$$\frac{\lambda_{LUF}}{4} = 0.2305 \text{ m} = 23.05 \text{ cm}$$

**So, one-quarter wavelength at the LUF is 23.05 cm.**

The dimension of stirrer along the vertical axis (height of stirrer) is chosen as:

$$L_{stir,z} = 30 \text{ cm}$$

The height of the stirrer is 30 cm. So, it is larger than one-quarter wavelength at the LUF. Hence, the criteria 1 is met.

And with:

$$\frac{3}{4} \min(a, b, d) = \frac{3}{4} \min(30 \text{ cm}, 40 \text{ cm}, 50 \text{ cm}) = \frac{3}{4} (30 \text{ cm}) = 22.5 \text{ cm}$$

**So, three-quarters of the smallest chamber dimension is 22.5 cm.**

The height of the stirrer is 30 cm. So, it is higher than three-quarter of the smallest chamber dimension. Hence, the criteria 2 is met.

The RC total volume

$$V_{RC} = a \times b \times d = 30 \text{ cm} \times 40 \text{ cm} \times 50 \text{ cm} = 60000 \text{ cm}^3 = 0.06 \text{ m}^3$$

$$8\% V_{RC} = 0.08 \times 60000 \text{ cm}^3 = 4800 \text{ cm}^3$$

**So, the 8% of the total internal volume of the reverberation chamber is 4800 cm<sup>3</sup>.**

The two other dimensions of the stirrer are chosen equal to:

$$L_{stir,x} = L_{stir,y} = 12.7 \text{ cm}$$

The volume of stirrer is calculated as:

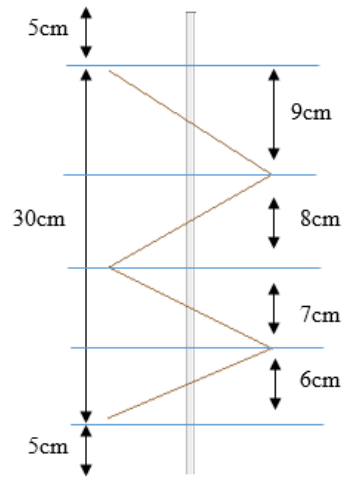
$$V_{stir} = L_{stir,x} \times L_{stir,y} \times L_{stir,z}$$

Then,

$$V_{stir} = L_{stir,x}^2 \times L_{stir,z} = 4838.7 \text{ cm}^3$$

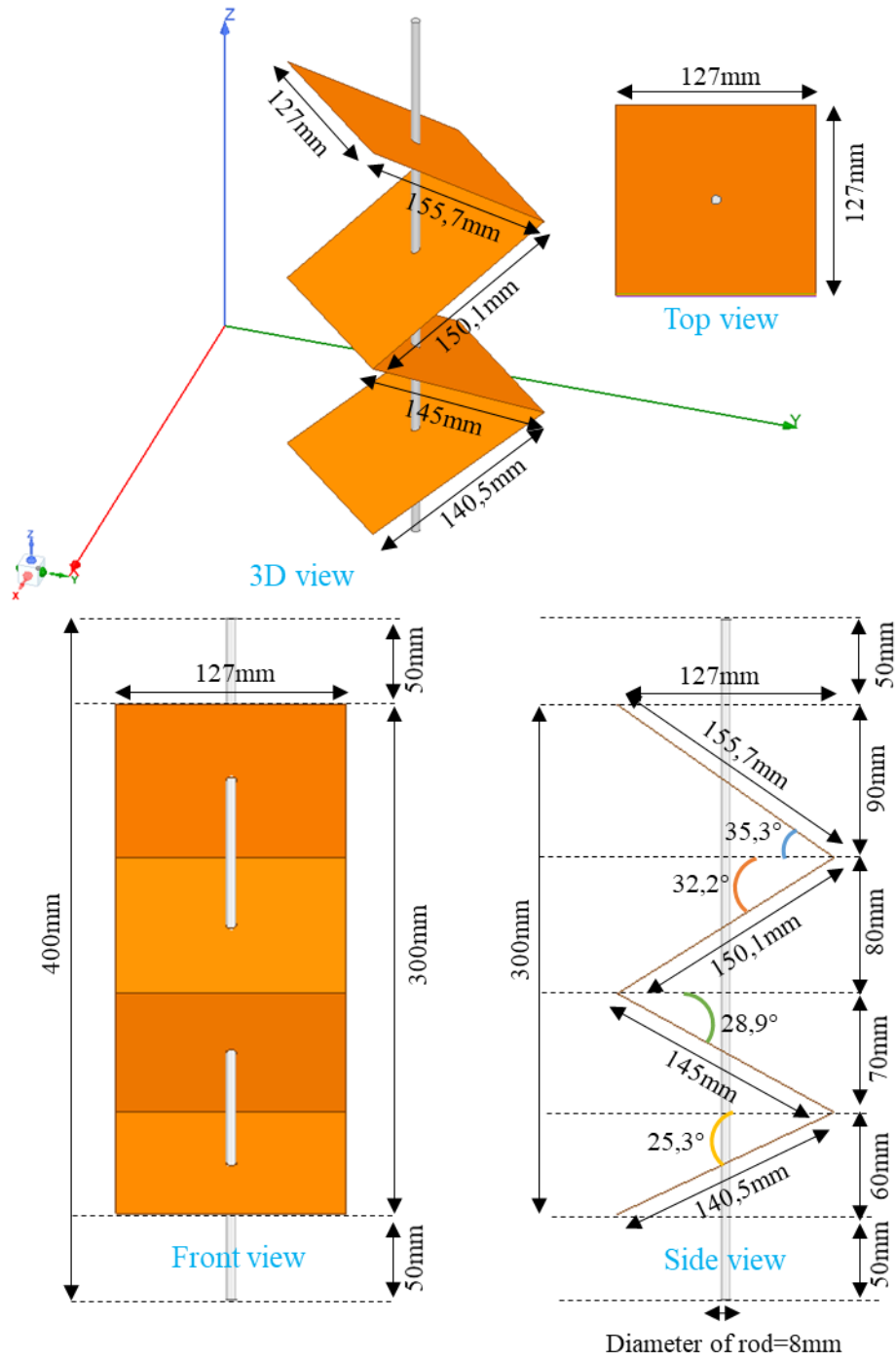
So, the criteria 3 is met due to  $V_{stir} > 4800 \text{ cm}^3$  which is the 8% of the total volume of the reverberation chamber.

To meet the criteria 4: the height of each stirrer wings are set as in Figure 6.2. They are asymmetrical. According to this figure, the height of each wing is set as 6 cm, 7 cm, 8 cm and 9 cm. So, the total height is 30 cm which is equal to  $L_{stir,z}$ .



**Figure 6.2 : Dimension of the 1<sup>st</sup> stirrer (side view)**

Hence, the structure of the stirrer is shown as in Figure 6.3 below.



**Figure 6.3 : The structure of the stirrer for the 1<sup>st</sup> design consideration.**

However, due to the prototype constraint with the length resolution as 1 mm and the angle resolution as 1 degree, the stirrer dimension is modified and presented as in Figure 6.4. In this

modification, the vertical length  $L_{stir,z}$  is reduced from 30 cm to 29 cm. This reduction does not affect the design since all the criteria are still validated.

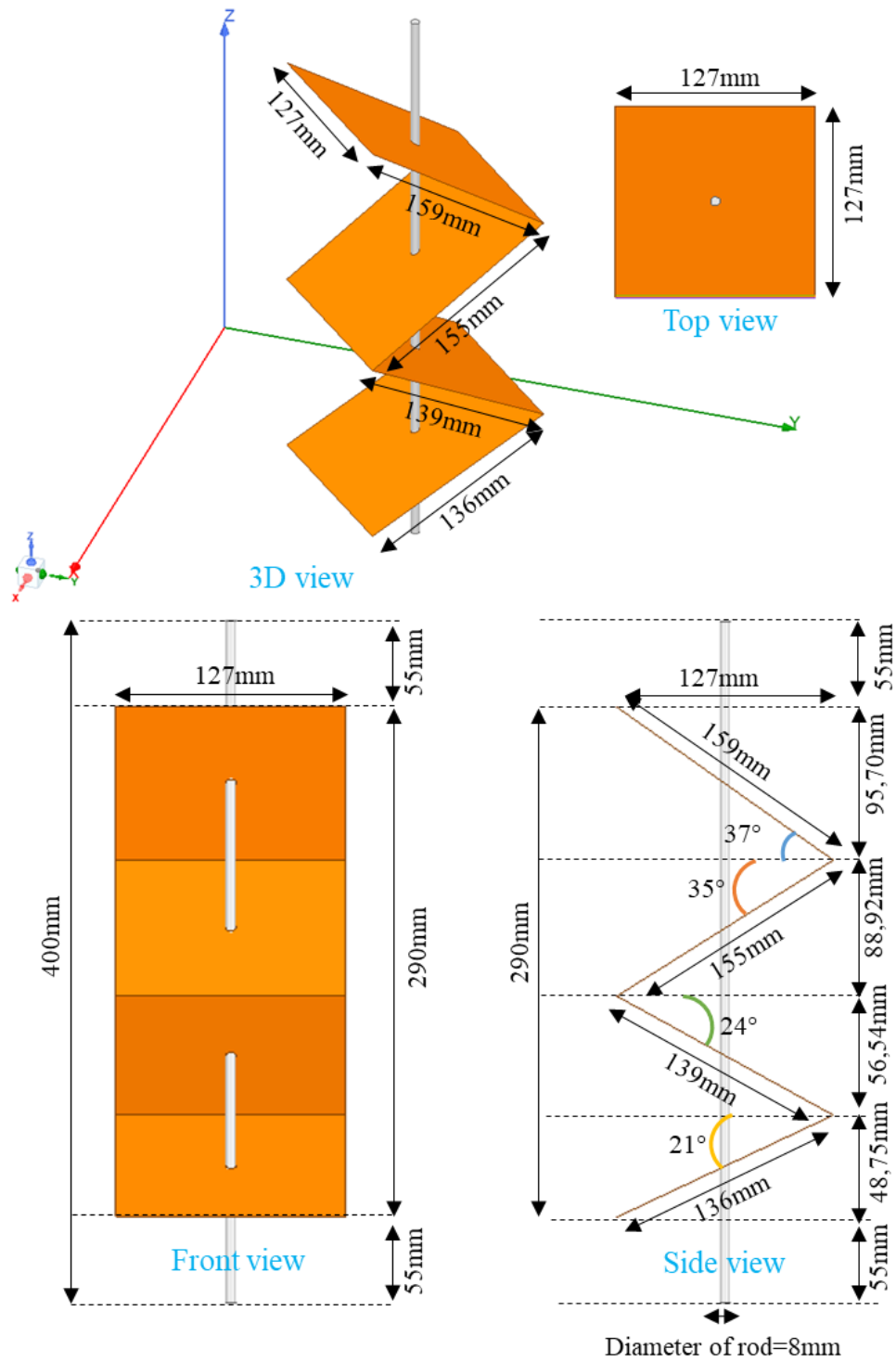
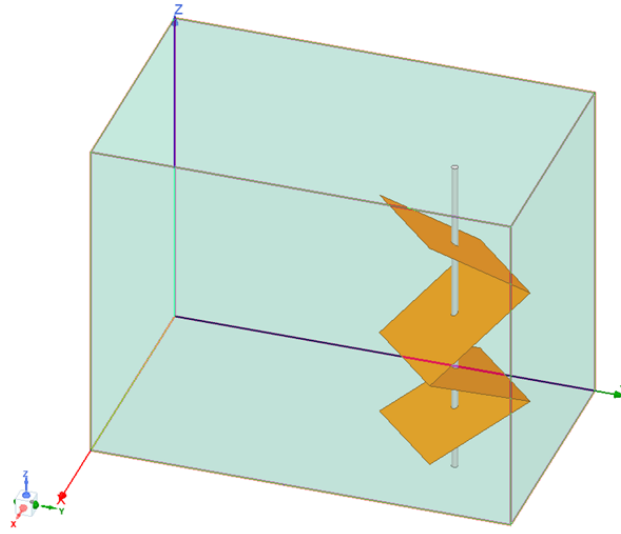


Figure 6.4 : The modified structure of stirrer to ease the prototype fabrication

### 6.3.3. The position of stirrer in the chamber



**Figure 6.5 : RC box which contain one stirrer**

To locate the stirrer in the reverberation for maximizing the chamber's working volume, some parameters are considered. Figure 6.5 shows the defined location of the stirrer in the chamber. Both closest walls to this stirrer are the wall at  $\{x = 30\text{ cm}\}$  and wall at  $\{y = 50\text{ cm}\}$ . The stirrer rod is in contact with the walls at  $\{z = 0\}$  and  $\{z = 40\text{ cm}\}$ . So, the location of the stirrer here depends on the coordinate of the stirrer's rotational axis  $(rod_{center,x}, rod_{center,y})$ .

The radius of the stirrer rotational volume is calculated as:

$$r_{stir} = \frac{L_{stir,x}}{\sqrt{2}} = 8.98\text{cm}$$

By considering that the stirrer rotational volume is located at least 1 cm from all the nearest walls, the  $offset = 1\text{ cm}$ .

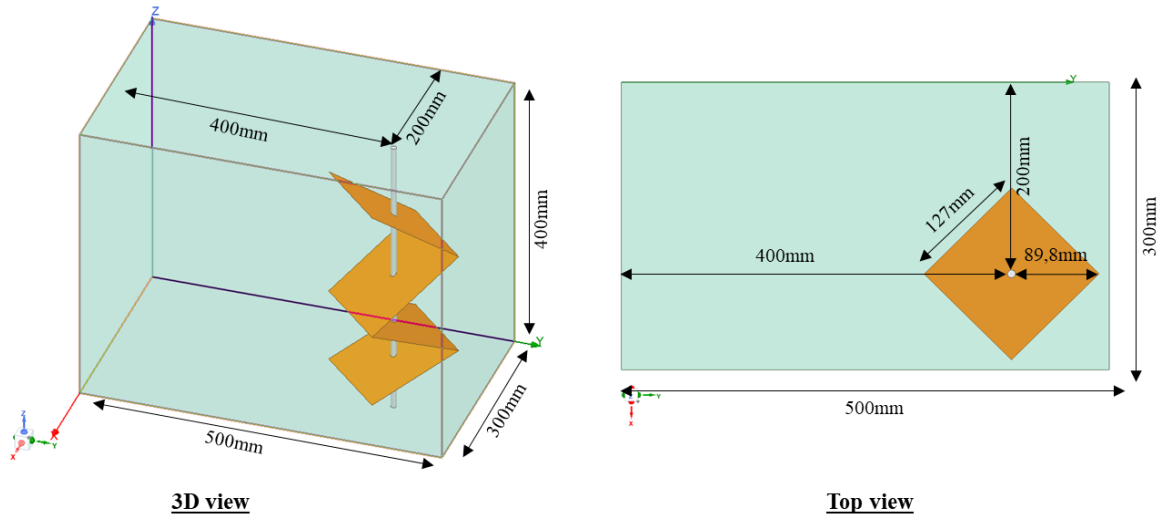
The center of rotational axis of stirrer is located as:

$$rod_{center,x} = 30\text{cm} - r_{stir} - offset = 30\text{cm} - 8.98\text{cm} - 1\text{cm} = 20.02\text{cm}$$

$$rod_{center,y} = 50\text{cm} - r_{stir} - offset = 50\text{cm} - 8.98\text{cm} - 1\text{cm} = 40.02\text{cm}$$

However, to ease the prototype fabrication the center of the stirrer rotational axis is shifted to  $(rod_{center,x}, rod_{center,y}) = (20\text{ cm}, 40\text{ cm})$ . So, the rotational volume of the stirrer is located at least 1.02 cm from the nearest walls. So, the offset become  $offset = 1.02\text{cm} = 10.2\text{ mm}$ .

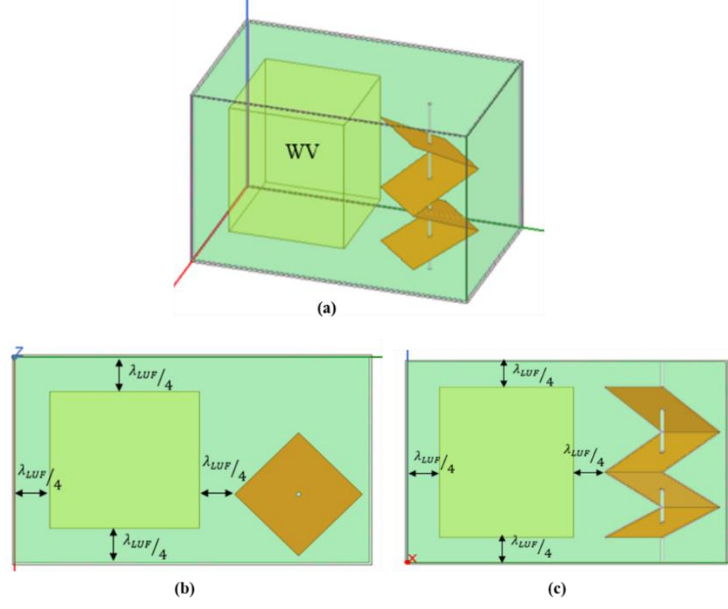
Hence, the location of the stirrer is set as in Figure 6.6.



*Figure 6.6 : Location of stirrer in the RC*

## 6.4. The working volume and location of field probe

For the case of metallic RC box, the working volume is located at  $\frac{\lambda}{4}$  from each metallic walls as well as the stirrer. Figure 6.7 show the location of this working volume inside the reverberation chamber.



**Figure 6.7 : The location of WV in RC: (a) 3D view (b) Top view (c) Side view**

The estimated LUF of metallic wall reverberation chamber according to the rule of 60 resonant modes is at 1.533 GHz when the metallic cavity is empty. According to Figure 6.7, the 3 dimensions of the working volume along the x, y and z axis are:

$$L_{WV,x} = a - \frac{\lambda_{LUF,metal}}{4} - \frac{\lambda_{LUF,metal}}{4} = a - \frac{\lambda_{LUF,metal}}{2}$$

$$L_{WV,y} = d - \frac{\lambda_{LUF,metal}}{4} - \frac{\lambda_{LUF,metal}}{4} - 2r_{stir,y} - offset$$

$$L_{WV,z} = b - \frac{\lambda_{LUF,metal}}{4} - \frac{\lambda_{LUF,metal}}{4} = b - \frac{\lambda_{LUF,metal}}{2}$$

where  $a$ ,  $b$  and  $d$  are the three dimensions of the chamber.

$$\lambda_{LUF,metal} = \frac{3 \times 10^8}{1.533 \times 10^9} = 0.1956m = 19.56cm$$

$$\frac{\lambda_{LUF,metal}}{4} = 0.0489m = 4.89cm$$

So, the WV is located at 4.89 cm from each wall and metallic stirrer of the chamber. However, to ease the field probe insertion and positioning in the WV, the distance of the WV from the walls and stirrer is round 5 cm instead.

Hence, the 3 dimension of the WV are:

$$L_{WV,x} = a - 2 \times 5 \text{ cm} = 30\text{cm} - 10\text{cm} = 20\text{cm}$$

$$L_{WV,y} = d - 2 \times 5 \text{ cm} - 2r_{stir,y} - offset = 50\text{cm} - 10\text{cm} - 2 \times 8.98\text{cm} - 1.02\text{cm} = 21.02\text{cm}$$

$$L_{WV,z} = b - 2 \times 5 \text{ cm} = 40\text{cm} - 10\text{cm} = 30\text{cm}$$

To ease the location of the field probe in the chamber qualification, the dimension of the WV is changed to:

$$L_{WV,x} = 20\text{cm}$$

$$L_{WV,y} = 21\text{cm}$$

$$L_{WV,z} = 30\text{cm}$$

The WV location and the 9 field probe locations for measurement are shown in Figure 6.8.

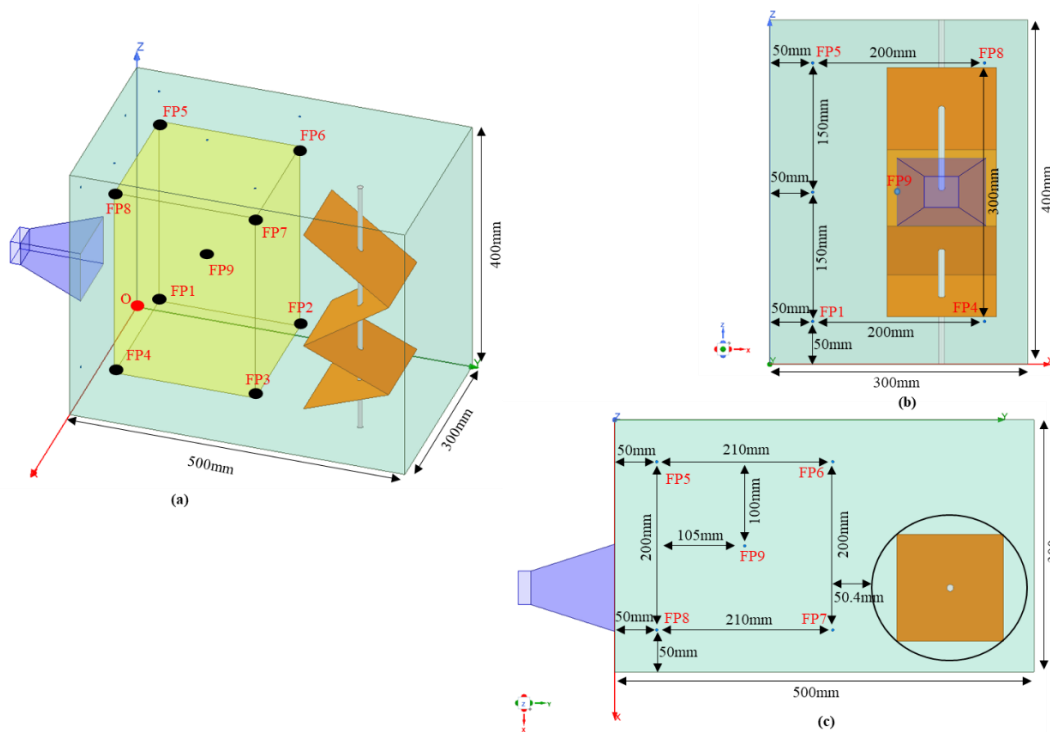


Figure 6.8 : WV and the 9 locations of field probe for chamber validation (a) 3D view (b) Side view (c) Top view



## 6.5. Changing distance to anisotropic surface impedance walls

The effect of the distance between parallel Anisotropic Impedance Surface planes on the resonant frequency of the rectangular cavity with metamaterial walls is analyzed here. The size of the cavity is  $W \times H \times L = 1.90m \times 2.58m \times 2.91m$ .

First, the distance between surface impedance walls is  $W = 1.90m$  with  $Z_t = Z_z = -j188.5 \Omega$ . After that, this distance is changed for  $H = 2.58m$  and then  $L = 2.91m$ , respectively. While 2 parallel walls are isotropic, the others are left PEC. The first 20 resonant modes resulting from calculation by MET and simulated with Eigen mode solver of Ansys-HFSS are shown in **Table 6.1, 6.2 and 6.3**.

*Table 6.1 : The first 20 resonant frequencies for isotropic walls distant from 1.90m*

mode	$f_r$ (MHz) by MET	$f_r$ (MHz) by HFSS
1	17.98669693	17.98721756
2	21.39397372	21.3944021
3	30.59053635	30.59166655
4	31.52929244	31.53072569
5	32.41402907	32.41472143
6	38.64782405	38.64884376
7	44.30028032	44.30471699
8	48.07852467	48.08217148
9	50.70878592	50.71594846
10	51.7074302	51.71629072
11	53.3694291	53.37826
12	54.21999039	54.22976216
13	55.91385774	55.91585126
14	57.88400583	57.88653881
15	68.70353976	68.70706878
16	69.05063799	69.07454492
17	69.60526842	69.62664735
18	69.93509965	69.9567678
19	73.54498708	73.58603839
20	74.20816387	74.21089226

**Table 6.2 : The first 20 resonant frequencies for isotropic walls distant from 2.58m**

mode	$f_r$ (MHz) by MET	$f_r$ (MHz) by HFSS
1	20.28997019	20.29095777
2	26.55686528	26.55711795
3	34.10629552	34.10967545
4	36.6034265	36.60674365
5	41.46909624	41.47343754
6	42.88626979	42.89165428
7	45.60046932	45.60857954
8	46.61324983	46.62118116
9	57.89063595	57.89755912
10	58.23813762	58.24744695
11	69.08517152	69.10044535
12	69.21179849	69.22622254
13	70.54906668	70.56173044
14	70.65943856	70.67157841
15	74.23326076	74.24659228
16	74.30955801	74.32431951
17	77.60916198	77.62637897
18	77.66811229	77.68280701
19	84.30812769	84.32643215
20	84.33449068	84.35626445

**Table 6.3 : The first 20 resonant frequencies for isotropic walls distant from 2.91m**

mode	$f_r$ (MHz) by MET	$f_r$ (MHz) by HFSS
1	24.35772811	24.35917365
2	27.88710941	27.88836997
3	34.55842283	34.56447906
4	36.08971219	36.09470306
5	43.51049052	43.52343678
6	44.18205376	44.18535777
7	51.85000001	51.85593805
8	52.142607	52.15034869
9	62.80080018	62.80857639
10	62.8934317	62.9034056
11	70.58377824	70.59548128
12	70.62477349	70.6368884
13	75.22682234	75.23994788
14	75.25034562	75.26525743
15	77.98439018	78.00013399
16	78.00180767	78.01964479
17	85.60480469	85.62328568
18	85.61627586	85.63157196
19	85.75529088	85.75742475
20	87.68205336	87.69883435

Those 3 tables show that MET and HFSS results are always in very good agreement. When the distance between the isotropic walls is the shortest one ( $W = 1.90m$ ), the resonant frequencies are smaller (for  $Z_t = Z_z = -j188.5 \Omega$ ). Under this condition, the metamaterial walls will be fixed on the closest parallel walls to decrease the LUF.

## **Publications**

1. J. Kean, N. Raveu, H. Kaouach, K. Thourn and S. Sreng, "Analysis of Metamaterial Walls Reverberation Chamber by Using Modal Expansion Theory," *2021 Asia-Pacific International Symposium on Electromagnetic Compatibility (APEMC)*, Nusa Dua - Bali, Indonesia, 2021, pp. 1-4, doi: 10.1109/APEMC49932.2021.9596974.

# References

- [1] L. B. Gravelle and P. F. Wilson, "EMI/EMC in printed circuit boards-a literature review," *IEEE Transactions on Electromagnetic Compatibility*, vol. 34, pp. 109-116, 1992.
- [2] B. Archambeault, C. Brench, and S. Connor, "Review of Printed-Circuit-Board Level EMI/EMC Issues and Tools," *IEEE Transactions on Electromagnetic Compatibility*, vol. 52, pp. 455-461, 2010.
- [3] M. T. Ma, M. Kanda, M. L. Crawford, and E. B. Larsen, "A review of electromagnetic compatibility/interference measurement methodologies," *Proceedings of the IEEE*, vol. 73, pp. 388-411, 1985.
- [4] R. Ganesan and K. R. Kini, "Electromagnetic Interference/Compatibility (EMI/EMC) Measurement," *IETE Technical Review*, vol. 20, pp. 415-424, 2003/09/01 2003.
- [5] I. Barbary, L. O. Fichte, M. Stierner, S. Lange, M. Schaarschmidt, R. Pape, *et al.*, "On the quality of a real open area test site," in *2015 IEEE International Symposium on Electromagnetic Compatibility (EMC)*, 2015, pp. 1201-1206.
- [6] S. Battermann and H. Garbe, "Effects of Realistic Groundplanes to NSA-measurements of Open Area Test Sites (OATS)," *International Union of Radio Science*, 2002.
- [7] M. Hoijer and M. Backstrom, "How we confused the comparison between high level radiated susceptibility measurements in the reverberation chamber and at the open area test site," in *2003 IEEE International Symposium on Electromagnetic Compatibility, 2003. EMC '03.*, 2003, pp. 1043-1046 Vol.2.
- [8] P. Wilson, "On correlating TEM cell and OATS emission measurements," *IEEE Transactions on Electromagnetic Compatibility*, vol. 37, pp. 1-16, 1995.
- [9] M. Donglin, L. Xiao, and L. Dabo, "Research on unwanted reflections in an OATS for precise omni antenna measurement," in *2015 IEEE 6th International Symposium on Microwave, Antenna, Propagation, and EMC Technologies (MAPE)*, 2015, pp. 245-249.
- [10] S. Eser and L. Sevgi, "Open-Area Test Site (OATS) Calibration," *IEEE Antennas and Propagation Magazine*, vol. 52, pp. 204-212, 2010.
- [11] Q. Xu and Y. Huang, *Anechoic and Reverberation Chambers: Theory, Design, and Measurements*: Wiley, 2019.
- [12] E. F. d. Silva, J. S. Rocha, P. R. Lins, S. D. d. Nobrega, and M. S. d. Alencar, "Characterization of electromagnetic radiation absorber materials," in *SBMO/IEEE MTT-S International Conference on Microwave and Optoelectronics, 2005.*, 2005, pp. 326-329.
- [13] C. Junqueira, M. Perotoni, and D. R. Lima, "Microwave absorber materials characterization: bulk absorbing and electrical/magnetic parameters," in *2014 International Telecommunications Symposium (ITS)*, 2014, pp. 1-5.

- [14] D. Mandaris, N. Moonen, S. V. d. Beek, F. Buesink, and F. Leferink, "Validation of a Fully Anechoic Chamber," in *2016 Asia-Pacific International Symposium on Electromagnetic Compatibility (APEMC)*, 2016, pp. 865-868.
- [15] V. S. Reddy and P. Kralicek, "Modeling of semi-anechoic chamber for use in automotive EMC simulations," in *2015 IEEE MTT-S International Microwave and RF Conference (IMaRC)*, 2015, pp. 93-95.
- [16] C. L. Holloway, P. M. McKenna, R. A. Dalke, R. A. Perala, and C. L. Devor, "Time-domain modeling, characterization, and measurements of anechoic and semi-anechoic electromagnetic test chambers," *IEEE Transactions on Electromagnetic Compatibility*, vol. 44, pp. 102-118, 2002.
- [17] Manisha and N. Sood, "Validation of Anechoic Chamber for Radiated Emission Test," in *2018 15th International Conference on ElectroMagnetic Interference & Compatibility (INCEMIC)*, 2018, pp. 1-4.
- [18] R. D. Leo and V. M. Primiani, "Radiated immunity tests: reverberation chamber versus anechoic chamber results," *IEEE Transactions on Instrumentation and Measurement*, vol. 55, pp. 1169-1174, 2006.
- [19] A. C. F. Reniers, A. Hubrechtsen, G. Federico, L. A. Bronckers, and A. B. Smolders, "Spherical mm-Wave Anechoic Chamber for Accurate Far-Field Radiation Pattern Measurements," in *2022 52nd European Microwave Conference (EuMC)*, 2022, pp. 318-321.
- [20] F. Comblet, "Radar cross section measurements in an anechoic chamber: Description of an experimental system and post processing," in *2014 IEEE Conference on Antenna Measurements & Applications (CAMA)*, 2014, pp. 1-4.
- [21] B. K. Chung, H. T. Chuah, and J. W. Bredow, "A microwave anechoic chamber for radar-cross section measurement," *IEEE Antennas and Propagation Magazine*, vol. 39, pp. 21-26, 1997.
- [22] A. Kundu, B. Gupta, K. Patra, and A. I. Mallick, "Role of Reverberation Chamber in Wireless Testing and Measurement with Emphasis on Investigating Biological Effects," in *2020 IEEE Calcutta Conference (CALCON)*, 2020, pp. 132-136.
- [23] E. J. Borgstrom, "A comparison of methods and results using the semi-anechoic and reverberation chamber radiated RF susceptibility test procedures in RTCA/DO-160D, Change One," in *2002 IEEE International Symposium on Electromagnetic Compatibility*, 2002, pp. 184-188 vol.1.
- [24] A. D. Leo, G. Cerri, P. Russo, and V. M. Primiani, "Experimental Validation of an Emission Test Method for Source Stirred Reverberation Chamber," *IEEE Transactions on Electromagnetic Compatibility*, vol. 64, pp. 11-18, 2022.
- [25] C. L. Holloway, D. A. Hill, J. Ladbury, G. Koepke, and R. Garzia, "Shielding effectiveness measurements of materials using nested reverberation chambers," *IEEE Transactions on Electromagnetic Compatibility*, vol. 45, pp. 350-356, 2003.
- [26] M. Á. García-Fernández, D. Carsenat, and C. Decroze, "Antenna Radiation Pattern Measurements in Reverberation Chamber Using Plane Wave Decomposition," *IEEE Transactions on Antennas and Propagation*, vol. 61, pp. 5000-5007, 2013.

- [27] A. Sorrentino, G. Ferrara, and M. Migliaccio, "The Reverberating Chamber as a Line-of-Sight Wireless Channel Emulator," *IEEE Transactions on Antennas and Propagation*, vol. 56, pp. 1825-1830, 2008.
- [28] A. K. Puls, J. M. Ladbury, and W. F. Young, "Antenna Radiation Pattern Measurements Using a Reverberation Chamber," in *2018 AMTA Proceedings*, 2018, pp. 1-6.
- [29] C. Groh, J. P. Karst, M. Koch, and H. Garbe, "TEM waveguides for EMC measurements," *IEEE Transactions on Electromagnetic Compatibility*, vol. 41, pp. 440-445, 1999.
- [30] J. P. Muccioli, T. M. North, and K. P. Slattery, "Predicting module level RF emissions from IC emissions measurements using a 1 GHz TEM or GTEM Cell - a review of related published technical papers," in *2008 IEEE International Symposium on Electromagnetic Compatibility*, 2008, pp. 1-7.
- [31] H. Garbe and D. Hansen, "The GTEM cell concept; applications of this new EMC test environment to radiated emission and susceptibility measurements," in *Seventh International Conference on Electromagnetic Compatibility, 1990*, 1990, pp. 152-156.
- [32] P. Kotwal, G. Verma, and P. K. Katti, "Modelling and Analysis of Gigahertz Transverse Electromagnetic Mode (GTEM) Cell," in *2019 International Conference on Communication and Electronics Systems (ICCES)*, 2019, pp. 1708-1712.
- [33] P. Corona, J. Ladbury, and G. Latmiral, "Reverberation-chamber research-then and now: a review of early work and comparison with current understanding," *IEEE Transactions on Electromagnetic Compatibility*, vol. 44, pp. 87-94, 2002.
- [34] I. A. Buriak and V. O. Zhurba, "A review of microwave metamaterial structures classifications and applications," in *2016 9th International Kharkiv Symposium on Physics and Engineering of Microwaves, Millimeter and Submillimeter Waves (MSMW)*, 2016, pp. 1-3.
- [35] M. Asif, D. A. Sehrai, S. H. Kiani, J. Khan, M. Abdullah, M. Ibrar, *et al.*, "Design of a Dual Band SNG Metamaterial Based Antenna for LTE 4G/WLAN and Ka-Band Applications," *IEEE Access*, vol. 9, pp. 71553-71562, 2021.
- [36] M. M. B. Suwailam, M. S. Boybay, and O. M. Ramahi, "Single-negative (SNG) metamaterials for mutual coupling reduction in high-profile antennas," in *2009 IEEE Antennas and Propagation Society International Symposium*, 2009, pp. 1-4.
- [37] R. W. Ziolkowski, "Design, fabrication, and testing of double negative metamaterials," *IEEE Transactions on Antennas and Propagation*, vol. 51, pp. 1516-1529, 2003.
- [38] M. D. Gregory, J. A. Bossard, Z. C. P. O. Morgan, C. S. Cicero, J. A. Easum, J. D. Binion, *et al.*, "A Low Cost and Highly Efficient Metamaterial Reflector Antenna," *IEEE Transactions on Antennas and Propagation*, vol. 66, pp. 1545-1548, 2018.
- [39] P. Alitalo and S. Tretyakov, "Electromagnetic cloaking with metamaterials," *Materials Today*, vol. 12, pp. 22-29, 2009/03/01/ 2009.

- [40] A. K. Iyer and G. V. Eleftheriades, "Free-Space Imaging Beyond the Diffraction Limit Using a Veselago-Pendry Transmission-Line Metamaterial Superlens," *IEEE Transactions on Antennas and Propagation*, vol. 57, pp. 1720-1727, 2009.
- [41] N. Capet, B. Byrne, L. Claudepierre, and N. Raveu, "Metamaterial waveguide with reduced cross section," in *2013 7th European Conference on Antennas and Propagation (EuCAP)*, 2013, pp. 2155-2157.
- [42] L. Kuhler, G. L. Fur, L. Duchesne, and N. Raveu, "The Propagation Characteristics of 2-D Metamaterial Waveguides Using the Modal Expansion Theory," *IEEE Transactions on Microwave Theory and Techniques*, vol. 66, pp. 4319-4326, 2018.
- [43] D. Seetharamdoo and I. M. Coccato, "Investigation on the use of metamaterials to lower the operating frequency of reverberation chamber," in *10th International Symposium on Electromagnetic Compatibility*, 2011, pp. 680-685.
- [44] L. F. Wanderlinder, D. Lemaire, and D. Seetharamdoo, "Experimental analysis for metamaterials used to lower the LUF of a reverberation chamber," in *2016 International Symposium on Electromagnetic Compatibility - EMC EUROPE*, 2016, pp. 240-244.
- [45] L. F. Wanderlinder, D. Lemaire, I. Coccato, and D. Seetharamdoo, "Practical implementation of metamaterials in a reverberation chamber to reduce the LUF," in *2017 IEEE 5th International Symposium on Electromagnetic Compatibility (EMC-Beijing)*, 2017, pp. 1-3.
- [46] M. I. Andries, D. Seetharamdoo, and P. Besnier, "Analytical modal analysis to evaluate the contribution of metamaterials to the improvement of reverberation chambers," in *2014 International Symposium on Electromagnetic Compatibility*, 2014, pp. 883-888.
- [47] N. Raveu, B. Byrne, L. Claudepierre, and N. Capet, "Modal Theory for Waveguides With Anisotropic Surface Impedance Boundaries," *IEEE Transactions on Microwave Theory and Techniques*, vol. 64, pp. 1153-1162, 2016.
- [48] G. Andrieu, F. Tristant, and A. Reineix, "Investigations about the Use of Aeronautical Metallic Halls Containing Apertures as Mode-Stirred Reverberation Chambers," *IEEE Transactions on Electromagnetic Compatibility*, vol. 55, pp. 13-20, 2013.
- [49] G. Andrieu, N. Ticaud, F. Lescoat, and L. Trougnou, "Radiated Susceptibility Tests in Thermal Vacuum Chambers Working as Reverberation Chambers," in *2018 International Symposium on Electromagnetic Compatibility (EMC EUROPE)*, 2018, pp. 1-9.
- [50] A. K. Fall, P. Besnier, C. Lemoine, M. Zhadobov, and R. Sauleau, "Design and Experimental Validation of a Mode-Stirred Reverberation Chamber at Millimeter Waves," *IEEE Transactions on Electromagnetic Compatibility*, vol. 57, pp. 12-21, 2015.
- [51] J. A. Andriambelason, P. G. Wiid, and H. C. Reader, "Reverberation chamber: Calibration, evaluation and application in transfer impedance measurement," in *IEEE Africon '11*, 2011, pp. 1-4.



- [52] J. Yousaf, H. Lee, M. Faisal, J. Han, W. Nah, H. Shahwani, *et al.*, "Design, analysis, and validation of Radio Research Agency reverberation chamber," *International Journal of Communication Systems*, vol. 34, 11/24 2020.
- [53] M. Poci, I. Dotto, D. Festa, and G. D. Abreu, "Improving the Performances of a Reverberation Chamber: a Real Case," in *2009 20th International Zurich Symposium on Electromagnetic Compatibility*, 2009, pp. 53-56.
- [54] D. A. Hill, "Electromagnetic fields in cavities: Deterministic and statistical theories " *IEEE Antennas and Propagation Magazine*, vol. 56, pp. 306-306, 2009.
- [55] I. E. C. Std, "Electromagnetic compatibility (EMC) - 61000-4-21: Testing and Measurement techniques - Reverberation chamber test methods ", ed.
- [56] L. Bastianelli, F. Moglie, and V. M. Primiani, "Evaluation of stirrer efficiency varying the volume of the reverberation chamber," in *2016 IEEE International Symposium on Electromagnetic Compatibility (EMC)*, 2016, pp. 19-24.
- [57] G. Andrieu, "Calibration of reverberation chambers from S11 measurements," in *2017 International Symposium on Electromagnetic Compatibility - EMC EUROPE*, 2017, pp. 1-6.
- [58] G. Andrieu, N. Ticaud, F. Lescoat, and L. Trougnou, "Fast and Accurate Assessment of the “Well Stirred Condition” of a Reverberation Chamber From S11 Measurements," *IEEE Transactions on Electromagnetic Compatibility*, vol. 61, pp. 974-982, 2019.
- [59] X. Guo, Z. He, Y. Zhang, X. Zhou, and M. Nie, "Investigation of field uniformity validation in reverberation chamber using VNA," in *2015 7th Asia-Pacific Conference on Environmental Electromagnetics (CEEM)*, 2015, pp. 270-273.
- [60] J. Yousaf, M. Ghazal, M. N. Hasan, H. Lee, W. Nah, and J. G. Yang, "Rapid Alternative Calibration Procedure of Reverberation Chamber Using Coupling Transfer Gain Function," in *2020 IEEE International Symposium on Antennas and Propagation and North American Radio Science Meeting*, 2020, pp. 1273-1274.
- [61] G. Andrieu, "Calibration of reverberation chambers from S21 measurements," in *2017 IEEE International Symposium on Electromagnetic Compatibility & Signal/Power Integrity (EMCSI)*, 2017, pp. 675-680.
- [62] "Siepel Commercial Products," ed.
- [63] M. Poci, I. Dotto, G. D. Abreu, and D. Festa, "Experimental definition of the lowest usable frequency (LUF) of an aluminum made reverberation chamber with reference to the IEC 61000-4-21 standard," in *2006 IEEE International Symposium on Electromagnetic Compatibility, 2006. EMC 2006.*, 2006, pp. 849-852.
- [64] R. Serra, A. C. Marvin, F. Moglie, V. M. Primiani, A. Cozza, L. R. Arnaut, *et al.*, "Reverberation chambers a la carte: An overview of the different mode-stirring techniques," *IEEE Electromagnetic Compatibility Magazine*, vol. 6, pp. 63-78, 2017.

- [65] J. Ji, X. Zhou, and P. Hu, "Frequency-dependent oscillating wall stirrer for measurement of quality factor in a reverberation chamber," in *2019 IEEE International Conference on Computation, Communication and Engineering (ICCCE)*, 2019, pp. 142-145.
- [66] Z. Zhou, P. Hu, X. Zhou, J. Ji, M. Sheng, P. Li, *et al.*, "Performance Evaluation of Oscillating Wall Stirrer in Reverberation Chamber Using Correlation Matrix Method and Modes Within  $Q$ -Bandwidth," *IEEE Transactions on Electromagnetic Compatibility*, vol. 62, pp. 2669-2678, 2020.
- [67] Z. Yang, X. Zhou, Z. Zhou, and H. Li, "Design and Simulation of z-folded Stirrer in Reverberation Chambers," in *2021 IEEE 5th Information Technology, Networking, Electronic and Automation Control Conference (ITNEC)*, 2021, pp. 641-645.
- [68] L. R. Arnaut, "Compound exponential distributions for undermoded reverberation chambers," *IEEE Transactions on Electromagnetic Compatibility*, vol. 44, pp. 442-457, 2002.
- [69] D. Fedeli, M. Iualè, V. M. Primiani, and F. Moglie, "Experimental and numerical analysis of a carousel stirrer for reverberation chambers," in *2012 IEEE International Symposium on Electromagnetic Compatibility*, 2012, pp. 228-233.
- [70] F. Moglie and V. M. Primiani, "Numerical Analysis of a New Location for the Working Volume Inside a Reverberation Chamber," *IEEE Transactions on Electromagnetic Compatibility*, vol. 54, pp. 238-245, 2012.
- [71] F. Leferink, J. C. Boudenot, and W. v. Etten, "Experimental results obtained in the vibrating intrinsic reverberation chamber," in *IEEE International Symposium on Electromagnetic Compatibility. Symposium Record (Cat. No.00CH37016)*, 2000, pp. 639-644 vol.2.
- [72] Z. Zhou, P. Hu, X. Zhou, J. Ji, M. Sheng, P. Li, *et al.*, "Performance Evaluation of Oscillating Wall Stirrer in Reverberation Chamber Using Correlation Matrix Method and Modes Within  $Q$ -Bandwidth," *IEEE Transactions on Electromagnetic Compatibility*, vol. 62, pp. 2669-2678, 2020.
- [73] D. Barakos and R. Serra, "Performance characterization of the oscillating wall stirrer," in *2017 International Symposium on Electromagnetic Compatibility - EMC EUROPE*, 2017, pp. 1-4.
- [74] Y. Shih-Pin and C. F. Bunting, "Statistical investigation of frequency-stirred reverberation chambers," in *2003 IEEE Symposium on Electromagnetic Compatibility. Symposium Record (Cat. No.03CH37446)*, 2003, pp. 155-159 vol.1.
- [75] A. Cozza, W. J. Koh, Y. S. Ng, and Y. Y. Tan, "Controlling the state of a reverberation chamber by means of a random multiple-antenna stirring," in *2012 Asia-Pacific Symposium on Electromagnetic Compatibility*, 2012, pp. 765-768.
- [76] E. Voges and T. Eisenburger, "Electrical Mode Stirring in Reverberating Chambers by Reactively Loaded Antennas," *IEEE Transactions on Electromagnetic Compatibility*, vol. 49, pp. 756-761, 2007.
- [77] G. Cerri, V. M. Primiani, S. Pennesi, and P. Russo, "Source stirring mode for reverberation chambers," *IEEE Transactions on Electromagnetic Compatibility*, vol. 47, pp. 815-823, 2005.

- [78] Q. Xu and Y. Huang, *Anechoic and Reverberation Chambers: Theory, Design, and Measurements*: Wiley, 2018.
- [79] B. H. Liu, D. C. Chang, and M. T. Ma, "Eigenmodes and the Composite Quality Factor of a Reverberating Chamber | NIST," 1983.
- [80] C. L. Holloway, D. A. Hill, J. M. Ladbury, and G. Koepke, "Requirements for an effective reverberation chamber: unloaded or loaded," *IEEE Transactions on Electromagnetic Compatibility*, vol. 48, pp. 187-194, 2006.
- [81] S. Qakir, Q. Asian, and F. Leferink, "Comparison of test standards for immunity testing in reverberation chambers," in *2017 Asia-Pacific International Symposium on Electromagnetic Compatibility (APEMC)*, 2017, pp. 44-46.
- [82] R. SC-135, *Environmental conditions and test procedures for airborne equipment*: RTCA, 2010.
- [83] I. 61000-4-21, "Electromagnetic compatibility (EMC)–Part 4–21: Testing and measurement techniques–Reverberation chamber test methods," ed: International Electrotechnical Commission, 2011.
- [84] A. D. Leo, G. Gradoni, G. Cerri, P. Russo, and V. M. Primiani, "Design and Experimental Validation of a Stochastic Diffractor for a Multiple Monopole Source Stirring Reverberation Chamber," in *2020 XXXIIIrd General Assembly and Scientific Symposium of the International Union of Radio Science*, 2020, pp. 1-4.
- [85] D. Yan, Q. Xu, C. Yu, Y. Huang, and T. H. Loh, "A Broadband Reference Antenna for Efficiency Measurements in a Reverberation Chamber," in *2020 IEEE 3rd International Conference on Electronic Information and Communication Technology (ICEICT)*, 2020, pp. 302-305.
- [86] L. Xiaoqiang, W. Guanghui, Z. Yongqiang, and Z. Chenghuai, "Effects of Stirrer on the Field Uniformity at Low Frequency in a Reverberation Chamber and its Simulation," in *2008 International Symposium on Computer Science and Computational Technology*, 2008, pp. 517-519.
- [87] S. Lup, C. Munteanu, S. Baranowski, and L. Kane, "3D numerical simulation of the stirrer effect inside a reverberation chamber," in *2012 International Conference and Exposition on Electrical and Power Engineering*, 2012, pp. 672-675.
- [88] A. Ubin, R. Vogt-Ardatjew, F. Leferink, M. Z. M. Jenu, and S. V. D. Beek, "Statistical analysis of three different stirrer designs in a reverberation chamber," in *2015 Asia-Pacific Symposium on Electromagnetic Compatibility (APEMC)*, 2015, pp. 604-607.
- [89] J. Yousaf, H. Lee, H. Junhee, J. Kim, M. Faisal, J. G. Yang, *et al.*, "Analysis of Effect of Stirrer Type on Field Uniformity in RRA Reverberation Chamber," in *2018 International Symposium on Antennas and Propagation (ISAP)*, 2018, pp. 1-2.
- [90] J. Tang, Z. Zhang, X. Chen, M. Zhao, S. Zhu, and A. Zhang, "Comparison of Three Types of Stirrers in Terms of Field Uniformity in a Reverberation Chamber," in *2018 12th International Symposium on Antennas, Propagation and EM Theory (ISAPE)*, 2018, pp. 1-4.

- [91] A. B. Ubin and M. Z. B. M. Jenu, "Field uniformity evaluation of different stirrer structure in a reverberation chamber," in *2012 IEEE Asia-Pacific Conference on Applied Electromagnetics (APACE)*, 2012, pp. 32-35.
- [92] A. Kadri, D. C. Pande, and A. Mishra, "A Criteria Based Design for the Shape of a Stirrer in a Reverberation Chamber," in *2018 International Conference on Information , Communication, Engineering and Technology (ICICET)*, 2018, pp. 1-4.
- [93] V. M. Primiani and F. Moglie, "Reverberation Chamber Performance Varying the Position of the Stirrer Rotation Axis," *IEEE Transactions on Electromagnetic Compatibility*, vol. 56, pp. 486-489, 2014.
- [94] D. T. Le and Y. Karasawa, "A novel compact ultra-wideband dipole antenna," in *2012 6th European Conference on Antennas and Propagation (EUCAP)*, 2012, pp. 2815-2818.
- [95] U. Schwarz, F. Thiel, F. Seifert, R. Stephan, and M. Hein, "Ultra-wideband antennas for combined magnetic resonance imaging and UWB radar applications," in *2009 IEEE MTT-S International Microwave Symposium Digest*, 2009, pp. 1433-1436.
- [96] B. Wang and Y. Wei, "Design of a Small and Compact Monopole Ultra Wideband Antenna," in *2018 International Conference on Microwave and Millimeter Wave Technology (ICMMT)*, 2018, pp. 1-3.
- [97] B. Byrne, N. Raveu, N. Capet, G. L. Fur, and L. Duchesne, "Field distribution of rectangular waveguides with anisotropic walls by using the modal theory," in *2016 IEEE International Symposium on Antennas and Propagation (APSURSI)*, 2016, pp. 1091-1092.
- [98] S. Boyes and Y. Huang, *Reverberation Chambers: Theory and Applications to EMC and Antenna Measurements*, 2016.
- [99] KEMET. *KEMET Electronics HiQ-CBR (RF & Microwave) Capacitors*. Available: <https://www.mouser.fr/new/kemet-electronics/kemetcbmlccs/>
- [100] M. Y. Koledintseva, A. Koul, S. Hinaga, and J. L. Drewniak, "Differential and extrapolation techniques for extracting dielectric loss of printed circuit board laminates," in *2011 IEEE MTT-S International Microwave Symposium*, 2011, pp. 1-4.
- [101] R. Torres-Torres and V. H. Vega-González, "An approach for quantifying the conductor and dielectric losses in PCB transmission lines," in *2009 IEEE 18th Conference on Electrical Performance of Electronic Packaging and Systems*, 2009, pp. 235-238.
- [102] J. Yousaf, H. Lee, J. Han, W. Nah, H. Shahwani, S. Shah, *et al.*, "Design, analysis, and validation of Radio Research Agency reverberation chamber," *International Journal of Communication Systems*, vol. 34, 02/01 2021.